**Czech Technical University in Prague**

**Faculty of Civil Engineering**

**Department of Mechanics**



# Application of electrochemical impedance spectroscopy for porosity determination of cementitious materials

Bc. Jana Chalupová

Diploma Thesis

Supervisor:  Ing. Jiří Němeček, Ph.D.
Year:  Prague, 2023

ČVUT
ČESKÉ VYSOKÉ
UČENÍ TECHNICKÉ
V PRAZE

# ZADÁNÍ DIPLOMOVÉ PRÁCE

## I. OSOBNÍ A STUDIJNÍ ÚDAJE

Příjmení: Chalupová     Jméno: Jana     Osobní číslo: 477385

Zadávající katedra: 132 - Katedra mechaniky

Studijní program: Stavební inženýrství

Studijní obor/specializace: Konstrukce pozemních staveb

## II. ÚDAJE K DIPLOMOVÉ PRÁCI

Název diplomové práce: Využití elektrochemické impedanční spektroskopie pro stanovení porozity cementových materiálů

Název diplomové práce anglicky: Application of electrochemical impedance spectroscopy for porosity determination of cementitious materials

Pokyny pro vypracování:
Cílem práce je navrhnout a zpracovat několik směsí čisté a nanopřísadami modifikované cementové pasty a stanovit porozitu pomocí nedestruktivní metody elektrochemické impedanční spektroskopie (EIS). V práci bude provedena rešerše o využití EIS pro cementové materiály. Bude provedena série EIS měření v různých časech hydratace za účelem sledování vývoje elektrických parametrů a následného výpočtu porozity. Výpočet porozity z EIS bude proveden pomocí analytických modelů, např. modifikovaný Archieho zákon. Porozita získaná pomocí EIS bude porovnána s porozitou stanovenou jinými metodami: heliová pyknometrie, rtuťová porozimetrie, otevřená porozita a elektronová mikroskopie v kombinaci s obrazovou analýzou.

Seznam doporučené literatury:
Guangling Song (2000) - Equivalent circuit model for AC electrochemical impedance spectroscopy of concrete
Robert Cottis, Stephen Turgoose (1999) - Electrochemical Impedance nad Noise
Yonathan Reches (2018) - Nanoparticles as concrete additives: Review and perspectives
K. B. Sanish, Narayanan Neithalath (2013) - Monitoring the evolution of material structure in cement pastes and concretes using electrical property measurements

Jméno vedoucího diplomové práce: Ing. Jiří Němeček, Ph.D.

Datum zadání diplomové práce: 19.9.2022     Termín odevzdání DP v IS KOS: 9.1.2023
*Údaj uveďte v souladu s datem v časovém plánu příslušného ak. roku*

Podpis vedoucího práce     Podpis vedoucího katedry

## III. PŘEVZETÍ ZADÁNÍ

*Beru na vědomí, že jsem povinen vypracovat diplomovou práci samostatně, bez cizí pomoci, s výjimkou poskytnutých konzultací. Seznam použité literatury, jiných pramenů a jmen konzultantů je nutné uvést v diplomové práci a při citování postupovat v souladu s metodickou příručkou ČVUT „Jak psát vysokoškolské závěrečné práce" a metodickým pokynem ČVUT „O dodržování etických principů při přípravě vysokoškolských závěrečných prací".*

23.9.2022
Datum převzetí zadání     Podpis studenta(ky)

# SPECIFIKACE  ZADÁNÍ

Jméno diplomanta:  Jana Chalupová

Název diplomové práce: Využití elektrochemické impedanční spektroskopie pro stanovení porozity cementových materiálů

Základní část: Využití elektrochemické impedanční spektroskopie pro stanovení porozity cementových materiálů     podíl: 100    %

Formulace úkolů:  Navržení a zpracování několika směsí čisté a nanopřísadami modifikované cementové pasty a stanovení porozity pomocí nedestruktivní metody elektrochemické impedanční spektroskopie (EIS). Provedení rešerše o využití EIS pro cementové materiály. Provedení série EIS měření v různých časech hydratace za účelem sledování vývoje elektrických parametrů a následného výpočtu porozity. Výpočet porozity z EIS pomocí analytických modelů. Porovnání porozity získané pomocí EIS s porozitou stanovenou jinými metodami: heliová pyknometrie, rtuťová porozimetrie, otevřená porozita a elektronová mikroskopie v kombinaci s obrazovou analýzou.

Podpis vedoucího DP:.....................................................      Datum: ......29.9.2022......

Případné další části diplomové práce (části a jejich podíl určí vedoucí DP):

2. Část: ............................................................................ podíl: ............ %

    Konzultant (jméno, katedra): ...........................................

    Formulace úkolů:

Podpis konzultanta:......................................................      Datum: .......................

3. Část: ............................................................................ podíl: ............ %

    Konzultant (jméno, katedra): ...........................................

    Formulace úkolů:

Podpis konzultanta:......................................................      Datum: .......................

4. Část: ............................................................................ podíl: ............ %

    Konzultant (jméno, katedra): ...........................................

    Formulace úkolů:

Podpis konzultanta:......................................................      Datum: .......................

# Declaration

I hereby declare that this diploma thesis has been my own work, written under supervision of Ing. Jiří Němeček, Ph.D.

All sources of information that have been used in the diploma thesis are acknowledged in the text and listed in the Bibliography.

In Prague, January 2023

.........................................

Bc. Jana Chalupová

# Acknowledgements

First, I would like to express my deepest gratitude to my supervisor, Ing. Jiří Němeček, Ph.D., for his guidance, advice, selection of the topic of this thesis and especially for his time and willingness devoted to me in the development of this thesis.

Further, the thank belong to Ing. Pavel Trávníček, Ph.D. for his advice and making the epoxy prints used for the formwork and prof. Ing. Jiří Němeček, Ph.D., DSc. for reading and correcting this thesis. Also, I would like to thank Ing. Vojtěch Pommer for his help in obtaining values from mercury intrusion porosimetry and helium pycnometry.

Also, I want to thank my colleagues from the University of Chemistry and Technology for performing analysis of the chloride penetration test. Further, the thank belongs to Ing. Vojtěch Hybášek for his help in electrochemical impedance spectroscopy.

Most importantly, the thank belong to my family and partner for their support, patience and motivation throughout the whole study.

# Abstract

In this thesis, the porosity and electric properties of pure cement paste, nanoparticles-modified cement pastes, and mortar were observed. Electrochemical impedance spectroscopy (EIS) was the main method used to obtain these material properties. The dimensions of the samples and electrode positions were specially designed for EIS measurement. Different equivalent electric circuit models were used to evaluate the resistance and capacitance of the material. Analytical models such as modified Archie's law and general effective media model were used to evaluate porosity from EIS. Moreover, for comparison with EIS, porosity was obtained by gravimetric method, helium pycnometry, mercury intrusion porosimetry, and image analysis based on scanning electron microscope output. In addition, a chloride penetration test was performed to study the dependence of the electrical resistance on the chloride concentration. During the observation period (1 day - 3 months), the resistances of all mixtures increased with hydration time while the porosity decreased. The differences between the mixtures were observed by all methods used. Analytical models considering multiple material parameters are best suited for the evaluation of porosity from EIS.

**Keywords**

Porosity, electrochemical impedance spectroscopy, equivalent electric circuit model, Archie's law, general effective media model, nanoparticles, cement paste.

# Abstrakt

V této práci byla pozorována porozita a elektrické vlastnosti čisté cementové pasty, nanočásticemi modifikovaných cementových past a malty. Jako hlavní metoda použitá ke zkoumání těchto materiálových vlastností byla elektrochemická impedanční spektroskopie (EIS). Speciálně pro EIS měření byly navrženy rozměry vzorku a poloha elektrod. K vyhodnocení odporů a kapacit měřených materiálů byly použity různé modely ekvivalentního elektrického obvodu. K vyhodnocení porozity z měření EIS byly použity analytické modely jako jsou různé modifikace Archieho zákona a nebo *general effective media* model. Pro porovnání s EIS byla porozita měřena také gravimetrickou metodou, héliovou pyknometrií, rtuťovou porozimetrií a obrazovou analýzou založenou na výstupech ze skenovacího elektronového mikroskopu. Byl proveden také test penetrace chloridů, ve kterém byla sledována závislost koncentrace chloridů v materiálu na jeho elektrickém odporu. V průběhu sledovaného období (1 den až 3 měsíce) vzrostly s hydratačním časem a současným úbytkem porozity odpory všech směsí. Také rozdíly mezi jednotlivými směsmi byly pozorovány ve všech použitých metodách. Analytické modely uvažující vliv vícefázových parametrů v materiálu jsou nejvhodnější pro vyhodnocení porozity z EIS.

**Klíčová slova**

Porozita, elektrochemická impedanční spektroskopie, model ekvivalentního elektrického obvodu, Archieho zákon, *general effective media* model, nanopřísady, cementová pasta.

# List of Figures

# List of Tables

# Abbreviations

| | |
|---|---|
| **AC** | **A**lternating **C**urrent |
| **ACIS** | **A**lternating **C**urrent **I**mpedance **S**pectroscopy |
| **BSE** | **B**ack**S**cattered **E**lectron |
| **C** | pure **C**ement paste |
| **C$_2$S** | di**C**alcium **S**ilicate |
| **C$_3$S** | tri**C**alcium **S**ilicate |
| **C$_3$A** | tri**C**alcium **A**luminate |
| **C$_4$AF** | tetra**C**alcium **A**lumino**F**errit |
| **CA** | **C**ement paste modified by 1.5 % of nano-**A**lumina |
| **C-A-S-H** | **C**alcium-**A**lumina-**S**ilica-**H**ydrate |
| **CBMs** | **C**ement **B**ased **M**aterials |
| **CCP** | **C**ontinuous **C**onductive **P**ath |
| **CH** | crystalline **C**alcium **H**ydroxide (Portlandite) |
| **CNT** | **C**arbon **N**ano-**T**ubes |
| **CPE** | **C**onstant **P**hase **E**lement |
| **CS-I** | **C**ement paste modified by 1.25 % of nano-**S**ilica |
| **CS-II** | **C**ement paste modified by 2.5 % of nano-**S**ilica |
| **C-S-H** | **C**alcium-**S**ilicate-**H**ydrate |
| **DCP** | **D**iscontinuous **C**onductive **P**ath |
| **DoH** | **D**egree **of** **H**ydration |
| **DP** | **D**iscontinuous **P**oint |
| **EC** | **E**quivalent **C**ircuit model |
| **EDS** | **E**nergy **D**ispersive X-ray **S**pectrometry |
| **EIS** | **E**lectrochemical **I**mpedance **S**pectroscopy |
| **FP** | **F**ull **P**late |
| **G** | **G**rid |
| **GEM** | **G**eneral **E**ffective **M**edia model |
| **HD C-S-H** | **H**igh-**D**ensity **C**alcium-**S**ilicate-**H**ydrate |
| **IA** | **I**mage **A**nalysis |
| **ICP** | **I**nsulator **C**onductive **P**ath |
| **IP** | **I**nner **P**roduct |
| **LD C-S-H** | **L**ow-**D**ensity **C**alcium-**S**ilicate-**H**ydrate |
| **LSCM** | **L**aser **S**canning **C**onfocal **M**icroscopy |
| **M** | **M**ortar |
| **MIP** | **M**ercury **I**nstrusion **P**orosimetry |
| **NMR** | proton **N**uclear **M**agnetic **R**esonance |
| **nA** | **n**ano-**A**lumina |
| **NIST** | **N**ational **I**nstitute of **S**tandards and **T**echnology |
| **NPs** | **N**ano-**P**articles |

| | |
|---|---|
| **nS** | **n**ano-**S**ilica |
| **OP** | **O**uter **P**roduct |
| **OPC** | **O**rdinary **P**ortland **C**ement |
| **PP** | **P**erforated **P**late |
| **RH** | **R**elative **H**umidity |
| **RCPT** | **R**apid **C**hloride **P**ermeability **T**est |
| **SCM** | **S**upplementary **C**ementitious **M**aterial |
| **SE** | **S**econdary **E**lectrons |
| **SEC** | **S**implified **E**quivalent **C**ircuit model |
| **SEM** | **S**canning **E**lectron **M**icroscopy |
| $\mu$**CT** | micro **C**omputed **T**omography |

# Contents

# 1    Introduction

Concrete structures are very often reinforced with steel. However, the reinforcement needs to be protected from adverse influences that can cause corrosion of the reinforcement and subsequent degradation of the entire structure. The protection of reinforcement is ensured by a covering layer of concrete. The long-term durability and resistance of the covering layer are closely related to its porosity. High porosity increases diffusion through the material, resulting in easier penetration of ions and gases through the porous system in a cement matrix, as shown in Figure 1.1. The most common processes are carbonation, sulfate attack, chloride penetration, alkali-silica reaction, and corrosion of steel structure [1]. As porosity decreases, the durability of the structure increases because the mass transfer is retarded.
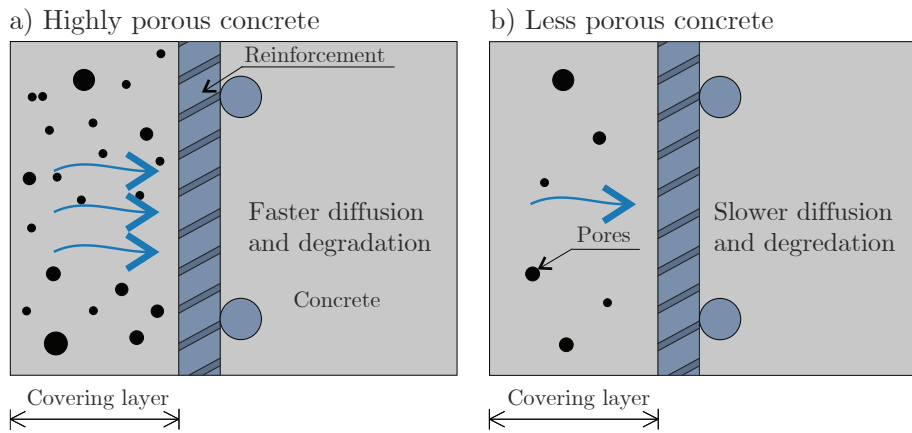


Figure 1.1: Effect of pore volume on concrete diffusity: a) highly porous concrete, b) less porous concrete.

In order to reduce the porosity, additives can be added to the cement mixture, which acts as a filler or enters into a secondary reaction to form additional hydration phases. The additives vary in size, shape, and quantity used. On the micro-scale (1 - 100 µm), silica fume, fly ash, granulated blast-furnace slag, and others are nowadays commonly used to increase durability and mechanical properties of cement-based materials [2]. Much smaller nanoparticles of 4 nm to 40 nm are also used as additives. These are mainly oxides (nano-$SiO_2$, nano-$Al_2O_3$, nano-$Fe_2O_3$, nano-$TiO_2$) or they are composed of nano-clays, which also change the microstructure of the material and affect the porosity, mechanical properties, and durability [3, 4].

The porosity of cementitious materials can be determined by many methods, one of which is electrochemical impedance spectroscopy (EIS). EIS is a non-destructive method that can observe changes in microstructure and porosity. In contrast to the other industries, EIS is not widespread in civil engineering. In the future, EIS could be used to investigate the local properties of existing structures to assess their durability. Majority of studies deal with corrosion of steel reinforcement [5, 6], chloride penetration into the material [7, 8], the hydration and shrinkage process [9], the influence of mineral admixtures [10], and the cement paste containing carbon nanotubes and carbon fibers [11]. However, EIS can also be used

to determine the porosity of the cementitious material [12–15]. The evaluation of porosity is possible based on Archie's law [16], modified Archie's law [17, 18], and the general effective media model [19].

## 1.1 Thesis motivation and objectives

The primary purpose of the thesis is the application of electrochemical impedance spectroscopy for the detection of changes in the microstructure and porosity of cement-based materials. Microstructural changes affect the mechanical properties and durability of structures. EIS is a non-destructive method, the principle of which is to subject the sample by an alternating electric current into the material and record the impedance. The method is not common and sufficiently explored in civil engineering, such as in the industries involved in biosensors, battery development, fuel cell development, and physical electrochemistry [20]. Therefore, research of this topic is beneficial. The individual research objectives are as follows:

- To design and manufacture several cement pastes/mortar mixtures modified with nano-additives with varying porosity.

- To design and manufacture samples with geometry applicable for EIS measurement.

- To determine the electrical properties of designed mixtures by electrochemical impedance spectroscopy at different hydration times.

- To evaluate the porosity from EIS measurements using analytical models.

- To compare porosity measured by EIS with porosity determined by other commonly used methods: scanning electron microscopy, gravimetric method, mercury intrusion porosimetry, and helium pycnometry.

# 2 Materials and microstructure characterization

This chapter describes properties (especially size), production of Portland cement, and nanoparticles used in this thesis. It also discusses the hydration reaction and the morphology of pure cement paste's main hydration products, including the porosity, composition, and conductivity of the pore solution. Attention is given to the effect of the addition of nanoparticles in the mature cement paste, which enter into a secondary reaction with the already formed products.

## 2.1 Raw materials

a) CEM I 42.5R        b) Nano-$SiO_2$        c) Nano-$Al_2O_3$
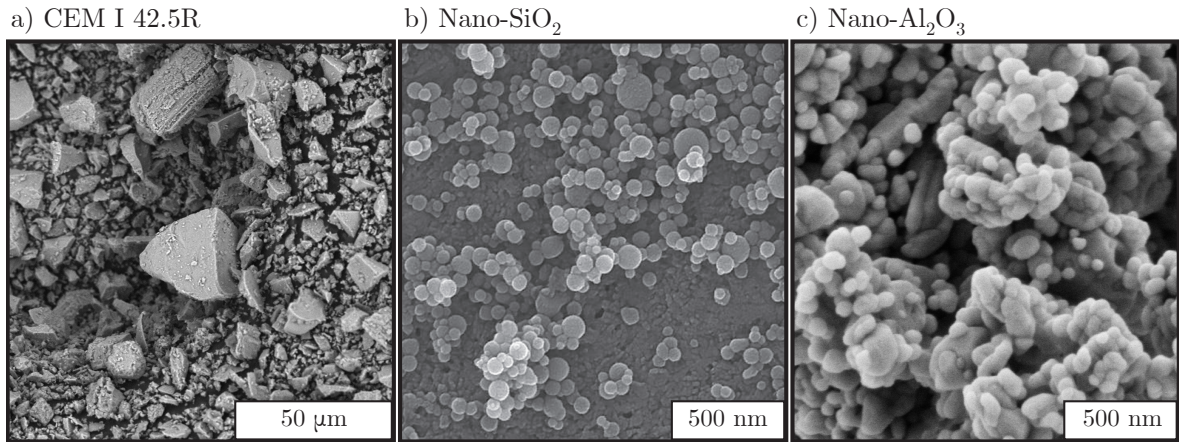


Figure 2.1: SEM-BSE image showing a) cement CEM I 42.5R particles, b) nano-$SiO_2$ [21], and c) nano-$Al_2O_3$ [22].

### 2.1.1 Portland cement

Concrete is the second most consumed construction material in the world after water. Portland cement is major component of concrete, shown in Figure 2.1a [23]. Cement is produced especially from limestone and clay by several process steps, which it is well-described in [24, 25]. Average size of spherical cement particles is 5 - 50 µm and the specific surface area ranges between 300 - 500 $m^2$/kg [26].

The ordinary Portland cement (OPC) is composed of main clinker mineral phases: tricalcium silicate ($C_3S$), dicalcium silicate ($C_2S$), tricalcium aluminate ($C_3A$), and tetracalcium aluminoferrit ($C_4AF$). Other components like gypsum ($CSH_2$) and MgO are also found in the cement [25].

### 2.1.2 Nanoparticles

Supplementary cementitious materials (SCM) with different shapes, sizes, phases (powder or colloidal solution), and amounts are usually added to cement paste or concrete. For example, silica fume, fly ash, and granulated blast-furnace slag are the most widespread particles on

the micro-scale (particle size ranging from 1 - 100 µm, with a specific surface area of typically 15 - 30 $m^2/g$ [27]), while nanoparticles (NP) with specific surface area ranging from 60 - 600 $m^2/g$ [28] are not that common. In most research, NPs of the 4 - 40 nm scale range are used [3], but in some cases nanoparticles with size 40 - 100 nm were used [3]. Many types of NPs are added to the cement-based material, for example: nano-$SiO_2$, nano-$Al_2O_3$, nano-$TiO_2$, nano-$Fe_2O_3$, nano-$CaCO_3$, zeolites, nano-clays, nano-fly-ash, graphene oxide, carbon nanotubes and fibers [3, 4].

**Nano-SiO$_2$**

Nano-silica is spherical shaped particles as shown in Figure 2.1b. It is abundantly used as a powder or as a colloidal suspension. There are three main methods to manufacture nano-$SiO_2$, two of them are described in Figure 2.2.

a) Sol-gel process       b) Olivine process

| Sol-gel process | Olivine process |
|---|---|
| Ingredients | Olivine |
| Reaction mixtures (stirring) | Crushing & screening |
| Colloidal SiO$_2$ | Neutralization ← Acid |
| Gelation & Aging | Decantation → Inert mineral |
| Heat drying | Silica filtration → Residual solution |
| Silica powder | Silica powder |
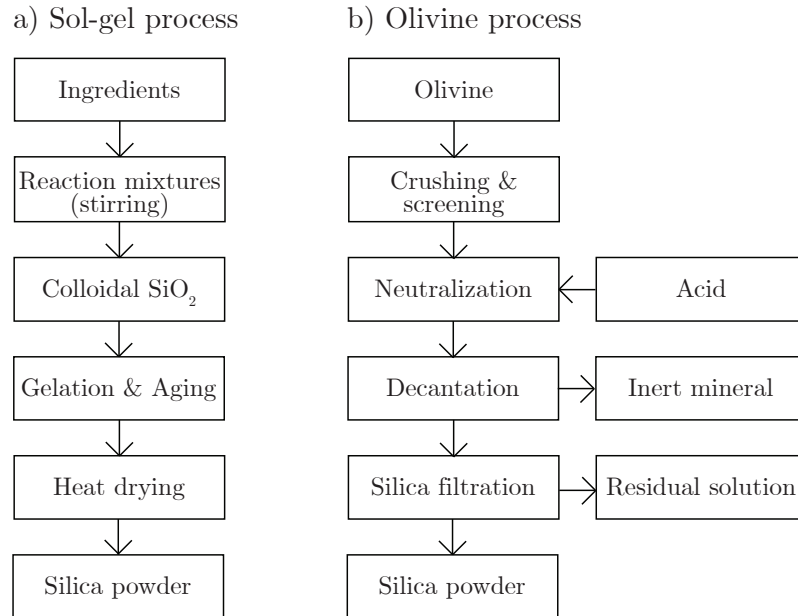
Figure 2.2: Production of nano-$SiO_2$ by a) sol-gel process [29], b) olivine process [30].

The first method is **flame hydrolysis**. The main product is called pyrogenic silica with a specific surface area in the range 100 - 200 $m^2/g$ [31].

The second method is called **Sol-gel process** or **Neutralization** of a sodium silicate solution with acid, most commonly sulfuric acid. Gradually, a sodium silicate solution is added to the acid, forming a gel. Subsequently, the gel is dried and milled. Production of sodium silicate solution is relatively demanding (occurs at 700 °C). Therefore the cost of the final product is high [32, 33].

The third method - **olivine process** is an alternative method to the Sol-gel process. It uses olivine as an entrance material to the neutralization in sulfuric acid. Precipitation of silica occurs in a short time at temperature 50 - 95 °C. The specific surface area of olivine nano-silica is 100 - 500 $m^2/g$, and a very high purity of 99 % is provided. This method is the least costly and has the lowest environmental impact [34, 35].

**Nano-Al$_2$O$_3$**

Nano-Al$_2$O$_3$ is spherical shape particles as shown in Figure 2.1c. It is made by various methods from corundum. The type of $\alpha$-Al$_2$O$_3$ varies in physical properties from the other types due to the different manufacturing processes summarized in Figure 2.3.

a) Combustion method          b) Precipitation method          c) Hydrothermal method
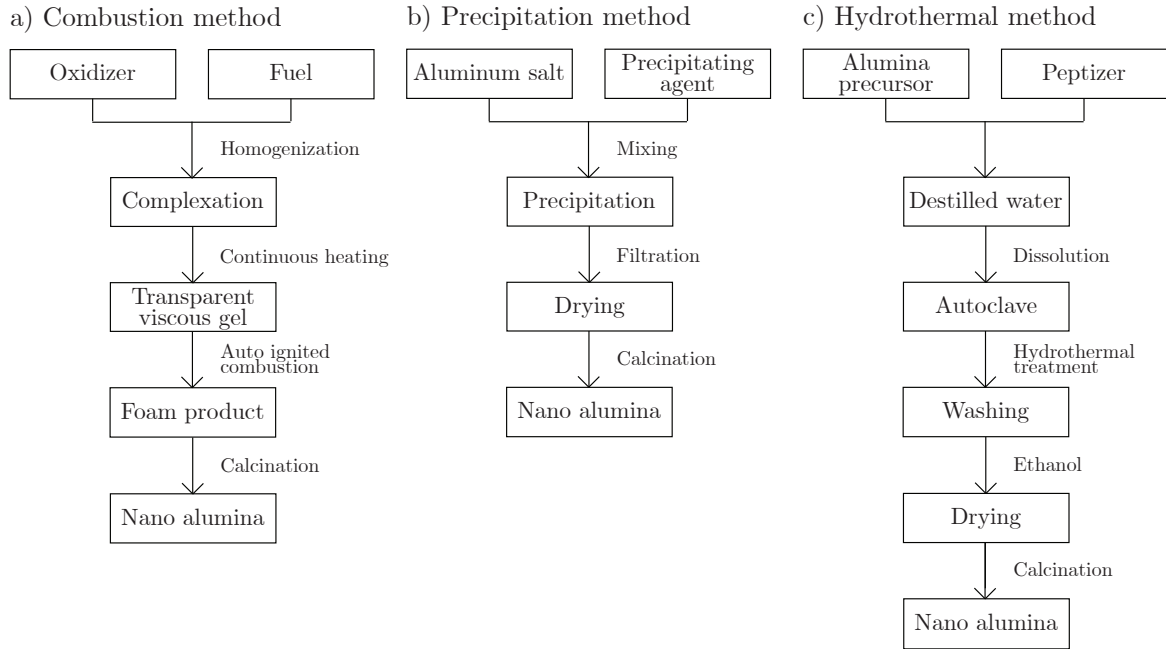


Figure 2.3: Nano-Al$_2$O$_3$ manufacturing processes: a) combustion method, b) precipitation method, c) hydrothermal method [29].

The first method is a low-cost simple **aqueous sol-gel process**. The method has the same process as described for nano-silica manufacturing. It uses various types of acids (for example acetic acid, and citric acid) or ethanol as solvents. It takes place at a temperature of 1000 °C or higher [36, 37].

The second method - **combustion synthesis** is relatively fast and cheap. Combustion synthesis can use a solid, liquid, or gaseous form of reactant. The gas phase used for combustion is the least efficient. Synthesis uses glycine as fuel and aluminum nitrate as an oxidant to ensure the production of pure foam $\alpha$-Al$_2$O$_3$ from nanoparticles are produced by calcination at 1100 °C [38].

**Precipation method** is attractive due to the use of inorganic precursors (chlorides, nitrates, sulfates) and precipitating agents. Ammonium acid carbonate acts as a precipitator in the process of $\alpha$-aluminum synthesis [39].

The principle of **Hydrothermal synthesis** is based on crystallization of anhydrous materials from an aqueous solution under elevated temperature and pressure. This synthesis is performed only in one complex step (without high temperature during calcination) in autoclaves [29].

The last method is **leaching method** of kaolin. Kaolin is a natural material containing 20 - 26% alumina [40]. The impurities of kaolin can be removed by filtration with hydrochloric

acid [41] or sulfuric acid [40] as a leaching agent. Precipitation in ethanol is an intermediate step between filtrations. $\gamma$-aluminum is synthesized by this method. The nanoparticles have a proper size, high surface area, and crystallinity.

## 2.2 Microstructure of cement based materials

### 2.2.1 Hydration of pure cement paste

Portland cement is composed of four main clinker minerals - $C_3S$, $C_2S$, $C_3A$, $C_4AF$, gypsum and other minor components. When the cement is mixed with water, highly soluble clinker minerals (especially $C_3S$, $C_3A$ and $CSH_2$) dissolve ions into the mix water. Then supersaturation of the pore solution happens. Therefore, it is energetically advantageous to precipitate ions in solution into new solid phases called hydration products. These precipitated ions leave space for further dissolution of more ions. Thus, the process can continue to precipitate [42].

Individual clinker minerals form different solid phases. These solid phases occur in the same pore solution. Therefore studying their separate reactions is enabled by an approximation of the overall hydration behavior of cement. $C_2S$ and more abundant $C_3S$ form calcium silicate hydrate (C-S-H) gel phase and crystalline calcium hydroxide, Portlandite (CH), according to the following equations:

$$C_3S + (1.3 + x)\,H \rightarrow C_{1.7}SH_x + 1.3CH, \qquad (2.1)$$

$$C_2S + (0.3 + x)\,H \rightarrow C_{1.7}SH_x + 0.3CH. \qquad (2.2)$$
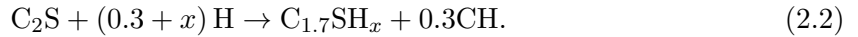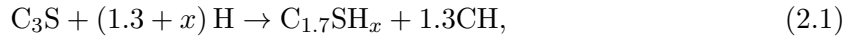
The main equation of hydration reaction includes variable $x$. It represents the amount of water entering to the reaction. $C_3S$ contributes primarily to the early development of strength, while $C_2S$ is involved in the strength development of mature cement paste [24].

Instantly after mixing water and $C_3A$, a hydration product called hydrogarnet is formed. It causes a setting almost immediately. This phenomenon is known as a flash set. However, this is undesirable because it decreases workability or makes it almost impossible. Therefore, gypsum is added to the cement mixture to delay setting. The product formed from $C_3A$, gypsum and water is called ettringite ($C_6AS_3H_{32}$). It is quite unstable product and it converts to monosulfoaluminate ($C_4ASH_{12}$). $C_4AF$ reacts in a similar way as $C_3A$ but a little slower. Final hydration products also contain ferrite, which partly replaces aluminate. For simplicity and because of their fluctuating chemical composition, these products are called AFt and AFm [43].

### 2.2.2 Degree of hydration and microstructure development

The hydration of the cement paste is described by the degree of hydration (DoH, $\alpha$), which indicates the percentage of hydrated cement particles. DoH values range from 0 (no cement particles reacted) to 1 (complete hydration of all cement particles), see Figure 2.4a.

During the hydration of cement, an exothermic reaction occurs. It produces the so-called hydration heat [43]. Hydration heat is generated by the reactions of all four main

clinker minerals. The example of the rate of hydration heat evolution of OPC is shown in Figure 2.4b. Immediately after mixing, rapid and highest hydration heat production occurs due to the $C_3A$ reaction and the rapid formation of a layer of hydration product around the cement particles. The second significant heat development is due to the $C_3S$ reaction. It is affected by the temperature and the average particle size of cement. Approximately 30% of the initial cement hydrates within 1 day. Reactions slow down as the layer of hydration product around cement particle grows. This part of reaction is called the diffusion-limited reaction period [25].
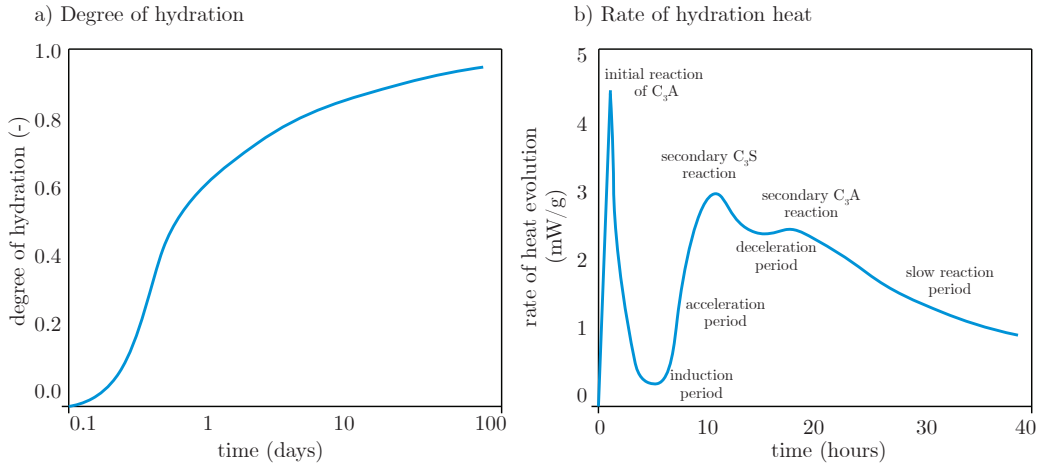


Figure 2.4: a) Degree of hydration [25], b) rate of heat evolution of OPC [25].

DoH can be derived experimentally or by using computer models [44]. An experimental approach as isothermal calorimetry quantifies the individual microstructural phases to determine DoH [45]. The hydration result can be further observed, e.g. by scanning electron microscopy or $\mu$CT. A computer-generated material structure can be distinguished by two types of models: vector and digital microstructural models.

Vector models simulate particles as centroids with different radii and hydration as particle growth with overlaps. Hymostruc3D [46] and $\mu$ic [47] are the most commonly used models, see Figure 2.5a. Jennings and Johnson model [48], the Navi and Pignat model [49], the Nothnagel and Budelmann model [50], the Wang et al. model [51] and the Ducom model [52] are another vector models used for DoH determination. In Hymostruc3D, the particles gradually dissolve as hydration proceeds and inner and outer hydration products form around them. This model is influenced by the particle size distribution of clinker, the amount of water, and the temperature [46]. Another vector model, $\mu$ic, works with an efficient calculation of spherical grain overlap and offers the flexibility of setting [47].

Cemhyd3D [53] and HydraticCA [54] are computer-digital models that illustrate the microstructure using cubic voxels (volume element). The cubic voxels represent the individual phases (anhydrous cement particles, pores, or hydration products), as shown in Figure 2.5b. It reflects chemical composition, particle size distribution, curing condition, and temperature. The voxels act like real phases, including dissolution, diffusion, transportation, and formation of new hydration products. Cemhyd3D represents particles as multiphases, multi-size, and

a) Hymostruc3D
b) Cemhyd3D
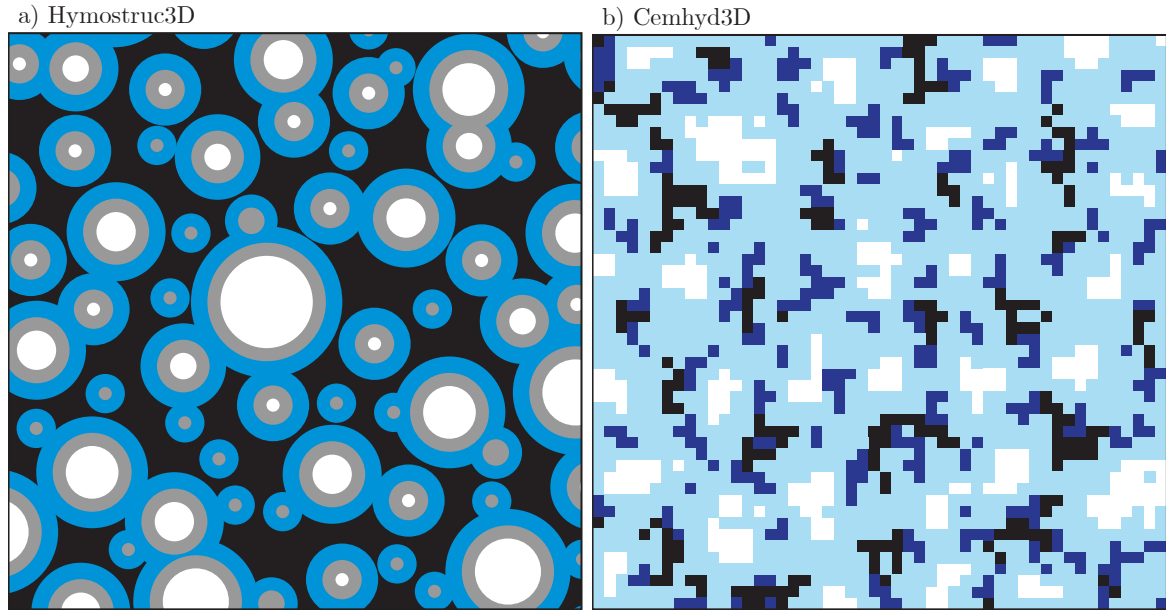


Figure 2.5: 2D slice from of microstructure of cement paste simulated by a) Hymostruc3D [44], b) Cemhyd3D [44] (white = anhydrous cement grains, light blue = C-S-H gel, dark blue = Portlandite, blue = outer products, grey = inner product, black = pores).

irregular elements. A finite element approach is used to calculate mechanical properties simply and efficiently. The degree of hydration and the real hydration time can be determined from Cemhyd3D. However, due to the limitations of the method, the real hydration time may be misrepresented. Therefore this value is not recommended for further use [44, 55].

### 2.2.3 Morphology of cement paste

As mentioned above, C-S-H gel, Portlandite, AFt, AFm, and other hydrates form simultaneously and therefore affect each other. Therefore, it is difficult to distinguish the individual phases and the boundaries between them at the microscale (100 nm - 100 µm). The C-S-H gel is often mixed with other hydration products forming inner and outer products. The inner product is a high-density C-S-H gel with an internal system of tiny pores - gel pores are described in Section 2.2.4. The inner product is created around the unhydrated cement particles. The outer product was located between the cement clinker particles. And the space that was originally occupied by capillary pores forms a continuous phase covered by the inner product. The outer product contains low-density C-S-H gel mixed with other hydrates [25].

The most important hydration products are considered to be inner products, outer products, unhydrated cement particles, Portlandite, and capillary pores [2], which can be seen in the scanning electron microscope (SEM) with a backscattered electron (BSE) detector at polished samples surface with a magnification of about 300× - 5000× as shown in Figure 2.6a. These SEM-BSE images can be further used for image analysis to get the volume fraction of the main hydration phases [2], see Figure 2.6b. The unhydrated clinker, inner and outer products contribute to the mechanical properties of mature cement paste. Also, Portlandite provides mechanical properties, but if it gets into contact with fresh water, CH will leach

a) SEM-BSE image                                    b) Image analysis
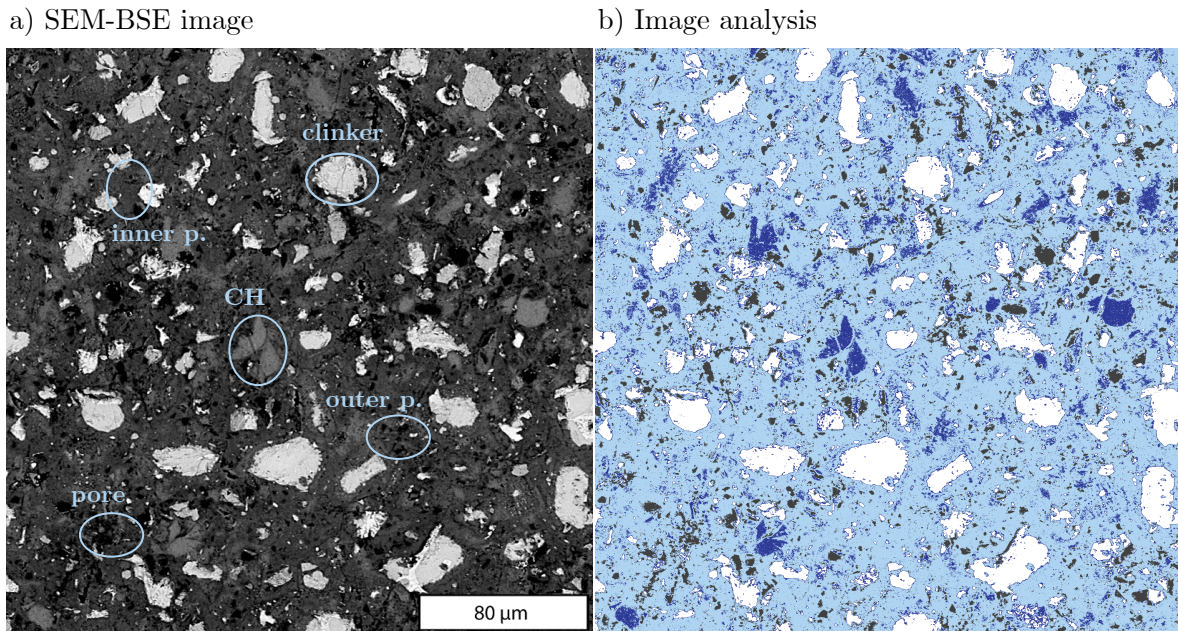


Figure 2.6: a) Typical SEM-BSE image of ordinary cement paste showing the individual phases at a magnification of 400×, b) example of image analysis with individual phases: pores/cracks (black), main hydrates (light blue), CH (dark blue), clinker (white).

out and as a result, it increases porosity and reduces durability. Capillary pores cause higher porosity, reduce the durability and mechanical properties of mature cement paste, and are described in more detail in Section 2.2.4 [24].

### 2.2.4 Porosity

Porosity is an integral part of cement-based materials at the micro-scale that influences strength and durability [56]. The measurement of porosity depends on the characteristics of the pores. The pore characteristics differ in size, shape, and distribution in the solid matrix, which determines the properties of mature cement. Generally, three types of pores can be found in hydrated cement paste - capillary pores, gel pores, microcracks/air voids [25]. The distinction of pore types and their exact size boundaries is not strictly defined and serves for practical separation and nomenclature.

The first and the finest type is **gel pores** ranging from 0.5 nm to 10 nm (up to 100 nm). It occurs in C-S-H gel and influences shrinkage and creep. Water in gel pores is non-evaporable in ordinary conditions. Part of the gel pores is called interlayer spaces, see Figure 2.7, which are adsorbed between C-S-H gel particles (physically bound water). Interlayer spaces are smaller than 0.5 nm and differ in two ways compared to gel pores. The first difference is that water in them is not liquid but chemically bound and therefore cannot be removed even by vacuum drying, and the second difference is the tight binding between the water molecules in the C-S-H gel structure.

The second type, **capillary pores**, with dimensions from 10 nm to 10 µm, occur in the space formerly occupied by the mix water. The hydration product increases in volume during
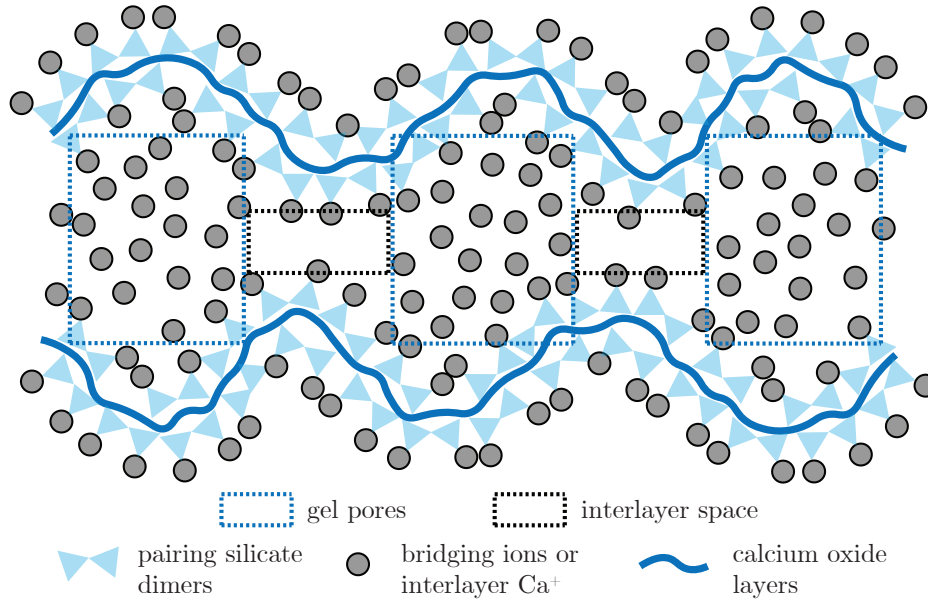
Figure 2.7: Schematic representation of gel pores and interlayer space in C–S–H by winding calcium oxide layers [57].

the hydration, consuming the free water and taking its place. These pores are interconnected and surrounded by low-density C-S-H gel. Capillary pores contain evaporable water and the permeability. Strength of the cementitious material decreases as their volume increases. This type of pores overlaps the size of gel pores, making the pore spectrum continuous.

The third and the most significant type of pores are the **microcracks and air voids**. Microcracks are formed due to a shrinkage process, mechanical stress from external loads, other environmental influences (as temperature), and, in the case of massive structures, as a result of tension stress due to the development of hydration heat. Microcracks range in diameter from about 10 µm to 200 µm in diameter. Air voids range in size from micrometers to millimeters and are caused by mixing technology and imperfect placing. All these types of pores contain bulk water, affect the permeability and strength of cement-based materials [43].

### 2.2.5 Pore solution

Instantly after mixing the cement with water, the ions of individual cement elements dissolve into the pore solution. The concentration of the dissolved ions varies widely depending on the composition, solubility, and ratio of all components, curing conditions, temperature, and hydration time. A plasma spectrometer is a sensitive instrument used to analyze pore solutions. It can distinguish the ions $Na^+$, $K^+$, $S^+$, $Ca^+$, $Si^+$, $Al^+$, $Fe^+$, and $Mg^+$ in the solution. Sodium ($Na^+$) and potassium ($K^+$) are alkalis that are present in high concentrations in the pore solution and have a positive charge. Therefore, hydroxyl ions ($OH^-$) balance the overall charge of the pore solution. The alkali prevents the dissolution of the main hydration products in cement due to a pH of approximately 13 [25].

Vacuum filtration or centrifugation can be used to extract pore solution during the first

hours of hydration. High pressure is required to obtain the pore solution from the hardened cement paste of common water to binder (w/b) ratio ($\ll 1.0$). The used pressure significantly affects the composition of the pore solution (due to too high pressure, a larger volume of ions can be observed in the pore solution than the number of ions is actually present). The amount of applied pressure depends on w/b ratio, age, and the material. The pressure of about 250 MPa is usually sufficient for an adequate amount of the pore solution of the cement paste, but higher pressures are necessary for mortar and concrete [58].

**Conductivity of pore solution**

The composition of the pore solution affects its conductivity, which is closely related to its electrical properties and the diffusive ionic transport. The conductivity of the pore solution can be determined by the direct method. It can be used only for early-age samples and samples with a high w/b ratio. As an additional method, for example, ion chromatography can be used [59].

The expected volumes of the pore solution and potential moles of available alkali ions can be computed by a virtual rapid chloride permeability test (RCPT). Generally, it has a reasonable agreement with the experimental test results, and it is used in the conductivity estimation proposed by Bentz [60]. $OH^-$, $Na^+$, and $K^+$ ions are considered to be the most significant contributors to the conductivity of the pore solution due to their high equivalent conductivity and high abundance in the solution. The $Ca^{2+}$, $SO_4{}^{2-}$, and other ions can be neglected, because they have much lower concentrations or mobility compared to $OH^-$ [61]. Thereby, Snyder et al. [59] developed the procedure to calculate the electrical conductivity of the pore solution $\sigma_0$ based on the concentration of $Na^+$, $K^+$, and $OH^-$ (the highest mobility ions) using the following equation:

$$\sigma_0 = \Sigma_i z_i \cdot c_i \cdot \lambda_i, \tag{2.3}$$

where $z_i$ is the ionic species valence, $c_i$ the ionic molar concentration, and $\lambda_i$ is the equivalent conductivity of each ionic species defined as:

$$\lambda_i = \frac{\lambda_i^\circ}{1 + G_i \cdot I_M^{1/2}}, \tag{2.4}$$

where $\lambda_i{}^\circ$ is the equivalent conductivity of an ionic species at infinite dilution, and $G_i$ is the conductivity coefficient, both summarized in the Table 2.1. $I_M$ is the molar ionic strength depending on $z_i$ and $c_i$ of ion species.

The diffusivity of ions in CBMs depends on the w/b ratio (ranging from 0.3 to 0.5), degree of cement hydration (ranging from 0.6 to 0.9), and weight fraction of silica fume, fly ash, and blast-furnace slag addition (ranging from 0.0 to 0.1) [60].

Pore solution composition (from the elements $K^+$, $Na^+$, and $OH^-$) and conductivity (S/m) for cement-based materials with a known degree of hydration and cement composition can be estimated by the virtual method based on [59, 60] freely accessible on the Internet at National Institute of Standards and Technology (NIST) [62].

Table 2.1: Equivalent conductivity at infinite dilution and conductivity coefficients for sodium, potassium, and hydroxide ions at 25 °C.

| Species | $\lambda°$ | $G$ |
| --- | --- | --- |
| | ($cm^2$ S / mol) | ($(mol / L)^{-1/2}$) |
| $Na^+$ | 50.1 | 0.733 |
| $K^+$ | 73.5 | 0.548 |
| $OH^-$ | 198.0 | 0.353 |

## 2.3 Effect of nanoparticles on cement paste

NPs improve mechanical properties (esp. at early ages) and durability because they have a high specific surface area. The negatives of their use are the high cost and decreased workability of fresh concrete mix (proved by the slump test). The reduction in workability depends on the amount of nanoparticles that absorb the mixture water [63]. Another disadvantage is that NPs tend to make agglomerates in size 100 μm or larger.

There are two cases of why NPs are used as an additive. In the first case, they act as a filling material. It fills the gaps occupied often by water hence it reduces porosity, increases durability and strength. In the second case, they react mainly with Portlandite or potentially with other products in the secondary reaction, which is called the pozzolanic reaction [4].

### 2.3.1 Nano-SiO$_2$

Nano-silica (nS) is not widely used in the civil engineering industry compared to, for example, the mining industry. However, it can improve the durability, transport properties, and mechanical properties of hardened cement - especially compressive, flexural, tensile strength and elasticity modulus. These properties are improved due to pozzolanic reaction:

$$CH + nS \rightarrow CSH. \tag{2.5}$$

During the secondary pozzolanic reaction, the Portlandite reacts with the nano-silica to form additional C-S-H gel that provides the desired material properties. The unreacted silica particles act as a filler agent and occupy the capillary pore space, which enhances the properties [3].

The optimal dosage of nano-silica is about 2% of the cement, and the maximum dosage to increase the mechanical properties is 4% of the cement weight. Further addition of nano-silica reduces the mechanical properties [64]. The phenomenon of lower strength is caused by the agglomeration of nanoparticles [4]. The use of a colloidal solution instead of a powder helps to disperse the particles better. It has a higher hydration acceleration effect on the pozzolanic reaction [65, 66]. Using $SiO_2$ nanoparticles has a 10 times higher pozzolanic reactivity than micro-scale silica fume [67].

Bai et al. [68] found that the specific surface area of nano-silica has an important effect on the porosity of CBMs. At the age of 7 and 28 days, nano-$SiO_2$ with a specific surface area

of 100 m$^2$/g increased the porosity and nano-SiO$_2$ with a specific surface area of 470 m$^2$/g decreased the total porosity.

### 2.3.2 Nano-Al$_2$O$_3$

Cement paste modified by nano-Al$_2$O$_3$ (nA) does not improve any properties up to 7 days of age. New crystalline phases are not developed yet, compressive strength of cement paste does not improve. Nanoparticles only act as fillers, making the microstructure denser [69].

A reaction occurs by adding nano-aluminum to the cement paste. The partial replacement of the cement weight by aluminum produces C-A-S-H (calcium-alumina-silica hydrate) gel according following equations [70]:

$$nA + 3CH + 11H + S \rightarrow C_3ASH_{14}, \tag{2.6}$$

$$nA + 3CH + 29H + 3S \rightarrow C_3AS_3H_{32}, . \tag{2.7}$$
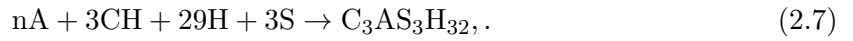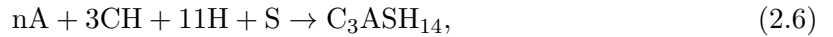
If the amount of aluminum is higher than 2 %, nano-Al$_2$O$_3$ tends to bind with the released lime during hydration and leach out silica from the hydration process. This effect reduces the mechanical properties of mature cement paste [4, 71].

The microstructure of materials is hence heterogeneous and porous [70]. León et al. [72] find out, that the addition of 5 % wt. of nano-aluminum increase medium-size capillary pores (10 - 50 nm), decreases the volume of large capillary pores (50 nm - 10 µm), and can increase the volume of macro pores (larger than 10 µm).

## 2.4 Chloride penetration through cement-based materials

Chlorides are one of the most important substances that affect the durability of concrete. However, in this case it is not dependent on the concrete itself, but on the potential corrosion of the reinforcement. Chloride ions can penetrate through the pores into the cement matrix and negatively affect the durability of the reinforcement's covering layer. The transfer process of chloride ions is caused by diffusion. The diffusion is the movement of (in this case) chloride ions from an area of high concentration to an area of low concentration, i.e. its driving force is a concentration gradient. Fick's first law describes the diffusion through the fully saturated material according to the following equation [13]:

$$-J(x) = \frac{dC}{dt} = D_{\text{eff}}\frac{dC(x)}{dx}, \tag{2.8}$$

where $J$ is diffusion flux density, $C$ is chloride concentration in the pore solution, $t$ is the time, and $D_{\text{eff}}$ is the effective diffusion coefficient. The $D_{\text{eff}}$ is the net flux of chloride without reaction in a porous medium at steady-state conditions and can characterize the long-term resistance to ion penetration into the CBMs. The chloride penetration of CBMs is affected by the diffusion coefficient and the binding capacity of material. The binding capacity is affected by type of the cement, admixtures, and porosity because the quantity of bound chlorides (describes below) depends on the quantity of hydration phases especially formed from C$_3$A, C$_4$AF, and C$_3$S [73].

In cement paste, an overall balance of negative and positive charge is provided by positive and negative ions present in the pore solution such as $OH^-$, $Na^+$, $K^+$, and chloride ions $Cl^-$. Chlorides in hardened cement paste are divided into bound chlorides and free chloride ions, as shown in Figure 2.8 [74].

Bound chlorides occur in CBMs in two variants, either as Friedel's salt (solid chlorides) or as chlorides adsorbed into pore walls [74]. Chlorides are being adsorbed in between layers of the C-S-H gel and are physically adsorbed due to high specific surface of C-S-H gels [70]. Friedel's salt is bound by chemical substitution, which is characterized by a greater binding force. As well as C-S-H gel, AFm phase and unreacted $C_3A$ particles are characterized by high binding capacity [75]. Due to this, Friedel's salt ($C_3A \cdot CaCl_2 \cdot 10H_2O$) is formed [70]. The porosity should decrease with increasing Friedel's salt volume as described in [76]. The addition of up to 3 % wt. nano-$Al_2O_3$ to the cement paste has a positive effect on chloride binding because it reacts with AFm phase to form Friedel's salt [70]. On the other hand, the amount of nano-aluminum less than 1 % wt. reduces the volume of solid chlorides [70].
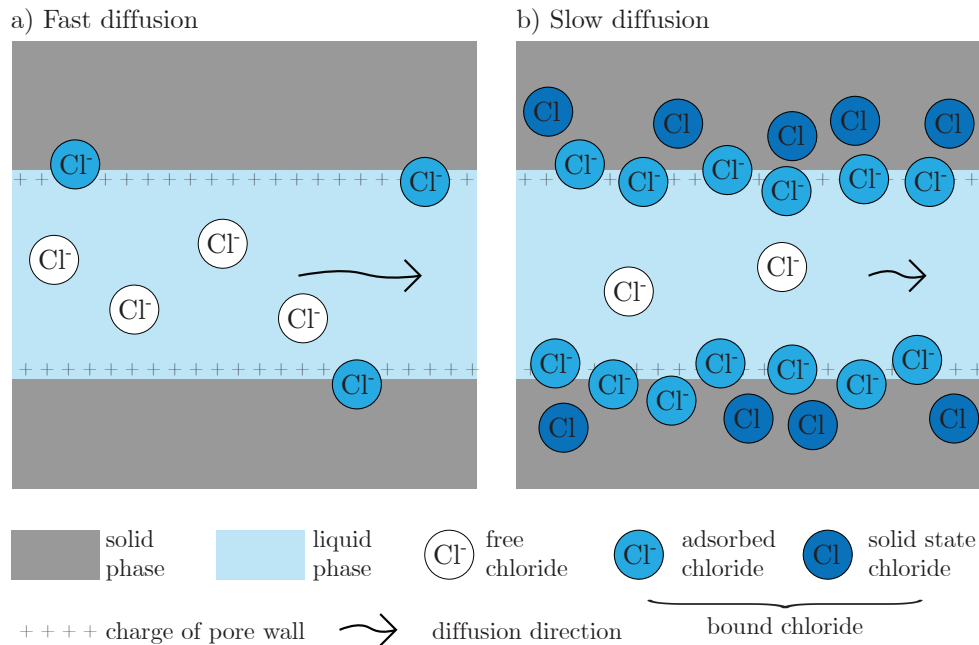


Figure 2.8: Influence of bound chloride volume on diffusion rate a) fast diffusion, b) slow diffusion [74, 77].

Free chlorides dissolved in pore solution can move freely compared to bound chlorides. In contrast, the bound chlorides can not move in ordinary concentration gradient or in a highly alkaline environment in concrete [77]. The pH of which, depending on the designed mixture, is typically in the range of 12 - 13 [78].

A reduction in the pH of concrete can occurs due to carbonation, the diffusion process of carbon dioxide into the material and its subsequent degradation [79]. Then, the bound chlorides are released into the pore solution, increasing the free chloride concentration in the carbonation zone [74]. The reduction of the high alkalinity environment in concrete can result in the corrosion of reinforcement.

The diffusion of chlorides through the CBMs is depended on the complexity of the pore structure (tortuosity and constrictivity). The chloride binding retards the chloride penetration into the material. The increasing volume of bound chlorides slows the diffusion of free chloride ions. Ishida et al. in [80] proposed explanations for this effect. The explanation was based on the assumption that the rate of movement of free chloride ions is retarded by increasing the volume of adsorbed chloride on the pore walls, as shown in Figure 2.8. Therefore, the negative charge of bound ions in the narrow pore space slows down the diffusion rate. An alternative explanation is that as the volume of bound chloride increases, the charge of pore walls in neutralized and the diffusion is driven only by the concentration gradient of free chlorides.

The total volume of chloride can be determined by a variety of experimental tests. For example, the salt ponding test, the bulk diffusion test, the rapid chloride permeability test (RCPT), the rapid migration test, or the sorptivity test can be used. During the test, chloride bounds and moves through the material naturally or, in order to accelerate the process, due to an external influence (e.g. an electric current) [81]. Then, the material is dried and ground. Subsequently, analysis using nitric acid solution and subsequent potentiometric titration is performed. The evaluation of the total chloride volume can then be determined according the following equation [82]:

$$C_{\text{cl}} = \frac{V_{\text{tot}} \cdot C_{\text{titr}}}{m_{\text{s}}} \tag{2.9}$$

where $C_{\text{cl}}$ is the chloride concentration in the sample (free and bound chloride), $V_{\text{tot}}$ is the total volume of the solution used for titration, $C_{\text{titr}}$ is the chloride concentration in the solution, and $m_{\text{s}}$ is the weight of the original powder.

# 3 Methods of determination porosity of cementitious materials

The porosity of cement-based material can be accessed either by direct or indirect methods. Direct methods can measure the pore sizes from the largest pores in the order of a few millimeters to hundreds or tens of nanometers. Direct methods analyze pore structure from 2D or 3D images of the sample. Therefore, these methods depend on the resolution of an image (pixel size). These methods include 2D images of scanning electron microscopy (SEM), 3D images of X-ray microtomography or X-ray nanotomography, and laser scanning confocal microscopy (LSCM) [57].

Indirect methods use liquid (such as water, gas, mercury, helium, etc.) inside cement paste as a probe. The size of the measurable pores is limited by the lower (tens of nanometers) and the upper boundary (hundred of micrometers). Indirect methods of measuring open porosity include mercury intrusion porosimetry (MIP), gravimetric method, and pycnometry. Electrochemical impedance spectroscopy (EIS) can also be ranked as the indirect method because a liquid conducts an electric current and thus is involved in the measurement. [24, 57, 83].
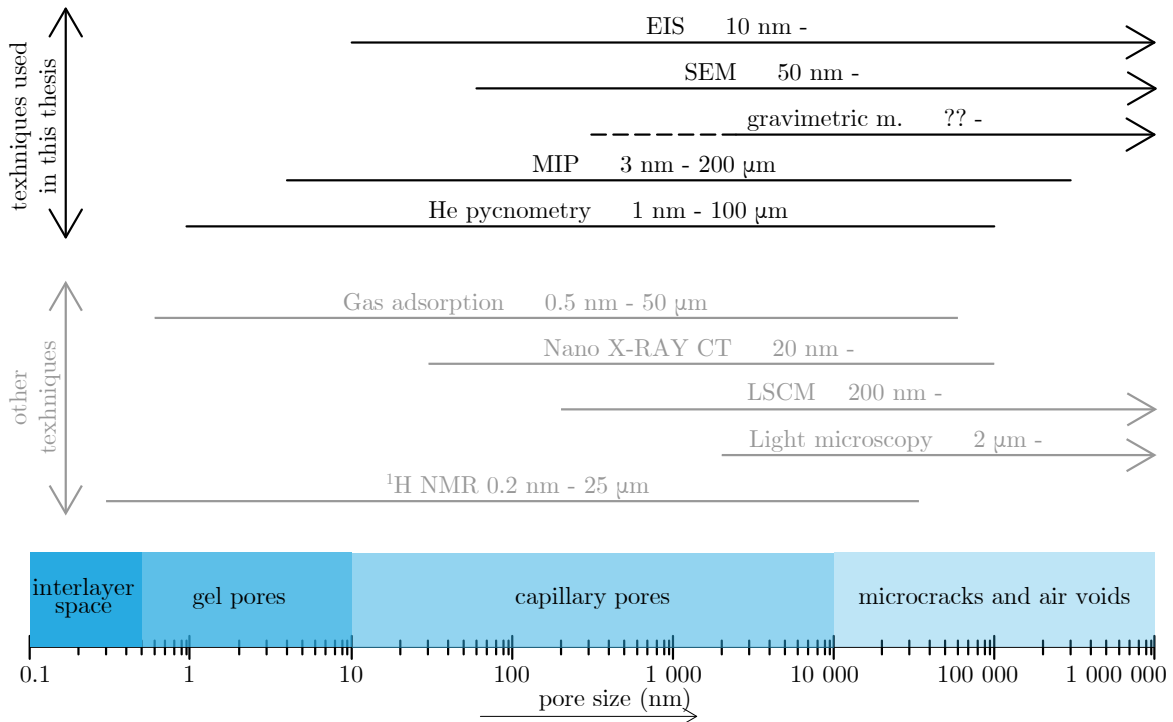


Figure 3.1: Methods of determination the distribution and size of pores in the cementitious material.

## 3.1   Scanning electron microscopy and image analysis

Scanning electron microscopy (SEM) is a method that can be used for the porosity evaluation of cement-based materials. The principle of SEM is based on the emission of a beam of electrons in rows onto the measured area of the sample. The individual components of the inhomogeneous material have different responses to the reflected electrons, which the microscope uses to process the resulting image. The detection of the electron reflection depends on the type of detector used. The first type of detector is the secondary electron (SE), which mainly provides information about the sample's topographical properties. The second type is the back-scattered electron (BSE) shown in Figure 3.2, which records material composition in addition to topographic properties. Using a BSE detector, it is possible to achieve higher microscope resolution than using an SE detector [84]. SEM can also be used for the elemental analysis or chemical characterization of a sample by energy-dispersive X-ray spectrometry (EDS). The atoms on the sample surface are excited by the electron beam, emitting wavelengths of X-ray that are specific and unique for every atomic structure.
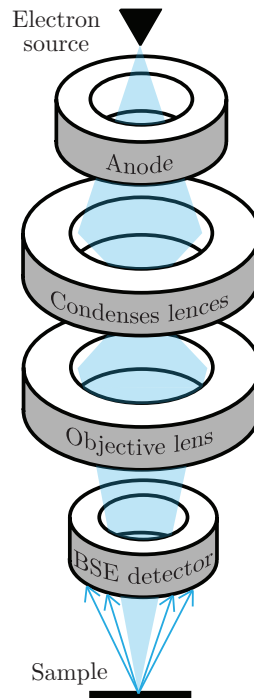


Figure 3.2: The principle of the scanning electron microscope with a back-scattered electron detector.

The ability to identify the pore size of cement-based materials is dependent on the pixel size of the image. The resolution of scanning electron microscopy based image analysis depends on the magnification of SEM. For routine measurements using BSE images, a magnification of approximately 400x is considered sufficient [85]. Image analysis based on the output from SEM-BSE uses 255 gray levels of an 8-bit image, pixels with the same characteristics are displayed with the same intensity of gray [86]. The gray level intervals for separating the hydration products can be obtained by pixel color thresholding. The cement paste is divided

17

at micro-scale (100 nm - 100 µm [2]) into main hydration products, such as unreacted clinker particles; C-S-H gel also containing C-A-H, C-A-S-H; CH; and pores/cracks [87]. By combining SEM-BSE image and image analysis, which are shown in Figure 2.6, it is possible to measure pores in the range of 50 nm [88].

## 3.2 Gravimetric method

The total open porosity of a material is measurable by the gravimetric method and is defined as the ratio of the open pore volume to the total volume of the sample. The volume ($V$) of the sample can be calculated from the equation:

$$V = \frac{(m_w - m_a)}{\rho_w},$$

(3.1)

where $\rho_w$ is the density of water, and is considered as $\rho_w = 998$ kg/m$^3$ at 20 °C. The weight of a sample completely immersed in water (or other reagents) is $m_a$ (so-called Archimedes weight), $m_w$ is the weight of a fully saturated sample as shown in Figure 3.3. The sample can be saturated naturally or in a vacuum of less than 800 Pa.
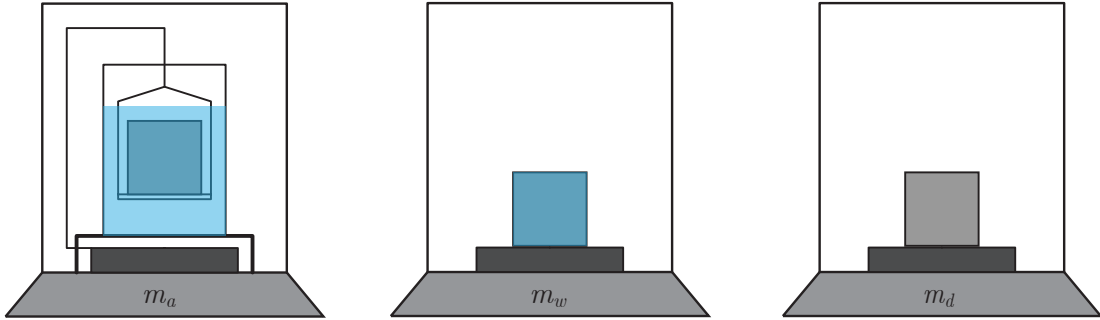


Figure 3.3: Gravimetric method measurement procedure.

Then, the samples are dried in an oven and weighed until the weight is stable. The calculation of the bulk density of the sample $\rho_{g,grav}$ (kg/m$^3$) and the open porosity $\phi_{0,grav}$ (%) is calculated according to the following equations [89]:

$$\rho_{g,grav} = \frac{m_d}{V},$$

(3.2)

$$\phi_{0,grav} = \frac{(m_w - m_d)}{V \cdot \rho_w},$$

(3.3)

where, $m_d$ is weight of dried sample.

## 3.3 Helium pycnometry

Gas pycnometer measures the volume of pores of a material due to the intrusion of a fluid (for example helium, nitrogen, or methanol) into the material. This method is based on a pressure change in a chamber and uses the Boyle-Marriotte law. The most commonly used

type of a pycnometer is a constant-volume pycnometer [90]. Nevertheless, variable volume pyknometer [91] and comparative pycnometer [92] are also used.
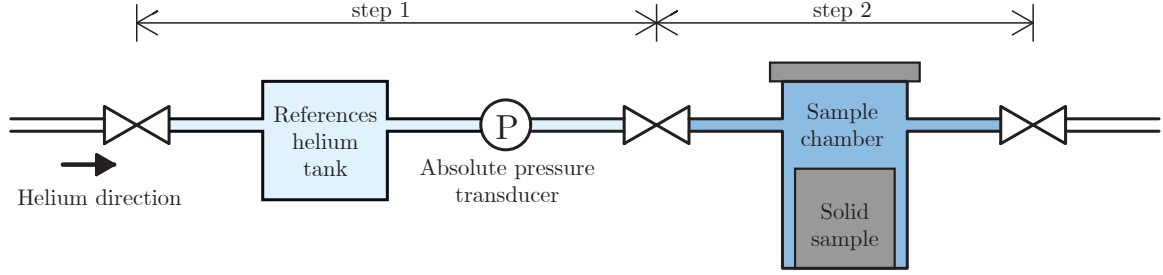


Figure 3.4: Schematic of helium pycnometric device [93].

The constant-volume pycnometer consists of two chambers - a helium tank and a sample chamber, which should be 1.5 - 3 times larger than the tank to achieve the effective range of porosity values shown in Figure 3.4 [94]. The device uses pressures of 50 - 500 kPa. The temperature of the pycnometer is an important factor in the accuracy of the pore volume evaluation, and so is the volume of the chamber. Pycnometry is able to measure the pores connected to the surface through the other. Their range is from 1 nm to 100 µm [95, 96].

The helium pycnometer measures the density of the sample, $\rho$. The porosity of the sample can be calculated according to the following equation:

$$\phi_{0,pyc} = (1 - (\rho_{\text{bulk}}/\rho)) \cdot 100, \tag{3.4}$$

where $\rho_{bulk}$ is the bulk density of the samples determined e.g. by the gravimetric method.

## 3.4  Mercury intrusion porosimetry

Mercury intrusion porosimetry (MIP) is a commonly used method for obtaining the pore size distribution of cement-based materials. MIP can measure pore size in the range of 3 nm - 200 µm. MIP is based on the mercury non-wetting properties (the contact angle for CBMs varies with their mixture and hydration age and ranges from 130° to 140° [97]). The mercury is injected into the dried sample using external pressure, and the change in pressure is recorded. The required pressure increases as the size of the entering pores decreases - large pores are measured at low pressure, as shown in Figure 3.5b, but the closed pores are not measurable regardless of the pressure. High pressure is necessary to measure small pores as shown in Figure 3.5c. However, it can damage the structure of the material.

Pore size can be calculated from the measured pressure using Washburn's equation:

$$d_p = -\frac{4 \cdot \gamma \cdot \cos\theta}{p}, \tag{3.5}$$

where $d_p$ is the pore radius (cylindrical pore shape is considered), $\gamma$ the surface tension, $\theta$ the contact angle and $p$ imposed pressure. For simplicity, $\gamma$ and $\theta$ are assumed to be constant.

By deriving this dependence, it is possible to obtain the pore size distribution curve, namely the increments of pore volume as a function of size [98].

The size of large pores accessed by a small opening can be distorted and registered as small porosity, which results in an overestimation of small pores and an underestimation of large pores. This phenomenon is called the ink-bottle effect. Mercury intrusion porosimetry does not register the largest capillary pores due to the upper limit of measurements. Since the measurements are made on dried samples, the pore structure may change during the drying process, which may cause inaccuracy in the recorded data [25, 99, 100].
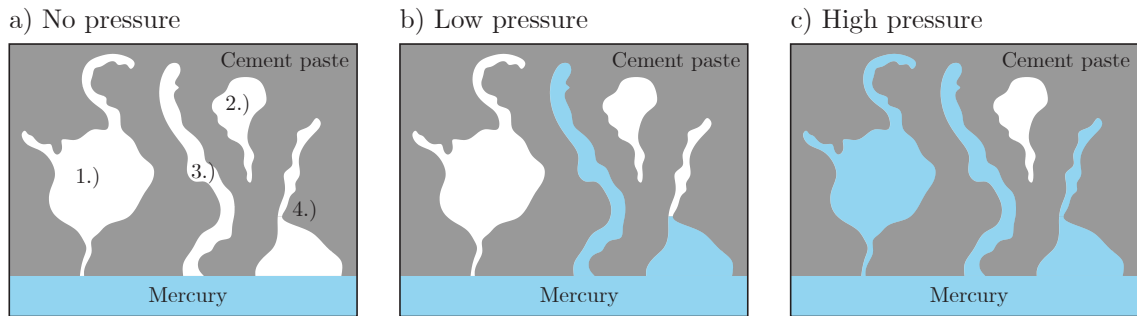


Figure 3.5: Intrusion of mercury into a pore material (cement paste) depending on the applied pressure, 1.) pores accessible by a small opening, 2.) closed pores (inaccessible to the surface), 3.) capillary pores, 4.) small pore opening resulting in an ink bottle effect.

# 4    Electrochemical impedance spectroscopy

Electrochemical impedance spectroscopy (EIS), otherwise known as alternating current impedance spectroscopy (ACIS), is a non-destructive method used to measure the resistance of materials, including cement paste and concrete [12, 25]. Electric alternating current (AC) is applied to the samples by a pair of electrodes embedded in the material or attached to their opposite surfaces. The transmitted current with the periodic alternating signal can be decomposed into a series of harmonic signals of sinusoidal shape with different frequencies due to fast Fourier transform [101, 102]. The measurement is taken from the highest frequencies to the lowest (typical range 10 MHz - 1 Hz for cementitious materials [8]), and the impedance is recorded [6, 12].

Application of EIS in cementitious materials detects the corrosion process of reinforced concrete [5, 6], the diffusion of chloride in concrete [7, 8], the hydration and shrinkage process [9], the porosity and the microstructure of concrete [12–15], the influence of mineral admixtures on cement-based material [10], and the cement paste with added carbon nanotubes and carbon fibers [11].

## 4.1    Equivalent circuit models for concrete

Cement-based materials cannot be considered as a single electrical resistor in EIS measurements because the material consists of a bulk matrix, unhydrated clinker, aggregates, and pores that may be empty or filled with a pore solution. Several researchers have proposed different models for the microstructure of CBMs, although most of them interpret the behavior of EIS unconvincingly. For example, the model for concrete proposed by Whittington et al. [103] contains three conductive paths: aggregate, cement paste, and interface of aggregate and paste. Although, the influence of the conductive path of the aggregate is very small in concrete because the cement paste layer interferes with the interconnection of the aggregate particles. In some cases, the resistances depend on the applied current, indicating unsuitable models (e.g. multi-layer [14], multi-cube [14], and "T" model [104]). One of the most complicated circuit models is the model proposed by Macphee et al. [105]. This model consists of conductive paths of continuous pores, discontinuous pores, hydration products, and unreacted cement particles. Resistance and capacitance extraction using this model is very difficult due to its complexity. The model is impractical in application because the conductive path of the unreacted cement particles is unimportant and has a negligible contribution to current conduction.

**Equivalent circuit models proposed by Song**

Based on above mentioned models, Song et al. [12] established a new model that is based on conductive paths in cement with respect to the pores. EIS is not able to record all types of pores, which vary in shape, size, and distribution in the cement paste structure. For example, capillary pores can be recorded because they are connected and have an elongated

shape, whereas spherical enclosed pores are not measurable [25]. Electrochemical impedance spectroscopy allows measuring only the capillary pores in CBM, and three conductive paths are distinguished as shown in Figures 4.1:

- Continuous conductive path (CCP) - Series of capillary pores connected by pore necks form CCP. The impedance of this path $Z_{ccp}$ equals the resistance of interconnected capillary pores $R_{ccp}$:

$$Z_{ccp} = R_{ccp}. \tag{4.1}$$

- Discontinuous conductive path (DCP) - The continuity of a capillary path is disturbed by a discontinuous point (DP) formed by a thin layer of cement paste. DP is considered to be a double parallel capacitor with electric capacitance $C_{dp}$. The resistance of the capillary path is labeled as $R_{cp}$. The impedance of the path $Z_{dcp}$ is composed of $C_{dp}$ and $R_{cp}$ connected in series as shown the following equation:

$$Z_{dcp} = R_{cp} + C_{dp}. \tag{4.2}$$
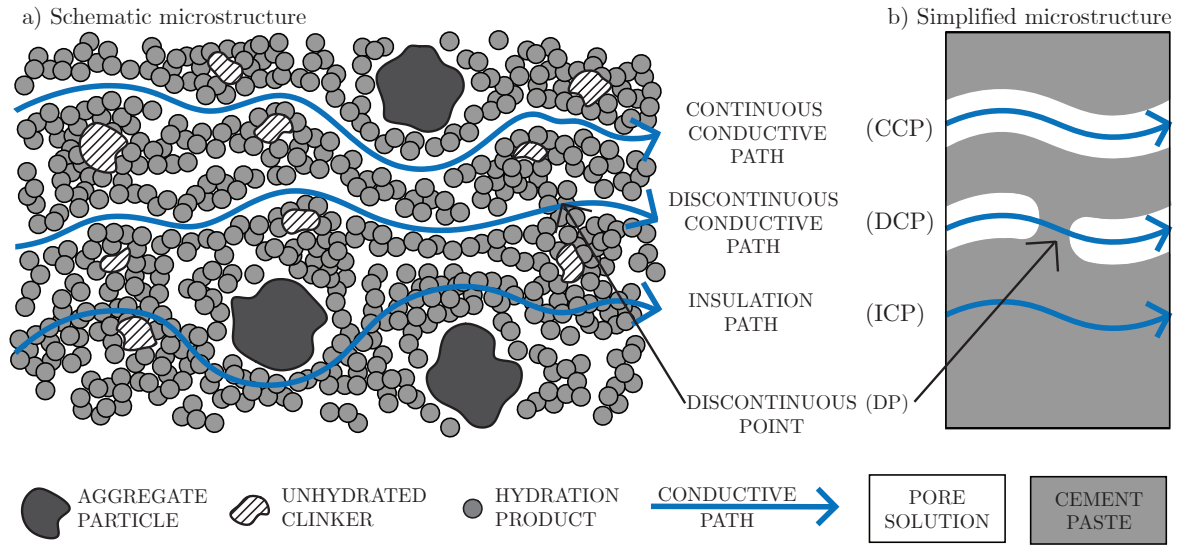


Figure 4.1: a) schematic representation of microstructure and b) simplified microstructure of concrete with illustrated conductive paths.

- Insulator conductive path (ICP) - The pores and voids do not form the largest part of cement paste. It is made up of a bulk matrix that acts as an electric insulator. The matrix becomes charged as a result of the current passing through the sample. Therefore it is considered a double parallel capacitor with capacitance $C_{mat}$. Although cement paste is not a perfect insulator, its resistance $R_{mat}$ can be neglected if the sample is not frozen or dried. Thus, the impedance of this path $Z_{icp}$ is just equal to the $C_{mat}$:

$$Z_{icp} = C_{mat}. \tag{4.3}$$

According to the typical Nyquist diagram (plot of real $Z_{re}$ versus imaginary $Z_{im}$ part of impedance), capacitive loops occur in cement-based materials as shown in Figure 4.2b. These loops can be replaced by parallel series of resistors ($R$) and capacitors ($C$). An equivalent electric circuit containing $R$ and $C$ is necessary to use in order to evaluate the results of EIS measurement [106, 107]. Many equivalent circuits based on various conductive paths have been published and are summarized in [107].

Guangling Song in [12] published two different equivalent electric circuit models that were used in this thesis. The first option is the equivalent circuit model (EC), which is composed of all the above-mentioned paths, as shown in Figure 4.2a. The capacitance of the solid matrix of cement paste is relatively low. Therefore the second option assumes the simplification that $C_{mat}$ does not have to be considered in the second equivalent model, as shown in Figure 4.2c.
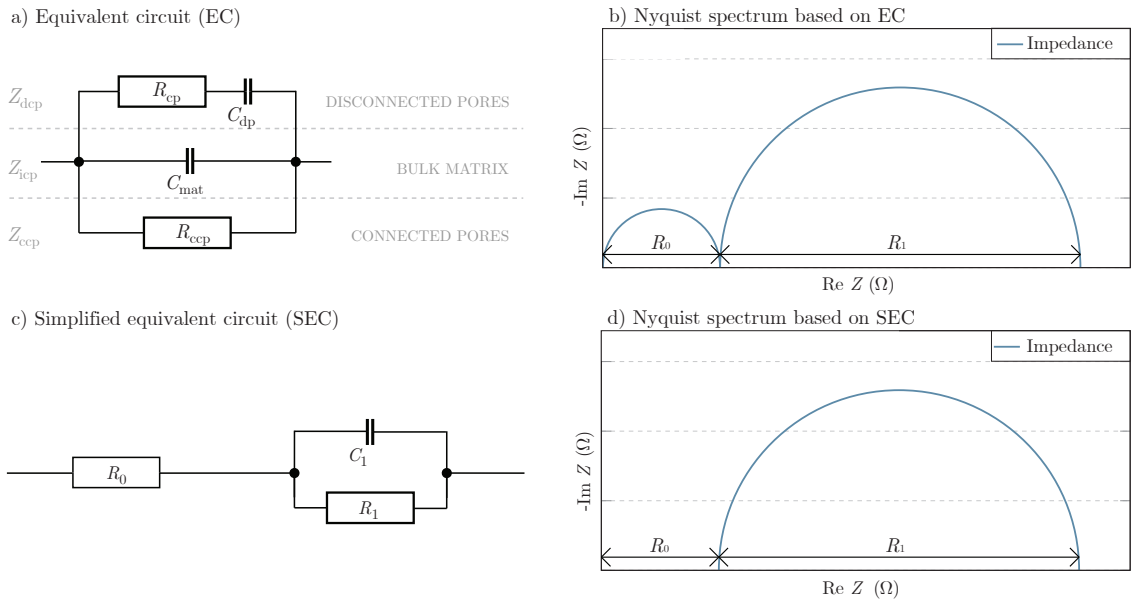


Figure 4.2: a) Equivalent circuit model (EC), b) theoretical Nyquist EIS spectrum based on a equivalent model EC, c) simplified equivalent circuit model (SEC), d) theoretical Nyquist EIS spectrum based on a equivalent model SEC [12].

Furthermore, the electric circuit can be simplified into the simplified equivalent circuit model (SEC) as shown in Figure 4.2c. Comparing the equivalent models in Figures 4.2a and 4.2c, the following relations can be deduced [12]:

$$R_0 = \frac{R_{cp} \cdot R_{ccp}}{R_{cp} + R_{ccp}}, \tag{4.4}$$

$$R_1 = \frac{R_{ccp}^2}{R_{cp} + R_{ccp}}, \tag{4.5}$$

$$C_1 = \left(1 + \frac{R_{cp}}{R_{ccp}}\right)^2 \cdot C_{dp}, \tag{4.6}$$

where $R_1$ is resistance of (continuous and discontinuous) pores and $C_1$ is capacitance of bulk cement (including $C_{dp}$) and $R_0$ is an offset resistance from the origin on real axis of Nyquist diagram.

The theoretical Nyquist spectrum of EIS consists of arcs. The arc of diameter $R_1$ in the EC model is the most important (due to its size and the fact that the accuracy of data measured at high frequency is low), see Figure 4.2b. The SEC model contains only arc $R_1$ as shown in Figure 4.2d. The position of the center of the arc on the horizontal axis $Z_r$ is given by the rotation by the depression angle ($\alpha$) [108], which is related to the pore size distribution and the others imperfection of the sample [6]. $R_0$ can be neglected because high-frequency measurement (nearly to the origin on the real axis of the Nyquist plot) is negatively influenced by surrounding phenomena and accuracy limitation of most electrochemical equipment [12, 61, 108].

**Equivalent circuit model proposed by Cabeza**

Another equivalent circuit model was proposed by Cabeza et al. [109]. The model is composed of two parts. The first part containing the capacitance $C_1$ is defined for the solid phase and the second part is associated with the liquid phase filling pores and is described by capacitance $C_p$ and resistance $R_p$ as shown in Figure 4.3. The double layer capacity $C_p$ is formed at the C-S-H gel, and capacitance at other hydration products (Portlandite, AFt, and AFm) are neglected in the model. The parameters $C_p$ and $R_p$ exponentially change as the sample dries off - with weight loss, capacitance decreases and resistance increases, while parameter $C_1$ has a constant value during drying. The Cabeza model deals with a wide range of frequencies (100 kHz - 15 MHz).
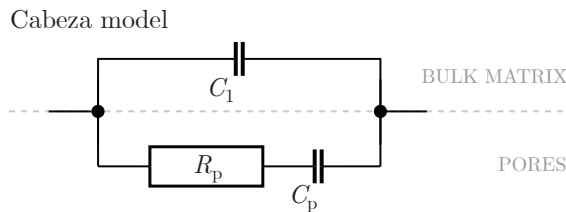


Figure 4.3: Equivalent circuit model proposed by Cabeza [109].

**Equivalent circuit model proposed by Covelo**

Covelo et al. [110] presented an equivalent electric circuit model shown in Figure 4.4. Covelo model consists of a resistance $R_e$, which corresponds to the conductivity of the external solution and high-frequency limit on the impedance spectrum, and capacitances and resistances of the sample connected in series. The part describing the electric behavior of the sample consists of the $C_1$, which corresponds to the bulk matrix, the resistance $R_1$ for crossing (capillary) pores filled with an electrolyte solution and $R_{op}$, $C_{op}$ describing the movement of ions in closed (occluded) pores. The Covelo model is designed for an experiment with electrodes attached to the sample in a testing cell. In the case with embedded electrodes, resistance $R_e$

is zero because the external solution does not appear in the system. If resistance $R_e$ is equal to zero, the Covelo model is the same as the EC model proposed by Song, which is more suitable for the embedded electrodes experiment.
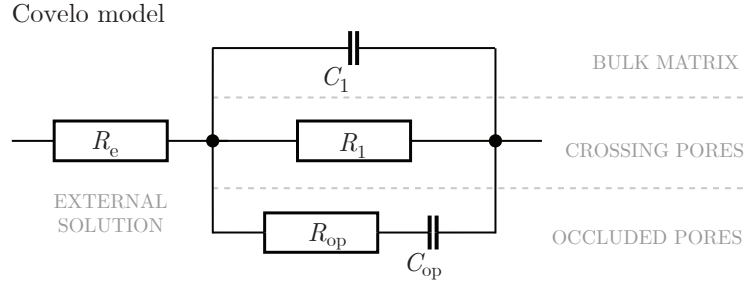


Figure 4.4: Equivalent circuit model proposed by Covelo [110].

**Equivalent circuit model proposed by Cruz**

The equivalent electric circuit model proposed by Cruz et al. [10] is based on the EC model. The Cruz model consists of sub-circuit modeling of the electrode-solution interface and a sub-circuit representing the sample. The first sub-circuit is composed of resistance $R_{sol}$ of the pore solution and the constant phase element $C_{ele}$, which is an imperfect capacitor describing the electric behavior of the embedded electrode in contact with the solution. The second sub-circuit is described by $R_1$, which is the resistance of connected capillary pores (and/or gel pores), $CPE_1$, which is a double layer capacitance of C-S-H gel, and resistance $R_{op}$ with the constant phase element $CPE_{op}$ corresponding to the resistance and diffusion of ions in the nano-pores (this branch overlaps with $CPE_{op}$).
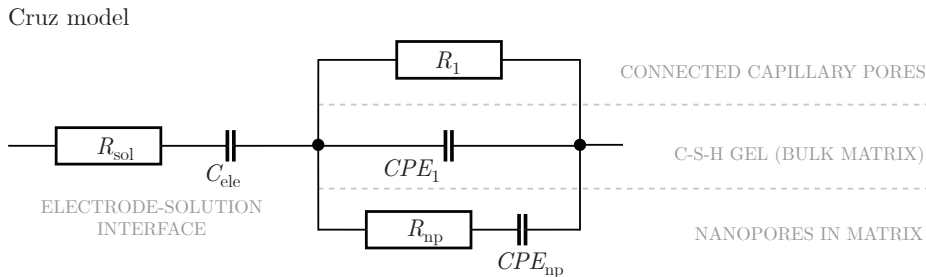


Figure 4.5: Equivalent circuit model proposed by Cruz [10].

**Fitting of the measured data**

Measured data are interleaved with a fit curve based on EC, SEC, Cabeza, Covelo, and Cruz models. The usability of the measured data is verified by Kramers-Kroning [111] fit and its fractional residual error. Fits based on the models mentioned above to evaluate resistances and capacitances are performed by the Simplex method. The goodness of fit $\chi^2$ is calculated

by using the equations contained in the software:

$$\chi^2 = \Sigma_{i=1}^{N} \cdot w_i^2 \cdot [(Z_{meas,re} - Z_{fit,re})^2 + (Z_{meas,im} - Z_{fit,im})^2], \tag{4.7}$$

where,

$$w_i = \frac{1}{\sqrt{(Z_{i,meas,re}^2 + Z_{i,meas,im}^2)}}, \tag{4.8}$$

where $Z_{meas,re}$ and $Z_{meas,im}$ are impedances of the measured data on the real and imaginary part of the Nyquist spectrum, respectively. $Z_{fit,re}$ and $Z_{fit,im}$ are the values of the fit on the real and imaginary parts of the Nyquist spectrum.

## 4.2 Porosity calculation from EIS measurements

### 4.2.1 Archie's law and its modifications

Archie's law is the most widely used relationship between resistivity and porosity of porous material. The relationship was originally derived from the sandstone filled with brine [16] and is defined by the equation:

$$F = A \cdot \phi_0^{-m}, \tag{4.9}$$

where $F$ is the formation factor (described below), $A$ is a coefficient, $\phi_0$ is capillary porosity, and $m$ is Archie's index. Archie's law can also be used for simply evaluation of CBMs porosity, but the following aspects need to be considered [17]:

1. The evolution of model parameter $m$ is not considered over time. The value of $m$ significantly affects the porosity as shown in Equation 4.9. The Archie index depends on the pore structure and differs with the age of the materials. Therefore, considering the constant $m$ is inappropriate.

2. The saturation degree is not considered. The transport of ions through the fluid cause the conductivity of the porous material. The volume fraction of the fluid is the porosity of saturated CBMs. For unsaturated CBMs, however, the porosity and degree of hydration are included in the fluid volume fraction. Therefore, Archie's law is applied to saturated CBMs.

3. The conductivity of the solid phase is not considered. Both capillary and gel pores are present in the cement paste. The conductivity of gel pores may be negligible in a highly porous cement paste. However, at low porosity, the conductivity of gel pores contributes significantly to the overall conductivity of the cement paste.

4. The percolation threshold is not considered because it is assumed zero in the capillary pores of the sandstone [112]. The percolation threshold of capillary pores in CBMs ranges from 0.16 to 0.20 [17, 113]. Thus the application of unmodified Archie's law is appropriate for very porous materials.

Some selected modifications of Archie's law used for the evaluation porosity of CBMs are described below. Further modifications are summarized in [17, 18].

**Effective electrical conductivity**

In cement-based materials, resistivity is dependent on sample dimensions and electrode positions. Thus, it is more convenient to convert the resistance to effective electrical conductivity $\sigma_{\text{eff}}$ as a function of electrode size and position:

$$\sigma_{\text{eff}} = \frac{l}{R \cdot S}, \tag{4.10}$$

where $l$ is the distance between the electrodes in the direction of current, $S$ is the cross-sectional area of the electrode embedded in the cement paste.

Therefore, the expression involving the effect of the saturation degree in Equation 4.9 is rewritten to:

$$\sigma_{\text{eff}} = C \cdot \sigma_0 \cdot \phi_0{}^m, \tag{4.11}$$

where $\sigma_0$ is the conductivity of conducting medium, $C$ is a constant depending on the saturation of the sample (assumed to be 1.0 for fully saturated samples), $\phi_0$ is the pore volume fraction, and $m$ is Archie's index. Exponent $m$ reflects pore complexity and tortuosity and is found in the range 1.5 - 4.0 [7, 106].

**Modified Archie's index including the effect of conductivity of solid phase**

CBMs consists of two phases - pore phase (with volume fraction $\phi_p$ and conductivity $\sigma_p$) and solid phase (with volume fraction $\phi_s$ and conductivity $\sigma_s$). Thus, the total volume of the material is:

$$\phi_p + \phi_s = 1. \tag{4.12}$$

The modification of Archie's law can given as:

$$\sigma_{\text{eff}} = \sigma_p \cdot \phi_p^m + \sigma_s \cdot \phi_s^{m^1}, \tag{4.13}$$

where the exponent $m^1$ is a parameter dependent on the degree of solid phase connectivity (better connectivity with the lower value), for cementitious materials with fluid-filled pores, the parameter $m^1$ takes very low values in the range of 0.03 - 0.10, resulting in a value of $\phi_s{}^{m^1}$ close to 1 [81]. In addition, capillary pores are the largest volume of the pores. Therefore volume fraction of pore phase $\phi_p$ is considered equal to capillary porosity $\phi_0$, which corresponds to the equality of the conductivities $\sigma_p = \sigma_0$. As a consequence, the modified Archie's law can be simplified to:

$$\sigma_{\text{eff}} = \sigma_0 \cdot \phi_0^m + \sigma_s, \tag{4.14}$$

where $\sigma_s$ is taken as 0.01 S/m [106] for CBMs without sand.

**Modified Archie's index including the effect of percolation threshold**

Percolation threshold $\phi_c$ of capillary pores is the critical porosity for the fluid movement in the material, and its value was predicted for cementitious materials. Percolation threshold and capillary porosity $\phi_0$ enter the following equation:

$$F = \left(\frac{\phi_0 - \phi_c}{1 - \phi_c}\right)^{-m}, \tag{4.15}$$

where $F$ is the formation factor and m is Archie's index. Formation factor is a commonly used parameter in conductive models of CBMs and is written in the following equation:

$$F = \frac{\sigma_0}{\sigma} = \frac{\zeta}{\zeta_0}, \tag{4.16}$$

where $\sigma$ and $\zeta$ represent total conductivity and resistivity of CBMs, $\sigma_0$ and $\zeta_0$ represent the pore solution conductivity and resistivity respectively [17, 114].

## 4.2.2 General effective media model

The general effective media (GEM) model proposed by McLachlan et al. [19] successfully describes the relation between electrical conductivity and porosity of a porous material. GEM model is not eliminated by any percolation threshold and predicts that cement paste consists of two phases [115]. The first phase with low conductivity is a solid matrix material and the second phase with high conductivity is capillary pores. GEM model is derived from Equations [17]:

$$\phi_0 \cdot \frac{\zeta_0^{1/k} - \zeta^{1/k}}{\left(\frac{1 - \phi_c}{\phi_c}\right) \cdot \zeta_0^{1/k} + \zeta^{1/k}} + (1 - \phi_0) \cdot \frac{\zeta_1^{1/k} - \zeta^{1/k}}{\left(\frac{1 - \phi_c}{\phi_c}\right) \cdot \zeta_1^{1/k} + \zeta^{1/k}} = 0, \tag{4.17}$$

$$\phi_0 = [(1 - \phi_c) \cdot F^{-1/k} + \phi_c] \cdot \left(\frac{M^{1/k} - F^{1/k}}{M^{1/k} - 1}\right), \tag{4.18}$$

where $\phi_0$ is capillary porosity, $\phi_c$ is the percolation threshold of capillary pores, $\zeta$ is total resistivity of CBMs, $\zeta_0$ is resistivity of pores solution, $\zeta_1$ is resistivity of solid phase and formation factor $F$ can be calculated using the Equation (4.16). Parameter $k$ is related to the shape of pore structures and takes values ranging from 1.40 to 2.46 [17] for composites. Parameter $M$ is given by equation:

$$M = \frac{\zeta_1}{\zeta_0}. \tag{4.19}$$

The application of the GEM model is impeded by the determination of parameters $k$ and $M$, which should not be considered constant due to their dependence on the degree of hydration. Both the tortuosity of pore structures and $k$ increase with hydration. In contrast, $M$ decreases with the growth of the C-S-H gel and can therefore be considered constant at the same degree of hydration. In addition, the parameter $M$ is also affected by temperature [17].

# 5 Experimental part

## 5.1 Experimental plan

Samples of pure cement paste, mortar, and cement paste modified by nanoparticles were produced for porosity estimation by electrochemical impedance spectroscopy. The results were supported by SEM + IA, gravimetric method, mercury intrusion porosimetry, and helium pycnometry. Nano-silica and nano-alumina were chosen for cement paste modification because they affect the porosity (and mechanical properties) of CBMs - nano-silica is assumed to decrease the porosity, and nano-alumina is assumed to increase the porosity of a cement paste. In addition, nano-silica and nano-alumina are relatively inexpensive and available compared with the other nanoparticles that can be added to cement paste. Totally, five types of mixtures were produced.

Pure cement paste (C) was produced as a reference to the modified mixtures. The optimal dosage of nano-silica is up to 4 % [116] of the cement weight, but at higher amounts, the particles may agglomerate and thus reduce the compressive and tensile strength. Therefore, the cement was replaced with 1.25% of nano-$SiO_2$ (CS-I) and 2.5% of nano-$SiO_2$ (CS-II) - such dosage reduces the porosity, and the nanoparticles are evenly distributed. In [117], Nazari et al. found that the highest compressive strength of cement modified with nano-$Al_2O_3$ is exhibited by its 1.5% replacement. Therefore, the CA mixture was produced in this modification. Cement mortar (M) with aggregates was also produced because its properties more closely match those of real concrete structures.

Table 5.1: Summary of the methods performed for porosity determination and chloride penetration tested at different sample age.

| sample age | EIS | MIP | helium pycnometry | †SEM + IA | gravimetric method | Cl$^-$ |
|---|---|---|---|---|---|---|
| 1 day | ✓ | | ✓ | | ✓ | |
| 3 days | ✓ | | ✓ | | ✓ | |
| 7 days | ✓ | ✓ | ✓ | ✓ | ✓ | ✓ |
| 14 days | ✓ | | ✓ | ✓ | ✓ | |
| 28 days | ✓ | ✓ | ✓ | ✓ ‡ | ✓ | ✓ |
| 56 days | ✓ | | ✓ | ✓ | ✓ | |
| 84 days | ✓ | | ✓ | ✓ | ✓ | |

Legend: † SEM with subsequent image analysis was not performed for mixture M.
‡ Energy dispersive spectroscopy analysis was performed.

The chloride penetration test was performed as a supplementary test to the porosity measurements in order to predict the effect of nano-additives on real structures.

The main method - electrochemical impedance spectroscopy - was performed on all types of mixtures at ages 1, 3, 7, 14, 28, 56, and 84 days as shown in Table 5.1. At the early

age of hydration, more time points of measurement were chosen because there are more noticeable changes in the microstructure and macroscopic properties than in the changes observed in mature cement paste. Helium pycnometry and gravimetric methods were also performed at all observed times for all five mixtures due to the simplicity and speed of the methods. SEM with subsequent image analysis was performed for C, CS-I, CS-II, and CA. The mortar samples were not polished due to the very different elastic modulus of the cement paste and aggregate particles. The early age samples of 1 and 3 days are in the phase of developing microstructure. Polishing samples with the current procedure would affect the image analysis results by highly overestimating the porous phase volume fraction. Due to the complexity of the measurements, the samples were used for mercury intrusion porosimetry and chloride penetration test only at 7 and 28 days of age. Since MIP and chloride penetration tests are complementary experiments and are not required for EIS measurements, additional observation times would not be chosen even if these experiments were not time-consuming.

## 5.2 Optimization of EIS measurement

Before the application of EIS to the samples used in this thesis, it was necessary to optimize the method and the dimensions of the samples and electrodes. The test samples were made from the CEM I 42.5R with a w/b ratio of 0.4, and measurements were performed at 14 days of sample age.

### 5.2.1 Type of electrodes

The type of used electrodes has a significant effect on the measured impedance by EIS. Three types of electrodes were tested. The first type was a full stainless steel plate (FP - Figure 5.1a) of thickness 0.5 mm and was inserted 3 mm above the formwork bottom to the cement paste interlinking. The second type was a perforated plate (PP - Figure 5.1b) from the same plate as the first type with 8 drilled holes of diameter 1.5 mm. A perforated plate was inserted to the full height of the sample, and the cement paste was linked through the holes. The third type of electrodes was made from the stainless steel grid (G - Figure 5.1c) made of 0.5 mm diameter wire with 1.8 mm mesh.
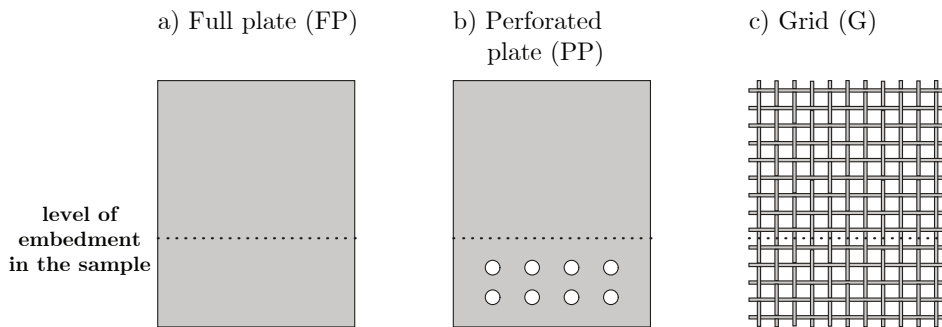


Figure 5.1: The types of electrodes: a) full plate, b) perforated plate, c) grid.

It was found that the interlinking of the cement paste of the sample with the PP electrode was insufficient. Also, drilling holes in the plate was time demanding. The area of the embedded electrode of type G in the cement paste was more challenging to determine and may have been inaccurate due to its unequal and ambiguous surface. All types of electrodes mentioned above (FP, PP, G) are applicable for EIS measurements. However, the FP electrode was chosen for the EIS measurements in this thesis. Since the inserted area of the electrode is easy to calculate, the interlinking of the cement paste is secured by the 3 mm offset from the sample surfaces, and the path leading to the electric current is clear.

### 5.2.2 Dimensions of samples and electrodes

The impedance measurement is also affected by the size and location of the electrode in the sample. This is determined by the ratio $S/d$, where ($S$) is the area of electrode contact with the material and ($d$) is a distance between the electrodes in the direction of the current. The wrong assumption of the $S/d$ ratio might significantly affect the results. Bayer [82] worked with the samples of 3 mixtures of CBMs, a $S/d$ ratio of 157. In contrast, Danoglidis et al. [11] used carbon nanotubes (CNT) cement paste samples with $S/d$ ratio of 6.6 for EIS measurements. A smaller ratio of $S/d$ can be used for CNT reinforced cement paste because the CNTs in the cement paste form a continuous electrically conductive network. Thus, the resistance of this sample is lower than that of a pure cement paste sample.

Contact between the electrode and the material can be achieved in two ways. The first is embedding the electrodes in the material. The second way is by attaching the electrodes to the material. In order to improve the measurement condition, a conductive material (e.g. graphite felt) should be inserted between the material and the electrodes to ensure a conductive and flexible bond between them. The sample should also be placed in a cell to ensure a stable condition during the measurement [82]. In this thesis, embedded electrodes were used.
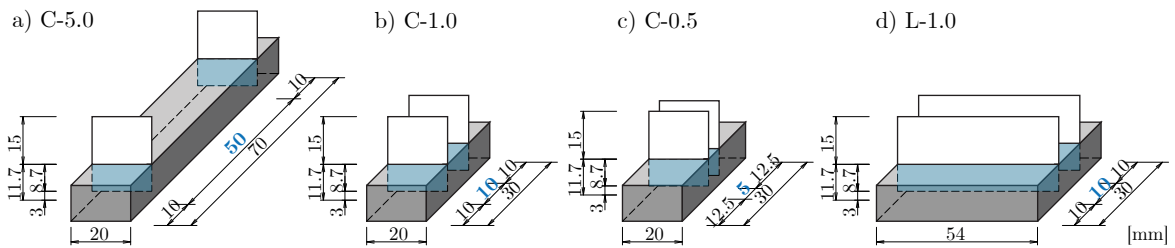


Figure 5.2: Illustration of the samples with different dimensions and distances between the electrodes.

Firstly, the samples were made for the electrode type test with dimensions of 70 × 20 × 11.7 mm (length, width, height) and crosswise electrodes were spaced 50 mm apart (C-5.0) - $S/d$ ratio was 3.2 inspired by Danoglidis study [11]. Measurements of this sample did not yield adequate results, e.g. too high resistance was measured, the Nyquist spectrum was not smooth. Therefore no evaluation could be performed since the equivalent electric circuit was changed compared to the samples containing CNT. Consequently, three types of samples with

different $S/d$ ratios were made to yield adequate results. Two samples with dimensions of $30 \times 20 \times 11.7$ mm (length, width, height) had electrodes inserted crosswise with distances between them of 10 mm (C-1.0) and 5 mm (C-0.5). The third sample with dimensions 54 $\times$ 30 $\times$ 11.7 mm (length, width, height) was made with a distance of 10 mm between the electrodes inserted lengthwise (L-1.0). The offset of the electrodes from the bottom of the formwork was 3 mm for all the samples, and the electrodes were inserted across the entire width of the sample. The ratio of $S/d$ is 17, 35, and 47, respectively, as shown in Table 5.2.

Table 5.2: Dimensions of test samples and electrodes.

| label | length | width | height | $S$ | $d$ | $S/d$ |
|-------|--------|-------|--------|-----------|--------|--------|
|       | (mm)   | (mm)  | (mm)   | (mm$^2$)  | (mm)   | (mm)   |
| C-5.0 | 70     | 20    | 11.7   | 174       | 50     | 3      |
| C-1.0 | 30     | 20    | 11.7   | 174       | 10     | 17     |
| C-0.5 | 30     | 20    | 11.7   | 174       | 5      | 35     |
| L-1.0 | 54     | 30    | 11.7   | 470       | 10     | 47     |

The sample L-1.0 has the largest $S/d$ ratio and thus seems to be the most appropriate. However, sample C-0.5 with a smaller ratio of $S/d$ had comparable results. Therefore, samples with both geometries could be used for future measurements, as a $S/d$ ratio of around 40 was sufficient. In the main part of the thesis, the L-1.0 sample geometry was used.

### 5.2.3 Influence of ambient solution

Samples hydrate in limewater, but measurements are made at a lower relative humidity of $\approx$ 40 - 60 %. After the removal of the samples from the water, the sample begins to dry out, which affects the measured resistivity (the resistivity increases as the drying process continues). The drying process should be prevented, for example, by partially immersing the sample in the solution to avoid contact water with the electrode.
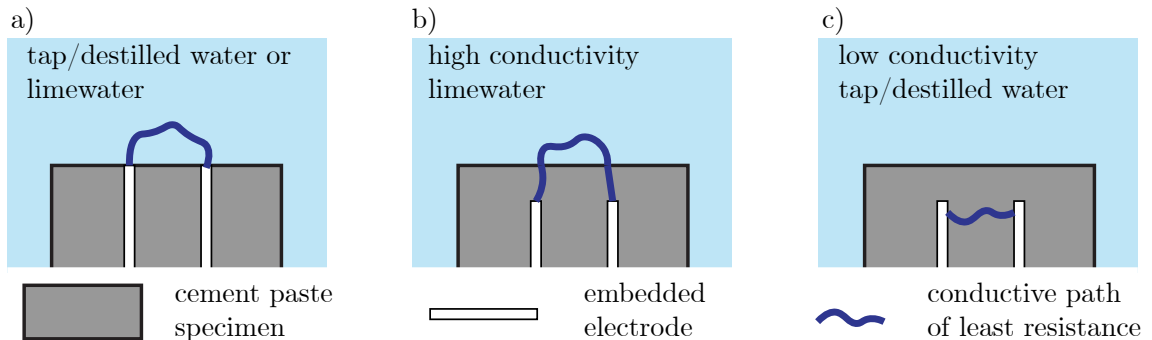


Figure 5.3: Assumed conductive paths of the electric current depending on position of electrodes - differences between a) and b). Conductive paths also depend on the conductivity of the immersion solution - differences between b) and c).

The assumed conductive path of electric current passes between the embedded electrodes, especially through the cement paste. However, when the embedded electrode was placed across the entire width of the sample and immersed in the solution, the electric current could pass through different conductive paths of least resistance (e.g. from the embedded electrode to the solution and back), as shown in Figure 5.3a. The electrodes should therefore be embedded in the sample with a sufficient covering layer of cement paste (the samples used in this thesis were protected on all sides by 3 mm thick covering layer). Only a partial immersion of the sample in the solution is necessary to avoid contact between the solution and the electrodes on the top of the sample, as shown in Figure 5.4.
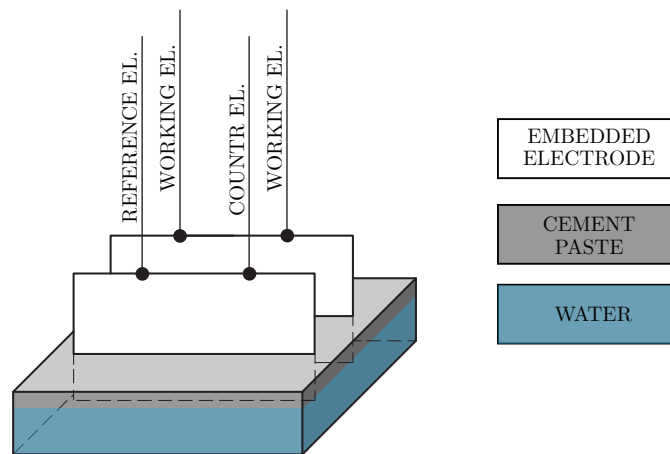


Figure 5.4: Illustration of a partially submerged sample in water during EIS measurement.

The conductivity of the solution in which the samples are immersed during the measurement greatly influences the measured resistance. Three types of solutions were tested: tap water, destilled water and limewater, where the samples were stored. Every sample was measured 5 times with $\approx$ 5 min intervals. The whole process took about 30 min. The conductive path is assumed to be affected by the high conductivity of limewater (1030 mS/m), as shown in Figure 5.3b, which is several times higher than the conductivity of tap water (average 30 mS/m [118]) and destilled water (around 0.15 mS/m [119]). The resistivities of tap and destilled water were stable and almost identical, as shown in Table 5.3. The resistivity measured in limewater was about 20 - 25 % lower than resistivities of tap and destilled water because the electric current passes through a highly conductive solution as shown in Figure 5.3b. The resistivity increases with increasing immersion time in the limewater solution. It is probably that although the surface water was removed from the top of the sample, a small amount of limewater remained. Therefore, electric current can pass through this surface water and the measured resistivities are lower compared to tap and destilled water. The increase in resistance over time could be due to the gradual drying of the sample. Therefore, the tap water and destilled water can be used as an immersion solution for EIS measurements as shown in Figure 5.3c.

Table 5.3: Resistances of samples measured by EIS in different immersion solution.

| solution | resistance ($\Omega$) |
|---|---|
| destilled water | $233 \pm 1.1$ |
| tap water | $230 \pm 0.5$ |
| limewater | $174 \pm 1.2 \rightarrow 182 \pm 0.2$ † |

Legend: † Resistivity increased over the 30-minute measurement interval.

### 5.2.4 Influence of relative humidity

The vast majority of structures are not located in an environment with 100 % relative humidity (RH). The average relative humidity is about 40 - 70 %. Therefore, the samples originally intended for optimization of measurements were stored at different relative humidities for 1 month until weight stabilization was observed. Subsequently, EIS measurements were performed at this time and after 2 months of storage at different RH. The different relative humidities were provided by saturated salt solutions and silica gel, summarized in Table 5.4. Before that, reference measurements were performed on the 4 and 6 month old fully saturated samples that were not immersed in the water during the measurements because some of the used (test) samples had electrodes located at the edge, as shown in Figure 5.3a. Subsequently, some of the saturated samples were stored at 43 %, 76 %, and 98 % relative humidities. Samples for the storage at 11 % RH were dried at 50°C for 14 days in order to reach the steady state more quickly and then placed in a box with silica gel. The reference sample was kept in the limewater.

Table 5.4: The relative humidity provided by saturated salt solutions.

| saturated salt solution | silica gel | relative humidity (%) |
|---|---|---|
| $KNO_3$ | | 98 |
| NaCl | | 76 |
| $K_2CO_3$ | | 43 |
| | silica gel | 11 |

## 5.3 Samples preparation

Five types of samples (C, CS-I, CS-II, CA, and M) were produced with a water to binder ratio of 0.4 and with a different mixture as shown in Table 5.5. The ordinary Portland cement, CEM I 42.5 R, was used from the Radotín cement plant, Českomoravský beton, a.s., and with a specific surface area 359 m$^2$/kg. Cement mineral composition is shown in Table 5.6. Cement paste was modified by colloidal nano-$SiO_2$ (50% solution of Levasil CB8, Nouryon) and nano-$Al_2O_3$ powder (with particle size 20 - 30 nm) with weight replacement of cement. The ratio of cement to aggregates was chosen to be 1:1 in the mortar mixture because of

the good workability of fresh concrete without the need for the addition of a plasticizer. The siliceous aggregates with fraction 0 - 0.5 mm were used because of the small dimensions of the samples and because a larger fraction caused worse immersion of the electrodes in the mixture.

Table 5.5: Types of sample mixtures.

| label | Additive | | cement | water | nano-SiO$_2$ | nano-Al$_2$O$_3$ | aggregate |
|---|---|---|---|---|---|---|---|
| | (%) | | (g) | (g) | (g) | (g) | (g) |
| C | | - | 1000 | 400 | 0 | 0 | 0 |
| CS-I | 1.25 | nano-SiO2 | 987.5 | 400 | 12.5 | 0 | 0 |
| CS-II | 2.5 | nano-SiO2 | 975 | 400 | 25 | 0 | 0 |
| CA | 1.5 | nano-Al2O3 | 985 | 400 | 0 | 15 | 0 |
| M | | siliceous aggregate | 1000 | 400 | 0 | 0 | 1000 |

Table 5.6: Mineral composition of CEM I 42.5 R, X-ray fluorescence data provided from the manufacturer.

| | SiO$_2$ | Al$_2$O$_3$ | Fe$_2$O$_3$ | CaO | MgO | SO$_3$ | K$_2$O | Na$_2$O | Cl$^-$ |
|---|---|---|---|---|---|---|---|---|---|
| | (%) | (%) | (%) | (%) | (%) | (%) | (%) | (%) | (%) |
| CEM I 42.5 R | 19.66 | 4.35 | 2.44 | 66.24 | 2.07 | 3.08 | 0.73 | 0.11 | 0.09 |

Two types of samples were made - samples with electrodes inserted for EIS measurement (in this thesis, one sample with electrodes was used for measurements at all observed times) and samples without electrodes, which were used for all other measurements (one sample was produced for each observed time, which was then cut at the desired time as described below).

The first type used for EIS measurement was a block with dimensions of 54 × 30 × 11.7 mm (length, width, height). Additionally, a pair of electrodes from a stainless steel plate was put longitudinally into the formwork. Electrodes were inserted 3 mm above the formwork bottom and 3 mm from the formwork edges. The distance between the electrodes was set to 10 mm. The scheme of the sample geometry for EIS measurement is shown in Figure 5.5. Three samples of the first type were produced for each mixture.
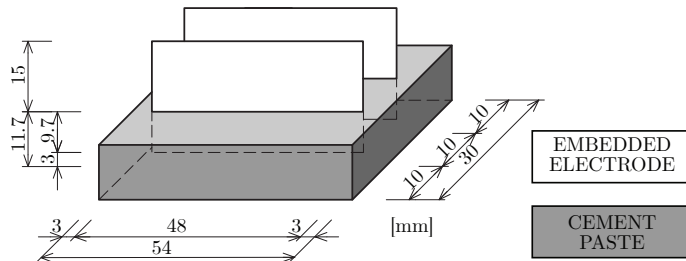


Figure 5.5: An illustration of the sample with embedded electrodes.

The second type with a cylindrical shape with a diameter of 27 mm and height of 64 mm was prepared for porosity measurement using other methods. Both types of samples were removed from the formwork after 24 hours and placed in 0.5% limewater solution where retained until the measurement.

Cylindrical shape samples were sliced by a precise diamond saw at the required times (1, 3, 7, 14, 28, 56, and 84 days). All slices were used for measurement by gravimetric method, and other methods were done on the slices of various thicknesses. The slices were cut into three thicknesses - 6 pieces of 2 mm, 3 pieces of 7 mm and one slice with a thickness of approximately 13 mm. The slices of 2 mm thick were used only to the gravimetric method. The small thickness accelerates the drying process. Two 7 mm and 13 mm thick slices were used for helium pycnometry measurement. Further, one of the slices was used for SEM with IA - the sample polisher requires samples with a minimum thickness of 7 mm. Another cylindrical shape sample was cut at 7 and 28 days of age into 3 pieces of 3 mm and 1 piece of 15 mm, which was used for MIP. The 3 mm thick slices were placed in 0.5% sodium chloride solution for 40 hours. This time was predicted by the Fick law to allow the chloride to penetrate the entire slice thickness. The chloride surface concentration was assumed as 6 g/kg, and the diffusion coefficient $D_{eff}$ was assumed as $11 \cdot 10^{-12}$ m$^2$/s [120]. Subsequently, all the cut samples were dried in an oven at 50°C.

## 5.4 Experimental setup

### 5.4.1 Scanning electron microscopy and image analyses

The dried samples were ground and polished in a scanning electron microscope before observation. Series of 500, 1200, 2000, and 4000 grit silicone carbide papers were used for lubricant-free grinding, each lasting approximately 2.5 min. Polishing was performed on a soft cloth with a diamond spray containing dispersed particles of size 0.25 µm. Also, the samples were immersed in alcohol and an ultrasonic cleaner after each step to remove free particles.

A Phenom XL desktop scanning electron microscope was used to characterize the phase composition of the C, CS-I, CS-II, and CA mixtures and the volume of each phase. The image maps were at the time of 7, 14, 28, 56, and 84 days in BSE mode (at 15 kV, 1000× magnification, spot size 300 µm) covering an area of 1.65 mm$^2$. This area size should be sufficiently representative for the studied microstructures [121]. Moreover, energy dispersive X-ray spectroscopy was performed for one selected spot of cement paste mixture for chemical characterization at 28 days of age (at 15 kV, 3500× magnification, spot size 80 µm, map resolution 1024×1024, pixel time 4 ms).

### 5.4.2 Gravimetric method

The open porosity of all samples (C, CS-I, CS-II, CA, and M) was measured by gravimetric method at all observation times. Firstly, the fully saturated sample slices (10 slices per

sample) were weighed in water at atmospheric pressure to obtain Archimedes weight $m_a$. Then, the water was removed from the surface slices, then weight $m_w$ was measured, and the volume of samples was calculated. Subsequently, the slices were placed in an oven and dried at 50°C until the weight was stabilized. The stabilization period of 2 mm slices took $\approx$ 3 days, for 7 mm slices about 10 days. Dried samples were also weighed ($m_d$) and the bulk density $\rho_{g,grav}$ and open porosity $\phi_{0,grav}$ of the samples were evaluated.

### 5.4.3 Mercury intrusion porosimetry

MIP also characterized the pore structure of all produced mixtures at a hydration age of 7 and 28 days. The measurements were done on approximately 5 g fragments of dried samples using set of instruments PASCAL 140 + 440 made by Thermo Fisher Scientific Inc. From this method, the pore size was calculated based on the external pressure required for mercury intrusion into the pores using the Washburn equation. The cumulative pore distribution curve was obtained for pore radii from 3 nm to 100 µm, and the mercury contact angle was considered to be 130°.

### 5.4.4 Helium pycnometry

The porosity of samples was also measured on dried samples by helium pycnometer Pycnomatic ATC from Thermo Fisher Scientific. The matrix density of all five mixtures was measured by a change of pressure in the device chamber on three samples at 7 observation times. The total open porosity $\phi_{0,pyc}$ of the studied material was calculated based on the bulk density measured by the gravimetric method and the matrix density.

### 5.4.5 Chloride penetration test

Samples C, CS-II, CA, and M were used for chloride penetration tests at 7 and 28 days of age. The samples were placed in 3 % NaCl solution. Three 3 mm thick slices from each mixture were immersed in 10 l of salt water to ensure a stable NaCl concentration during chloride penetration and binding to the pore walls. The exposure time was estimated to be 40 hours. This time was assumed to be sufficient to allow chloride penetration into the entire volume of the samples exposed to the solution from both sides. After 40 hours, the samples were dried in an oven at 50°C until their weight had stabilized.

The same procedure as in Bayer's thesis [82] was used to obtain the total chloride volume. The dried samples were ground to powder. A quantity of $\approx$ 2.5 g of powder was weighed accurately and placed in a beaker with 50 ml of demineralized water and 10 ml of 5 mol/l nitric acid. Subsequently, 50 ml of boiled demineralized water was added and covered with a watch glass. The suspension was boiled for 3 min. Then, the suspension cooled to room temperature and was filtered through filter paper. Potentiometric titration was then performed on an EasyPlus APO 15 device from Mettler Toledo using 0.1 M AgNO$_3$ solution. The concentration in the sample $C_{cl}$ was then calculated from the known total volume of the solution $V_{tot}$, the weight of the original powder $m_s$, and the chloride concentration in the solution $C_{titr}$.

### 5.4.6 Electrochemical impedance spectroscopy

EIS measurement was performed using Zahner Zennium X device and ThalesXT USB software with a frequency range of 12 MHz - 100 Hz and 10 steps per decade. The amplitude of the sinusoidal voltage was set to 10 mV. The use of a larger potential amplitude is not recommended due to possible changes in the surfaces of the samples [102]. The cables connected two working electrodes to one of the embedded electrodes. The reference electrode and the counter electrode were connected to the other of the embedded electrode as shown in Figure 5.5 [122]. Short coaxial cables were used to reduce the influence of surrounding phenomena and a measurement noise [102]. Samples were partly submerged in the tap water while simultaneously avoiding contact between electrodes and water as described in Subsection 5.2.3. The samples were measured at 7 different ages of hydration - 1, 3, 7, 14, 28, 56, and 84 days. The EIS measurements were performed three times on the individual samples, for a total of 9 measurements were taken for each mixture at one observation time. Totally, 315 measurements were performed during the whole observation period.

# 6 Results

## 6.1 Scanning electron microscopy and image analyses

Samples at 28 days aged were used for EDS analysis to obtain the chemical composition of the mixtures. The performed maps are shown in Figure 6.1. The percentage representation of oxides ($CaO$, $SiO_2$, $Al_2O_3$, $MgO$, $SO_3$, $Fe_2O_3$, and $K_2O$) is summarized in Table 6.1. As visible, the differences between individual mixtures are minor since the same type of Portland cement was used for mixtures. The small amount of NPs addition (1.25 % - 2.5%) did not affect the chemical composition of the mixtures very much.
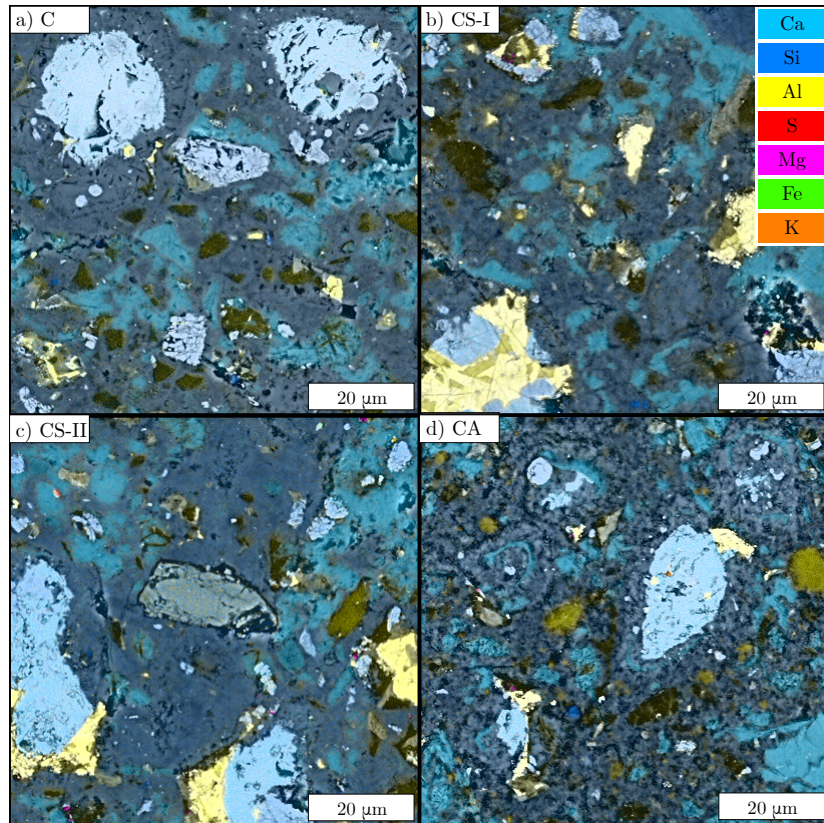


Figure 6.1: EDS maps performed for 28 days old samples: a) C, b) CS-I, c) CS-II, d) CA.

Image analysis was performed for C, CS-I, CS-II, and CA using color pixel thresholding. Sample older than 7 days were used for image analysis. Color pixel thresholding was used to segment the images into individual components. In general, the sample's microstructure was divided into main hydrates, unhydrated clinker particles, CH, and pores/cracks. The volume fraction of individual components of the mixtures during the time is summarized in Table 6.2. The volume fraction was obtained from a single image map covering a suffi-ciently representative area of each mixture. Some phases were not clearly separated due to similar color intensity. Therefore, phases e.g. C-S-H gel, C-A-H gel, and C-A-S-H gel were jointly identified as main hydrates. The group of pores contains shrinkage cracks or cracks artificially created during polishing. Also, the color intensity overlaps with other phases,

Table 6.1: Stoichiometric weigh concentration of oxides measured by EDS analysis for 28 days old samples.

| mixture | stoichiometric weight concentration (%) | | | | | | |
|---|---|---|---|---|---|---|---|
| | CaO | $SiO_2$ | $Al_2O_3$ | MgO | $SO_3$ | $Fe_2O_3$ | $K_2O$ |
| C | 64.0 ± 0.4 | 23.5 ± 0.3 | 4.6 ± 0.3 | 1.8 ± 0.1 | 3.6 ± 0.1 | 2.6 ± 0.3 | 0.2 ± 0.0 |
| CS-I | 63.9 ± 1.0 | 22.2 ± 1.5 | 5.3 ± 1.1 | 1.8 ± 0.1 | 3.5 ± 0.2 | 3.1 ± 0.7 | 0.2 ± 0.0 |
| CS-II | 61.3 ± 0.6 | 24.0 ± 0.7 | 5.1 ± 0.3 | 2.3 ± 0.3 | 3.5 ± 0.2 | 3.0 ± 0.3 | 0.7 ± 0.0 |
| CA | 63.0 ± 1.1 | 22.6 ± 1.6 | 6.4 ± 0.6 | 1.7 ± 0.0 | 3.9 ± 0.4 | 2.9 ± 0.5 | 0.5 ± 0.1 |

causing an overestimation or underestimation of the phases, so this method is approximate and dependent on the accuracy of the estimation. The example of SEM-BSE images and corresponding image analysis performed is shown for two selected hydration times (7 and 56 days) in Figure 6.2.

In general, the volume of pores and cracks decreases with increasing time due to continuous hydration and ranges from 12.9 % at 7 day of age samples to 7.1 % measured at 84 days. The volume of cracks and pores at age 1 day of hydration is similar for all mixtures and is ≈ 12.8 %. At further hydration ages, the crack/pores volumes of CS-I and CS-II take on lower values than those of pure cement paste in proportion to the amount of nano-silica added. These values are almost identical to the reference mixture at the 84 days with $\phi_0 \approx 7.3$ %. In contrast, CA has ≈ 1.5 % more volume of cracks/pores, which ranges from 12.8 % to 9.0 %.

Table 6.2: Volume fraction of individual microstructure components evaluated by image analysis from SEM-BSE images.

| mixture | cracks/pores (%) | | | | | main hydrates (%) | | | | |
|---|---|---|---|---|---|---|---|---|---|---|
| | 7 d. | 14 d. | 28 d. | 56 d. | 84 d. | 7 d. | 14 d. | 28 d. | 56 d. | 84 d. |
| C | 12.9 | 11.2 | 10.0 | 8.7 | 7.4 | 62.4 | 66.0 | 69.8 | 73.6 | 75.1 |
| CS-I | 13.0 | 10.3 | 8.3 | 8.0 | 7.4 | 63.0 | 68.7 | 72.7 | 73.9 | 76.1 |
| CS-II | 12.3 | 9.0 | 8.0 | 7.8 | 7.1 | 63.5 | 69.9 | 73.6 | 76.2 | 78.1 |
| CA | 12.8 | 11.3 | 10.5 | 9.4 | 9.0 | 62.7 | 66.9 | 68.9 | 72.7 | 73.3 |
| mixture | Portlandite (%) | | | | | unhydrated clinker particles (%) | | | | |
| | 7 d. | 14 d. | 28 d. | 56 d. | 84 d. | 7 d. | 14 d. | 28 d. | 56 d. | 84 d. |
| C | 12.8 | 11.3 | 10.5 | 10.4 | 10.3 | 12.0 | 11.4 | 9.8 | 7.4 | 7.1 |
| CS-I | 12.4 | 10.2 | 10.0 | 9.8 | 9.4 | 11.6 | 10.9 | 9.0 | 8.3 | 7.1 |
| CS-II | 12.3 | 10.1 | 9.4 | 8.1 | 7.8 | 12.0 | 11.0 | 9.1 | 7.9 | 7.1 |
| CA | 12.6 | 11.6 | 10.9 | 10.7 | 10.7 | 11.9 | 10.2 | 9.6 | 7.2 | 7.1 |

The volume of main hydrates generally increases with hydration time as new phases are formed at the expense of the volume of unhydrated clinker particles and Portlandite. The volume of unhydrated clinker particles is not affected by nano-additives and therefore has
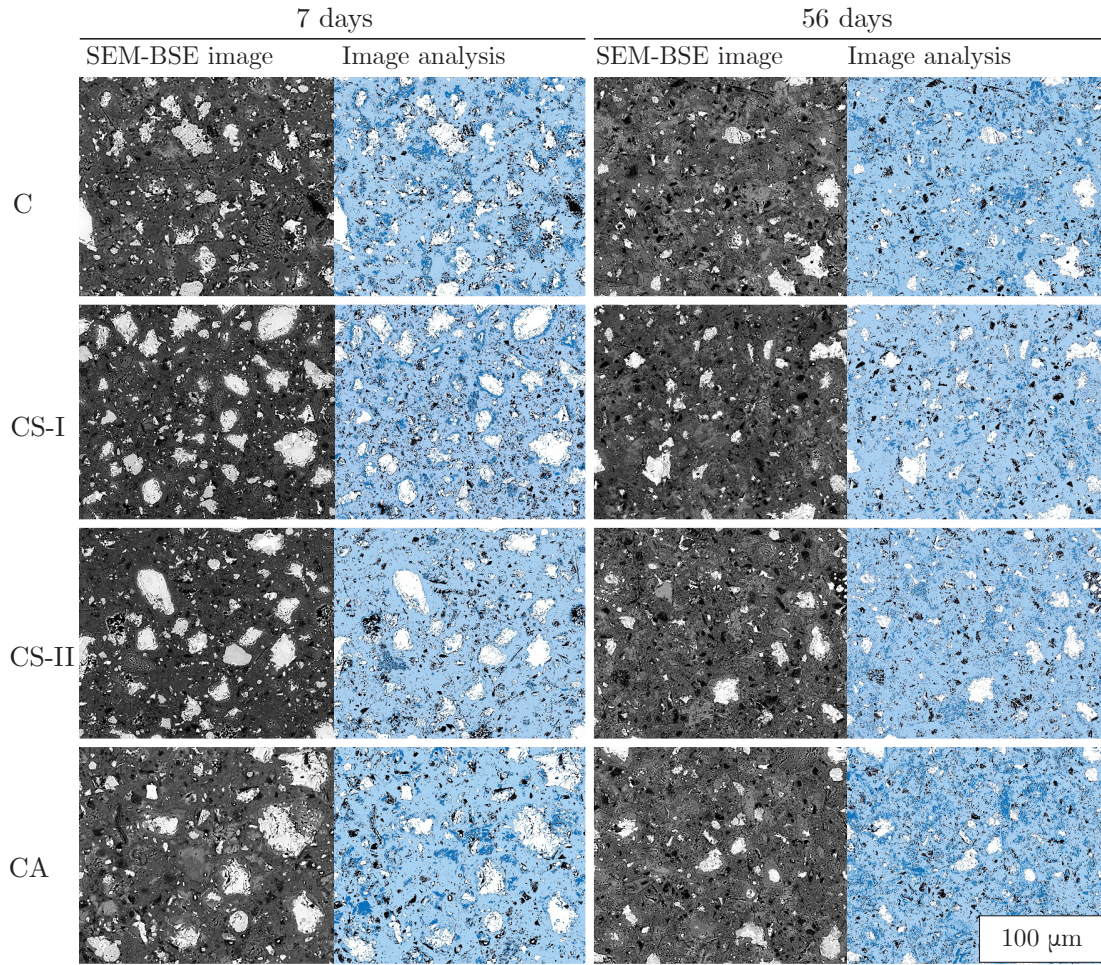
Figure 6.2: SEM-BSE images and image analysis of different mixtures at 7 and 56 days aged showing individual phases: pores/cracks (black), main hydrates (light blue), Portlandite (dark blue), unhydrated clinker particles (white).

approximately the same for all mixtures at the observed times. The volume of unhydrated clinker particles varies from $\approx 11.9$ % at 7 days old to $\approx 7.1$ %, which is the value measured for the 84 days old sample. The results show that the volume of Portlandite decreases with continuous hydration. The addition of nano-silica decreased the volume of CH because it formed an additional C-S-H gel. The reduction in the volume of Portlandite increases with the amount of nano-silica added. The initial CH volume is almost identical for all mixtures and is $\approx 12.5$ %. Based on mention above principle, the CH volume of CS-I and CS-II mixtures decreases by about $\approx 9$ % and $\approx 25$ %, respectively, compared to the C-84d sample.

In contrast, the addition of nano-aluminum increases the volume of formed Portlandite compared to the pure cement paste by $\approx 3$ % at the last measurement time. The volume of main hydrates in all mixtures is $\approx 63$ % at 7 days old. The volume gradually increases with time due to hydration. At 84 days, the highest volume of main hydrates has CS-II (78.1 %), followed by CS-I (76.1 %), which confirms the addition reaction of nano-silica. The volume fraction of the reference C mixture was measured as 75.1 %. The slowest increase of main hydrates was observed for the CA sample as 73.3 %.

## 6.2 Gravimetric method

A wide range of open porosity values measured by the gravimetric method lies in the interval from 19.4 % to 37.8 % as summarized in Table 6.3. The results are also graphically shown in Figure 6.3. The highest porosity was measured for 1 day old samples and gradually decreased with hydration time. This phenomenon corresponds to the formation of new hydration products which occupy the space initially occupied by water (esp. capillary pores). After 28 days, the porosity decreases from $\approx 37$ % to $\approx 30$ % for all cement paste samples. Furthermore, changes in open porosity were measured at less than 1 % for all mixtures. No apparent effect of nanoparticles was observable. The open porosity of mortar samples was measured significantly lower by up to 35 % compared to samples due to the presence of aggregates in the volume.
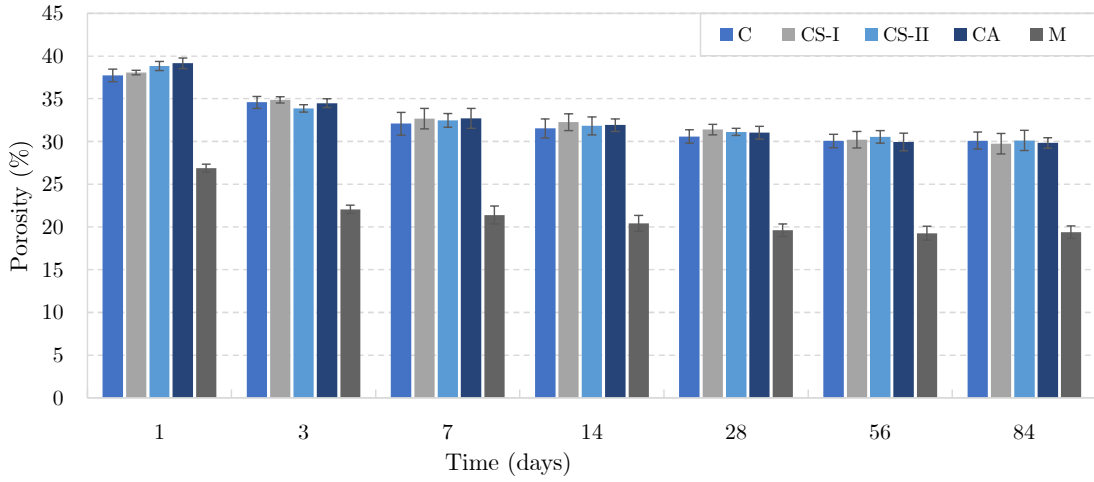


Figure 6.3: Porosity evaluated by gravimetric method.

Table 6.3: Total open porosity of different mixtures evaluated by gravimetric method.

| age | porosity (%) | | | | |
|---|---|---|---|---|---|
| (days) | C | CS-I | CS-II | CA | M |
| 1 | 37.8 ± 0.7 | 38.1 ± 0.3 | 38.8 ± 0.5 | 39.1 ± 0.6 | 26.9 ± 0.5 |
| 3 | 34.6 ± 0.7 | 34.9 ± 0.4 | 33.9 ± 0.4 | 34.5 ± 0.5 | 22.1 ± 0.5 |
| 7 | 32.1 ± 1.3 | 32.7 ± 1.2 | 32.5 ± 0.8 | 32.7 ± 1.2 | 21.4 ± 1.1 |
| 14 | 31.5 ± 1.1 | 32.3 ± 1.0 | 31.8 ± 1.1 | 31.9 ± 0.7 | 20.4 ± 0.9 |
| 28 | 30.6 ± 0.8 | 31.4 ± 0.6 | 31.3 ± 0.4 | 31.0 ± 0.8 | 19.6 ± 0.7 |
| 56 | 30.1 ± 0.8 | 30.2 ± 1.0 | 30.5 ± 0.7 | 29.9 ± 1.0 | 19.3 ± 0.8 |
| 84 | 30.1 ± 1.0 | 29.7 ± 1.2 | 30.1 ± 1.2 | 29.8 ± 0.6 | 19.4 ± 0.7 |

## 6.3 Helium pycnometry

The porosity obtained by helium pycnometry lies in the interval from 16.5 % to 34.0 % as shown in Table 6.4 and graphically in Figure 6.4. The highest porosity was measured for the 1 day old and gradually decreased with hydration time, similar to the measurement with the gravimetric method in Section 6.2. After 28 days, the porosity decreased from $\approx$ 38 % loss to $\approx$ 31 % compared to the first measurements. The differences between the modified cement pastes and the reference cement paste vary but do not have a typical trend. The maximum differences between the modified cement mixtures decrease from $\approx$ 10 % to $\approx$ 5 % with increasing hydration. The only stable phenomenon is the higher porosity of CS-I and CA mixtures compared to CS-II. Mortar is again characterized by significantly lower porosity of $\approx$ 30 % compared to cement pastes.
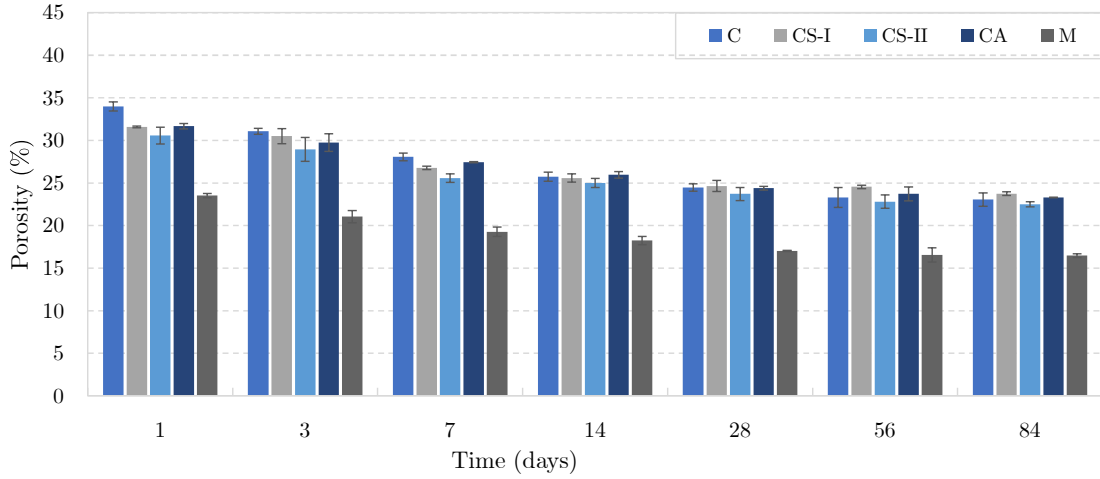


Figure 6.4: Porosity results measured by helium pycnometry.

Table 6.4: Total open porosity of different mixtures measured by helium pycnometry.

| age | porosity (%) | | | | |
|---|---|---|---|---|---|
| (days) | C | CS-I | CS-II | CA | M |
| 1 | 34.0 ± 0.5 | 31.6 ± 0.1 | 30.6 ± 1.0 | 31.7 ± 0.3 | 23.5 ± 0.2 |
| 3 | 31.1 ± 0.4 | 30.5 ± 0.9 | 28.9 ± 1.4 | 29.8 ± 1.0 | 21.0 ± 0.7 |
| 7 | 28.1 ± 0.5 | 26.8 ± 0.2 | 25.6 ± 0.5 | 27.4 ± 0.0 | 19.3 ± 0.6 |
| 14 | 25.7 ± 0.5 | 25.6 ± 0.5 | 25.0 ± 0.5 | 26.0 ± 0.4 | 18.2 ± 0.5 |
| 28 | 24.5 ± 0.4 | 24.6 ± 0.7 | 23.7 ± 0.8 | 24.4 ± 0.2 | 17.0 ± 0.1 |
| 56 | 23.3 ± 1.2 | 24.5 ± 0.2 | 22.8 ± 0.8 | 23.7 ± 0.8 | 16.6 ± 0.8 |
| 84 | 23.0 ± 0.8 | 23.7 ± 0.2 | 22.5 ± 0.3 | 23.3 ± 0.1 | 16.5 ± 0.2 |

## 6.4 Mercury intrusion porosimetry

The results of mercury intrusion porosimetry can be processed into the different outputs - cumulative pore volume curve, distribution pore volume curve and pore volume distributed by pore diameter into five groups according to the decade from 1 nm - 100 µm. The cumulative pore volume is shown in Figure 6.5. Mixture C acquires the largest values of total cumulative volume, 0.157 cm$^3$/g and 0.135 cm$^3$/g, at both 7 and 28 days, respectively. In contrast, the mortar has the smallest total cumulative pore volume. M-7d has reduced values by $\approx$ 50 % compared to C-7d, and the total cumulative pore volume of M-28d has reduced by $\approx$ 38 % compared to C-28d. The modified cement pastes assume nearly the same values at 7 days, differing by $\approx$ 2 %. However, CS-II-28d achieves $\approx$ 20 % higher values than the CS-I and CA mixtures at 28 days.
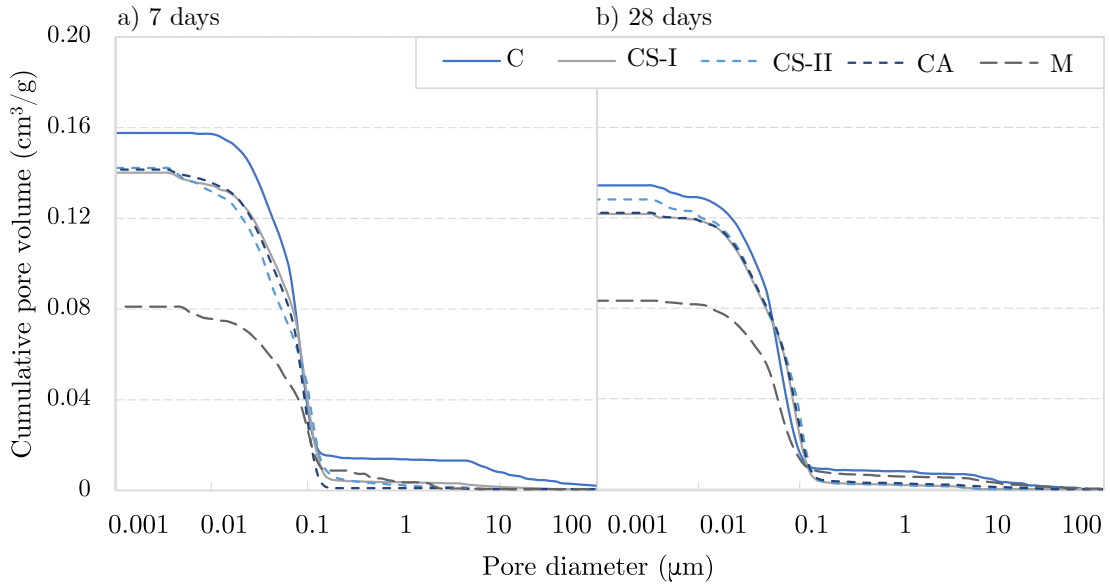


Figure 6.5: Cumulative pore volume curves of different cement pastes measured a) at 7 days and b) at 28 days of hydration.

The pore size distribution curves in the material are shown more clearly in Figure 6.6 and the interval distribution according to pore size is shown in Figure 6.7. The largest pore volume is occupied by pores with diameters in the range of 0.01 - 0.1 µm for all mixtures. The maximum pore volume of give pore size of a mortar mixture differs significantly from the other mixtures at both times. The largest peak for the mortar at 7 days is $\approx$ 55 % lower than that for C-7d, and at 28 days the reduction is $\approx$ 35 %.

The differences in pore volume of a certain size between observation times are shown in Figure 6.7. In the first pore size range, 1 nm - 10 nm, the pore volume of each mixture generally decreased over time. The exception is sample C, where the pore volume increased in this diameter range. In the second pore size range, 10 nm - 0.1 µm, the pore volume of C and CS-I remained unchanged at both times. CS-II-28d and CA-28d decrease by $\approx$ 8 % and $\approx$ 12 %, respectively, compared to age 7 days. In contrast, the pore volume in this range for
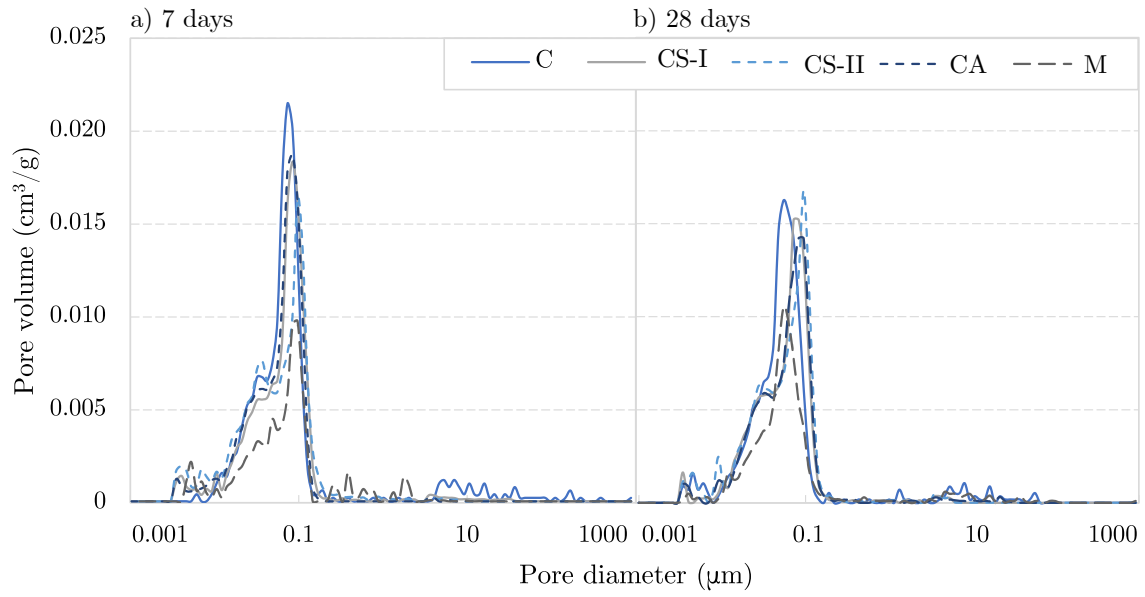
Figure 6.6: Distribution curves of different cement pastes measured a) at 7 days and b) at 28 days of hydration.
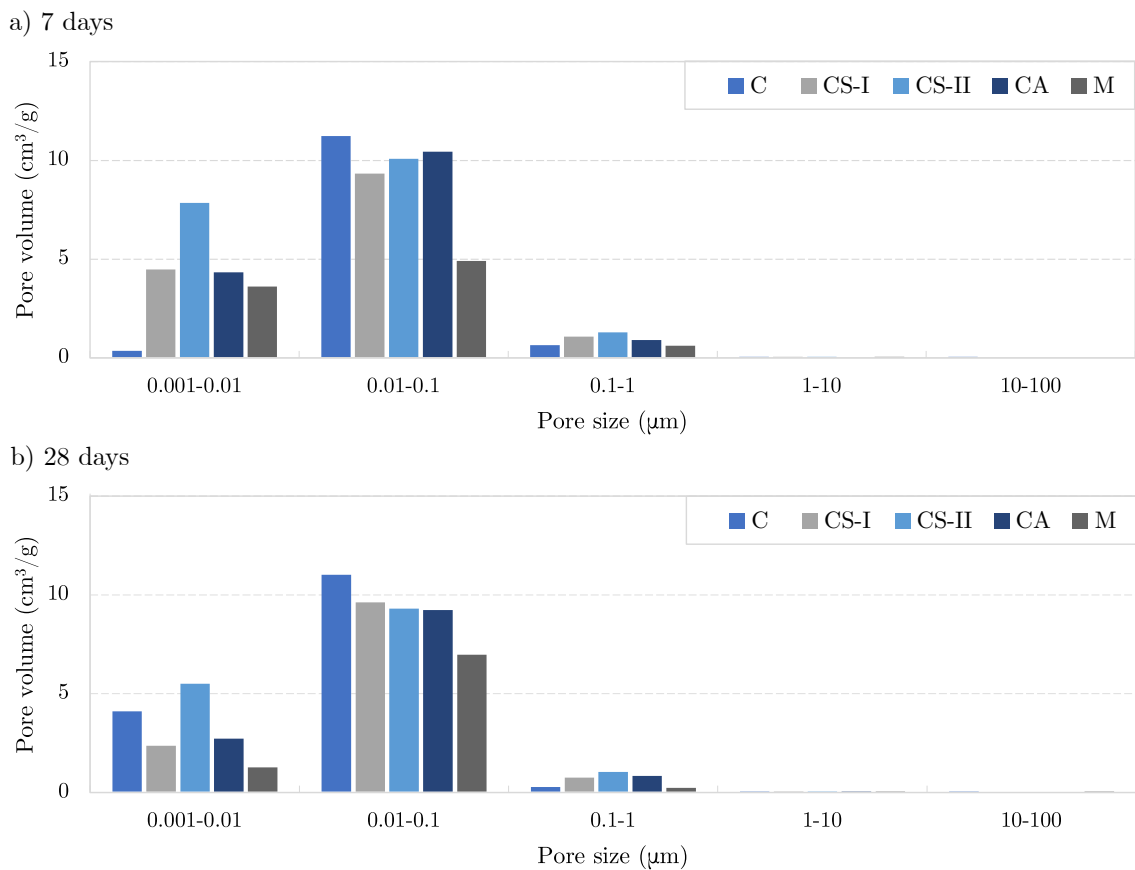


Figure 6.7: Pores measured by MIP a) at 7 days and b) at 28 days of hydration divided according their size.

the mortar increases by $\approx$ 40 % at 28 days compared to the 7-days-old sample. The pore volume of modified cement pastes at this pore diameter range stayed lower than C at both observation times, however with various ratio between each mixtures. The largest change over time is observed between mixtures C and CA. In the pore size range of 0.1 - 1 µm, the pore volume of all mixtures generally decreases with time. The smallest reduction is for the CA, $\approx$ 6 %. For the other mixtures, the reduction at 28 days is $\approx$ 33 % compared to 7 days. In the range of 1 - 100 µm, the differences between the observation times are negligible.

## 6.5    Chloride penetration test

The chloride concentration of the samples ranges from 6.04$\pm$0.29 mg/g to 12.60$\pm$0.06 mg/g, as shown in Figure 6.8.The differences in concentrations of $C_{cl}$ of C, CS-II, and CA mixtures are about $\approx$ 7 % at 7 days. For the mortar, the $C_{cl}$ is $\approx$ 43 % lower than the reference pure cement paste. The differences between the concentrations at 28 days of age are more significant, with the chloride concentration of CS-II being $\approx$ 26 % lower than that of the reference mixture C, while the concentration of CA is $\approx$ 7 % higher. The mortar at 28 days of age contains almost the same chloride concentration as at 7 days of age.
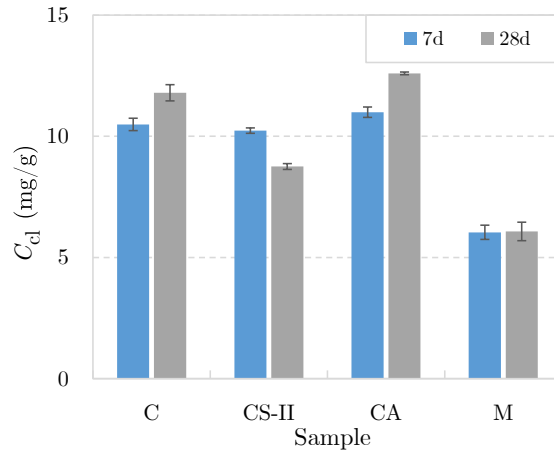


Figure 6.8: Results of chloride penetration test.

The mixtures C, CA, and M have larger chloride concentrations measured at 28 days of age compared to the measurement at 7 days. That was unexpected since the samples with lower porosity should have measured smaller concentrations. It is assumed that chloride has not penetrated the entire sample thickness, and the diffusion coefficient used for prediction varies with hydration time. Also, it is possible that the ability to bind chloride may have decreased with decreased porosity. It can therefore be stated that the penetration time should have been longer.

## 6.6 Electrochemical impedance spectroscopy

### 6.6.1 Equivalent electric circuit models

An example of a typical Nyquist spectrum measured by EIS for the C-56d sample is shown in Figure 6.9a. This spectrum is typical for all saturated mixtures (even mortar) at all the observed times used in this thesis. Figure 6.9b shows the position of the data obtained from EIS measurement on the Nyquist spectrum based on the SEC model. The measured points lie in the lower frequencies of the Nyquist spectrum. Before evaluating the resistance and capacitance, the experimental data was corrected and cut off at both ends. Correction of the data was necessary because the values at very low frequencies correspond to the electrodes' resistance and their contact with the material. The values at high frequencies are inaccurate due to the limitations of the measuring device. Furthermore, the data was fit with the Simplex algorithm with the application of different models. Four different equivalent circuit models (EC, SEC, Cabeza, and Cruz) were used to evaluate the resistance of the connected capillary pores. The resistances differ by $\approx 2$ % as shown in Table 6.5. The most appropriate fits are Cabeza, Cruz, and SEC with the goodness of fit in the order of $10^6$. The accordance of the fits with the experimental data is shown in Figure 6.10. The fits of the EC model deviate mostly from the measured data at high and low frequencies. In contrast, the fits of SEC, Cabeza, and Cruz have almost identical shapes, and the fit measured data more accurately.

SEC model was chosen and applied for porosity evaluation in this thesis, although Cabeza and Cruz models would be equally appropriate for used mixtures.
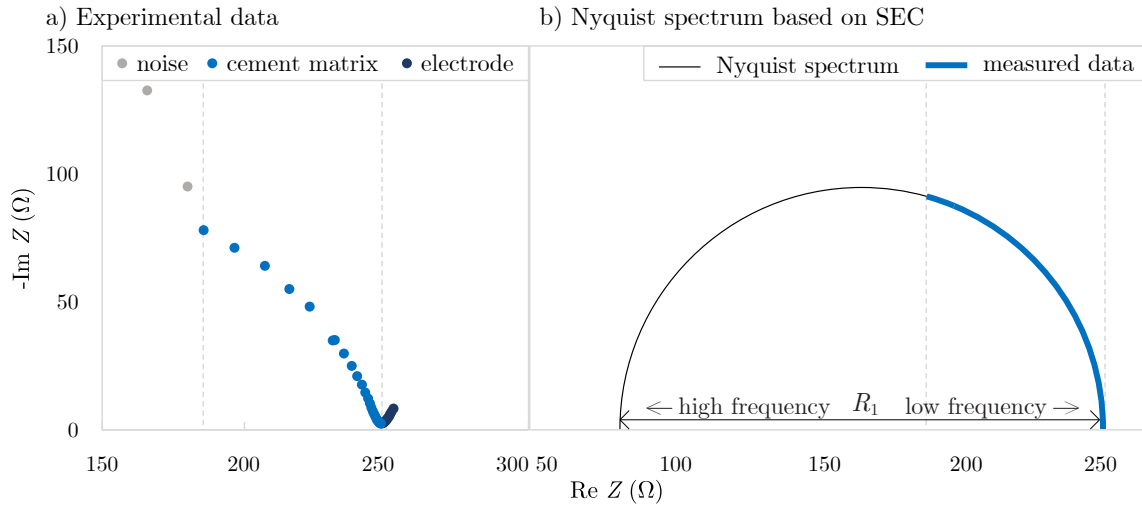


Figure 6.9: a) Experimental Nyquist EIS spectrum of real measured data, b) the position of the measured data on the Nyquist spectrum.

Table 6.5: Resistances of continuously connected pores (CCP) of the C-56d sample evaluated by different equivalent electric circuit models.

| model | resistance of CCP | | goodness of fit |
|---|---|---|---|
| | label | $R$ ($\Omega$) | $\chi^2$ |
| EC | $R_{\mathrm{ccp}}$ | 252.4 $\pm$ 0.9 | 3.7E-05 |
| SEC | $R_1$ | 254.4 $\pm$ 0.9 | 4.5E-06 |
| Cabeza | $R_1$ | 254.1 $\pm$ 0.8 | 1.8E-06 |
| Cruz | $R_1$ | 250.0 $\pm$ 2.2 | 1.9E-06 |
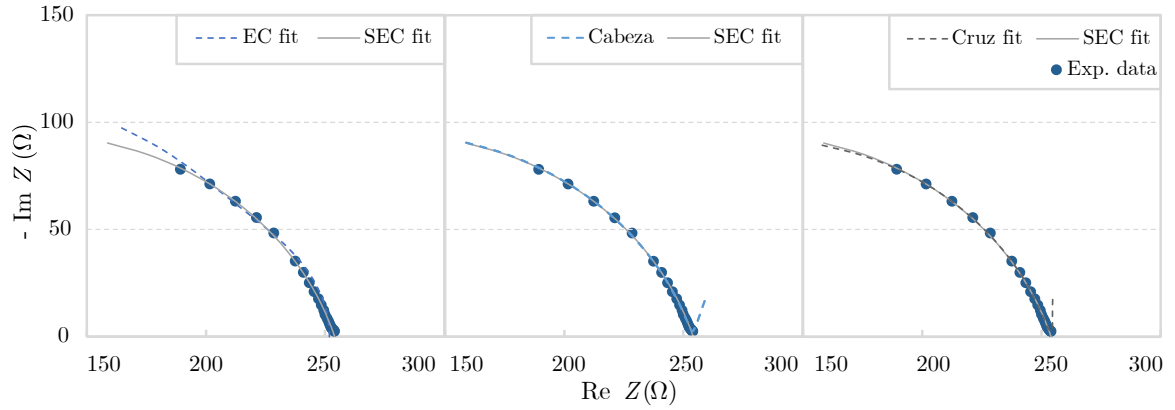


Figure 6.10: Experimental Nyquist EIS spectrum with fits (EC, SEC, Cabeza, Cruz).

### 6.6.2 Resistance and capacity measured by EIS

In the case of EIS measurement, the resistances were not converted to effective electrical conductivity because of the same sample and electrode dimensions (i.e. the ratio $S/d$ is identical for all mixtures). Moreover, resistance values are better describable. Resistances of CBMs increase with ongoing hydration and range from 83.2 $\Omega$ to 471.7 $\Omega$ for all types of samples up to 84 days old, as shown in Figure 6.11a. The capacitances do not have a clear trend. However, they decrease with continuous hydration from 69.2 pF to 28.3 pF, as shown in Figure 6.11b. This effect corresponds to increasing the volume of C-S-H gel and the associated porosity decrease. For example, the resistance of C-84d is $\approx$ 2.8 $\times$ higher than that of C-1d.

During the first 7 hydration age, almost no differences ($\approx$ 2 %) were observed between the resistances of the reference and all modified cement pastes. However, from 14 days of age, the differences between individual paste mixtures started to be more pronounced. The resistances of cement pastes modified by nano-silica increases from 14 to 56 days of age with the increasing nano-SiO$_2$ dose and continuous hydration. The highest resistances of nano-silica modified cement paste is for the CS-I-56d and CS-II-56d, with values higher by $\approx$ 18 % and 46 %, respectively, compared to C-56d. However, at 84 days of age, the resistance values slightly decreased compared to the measurement at 56 days. The reason for this decrease is unknown and may be explained by measurements at a later observation time. The resistances
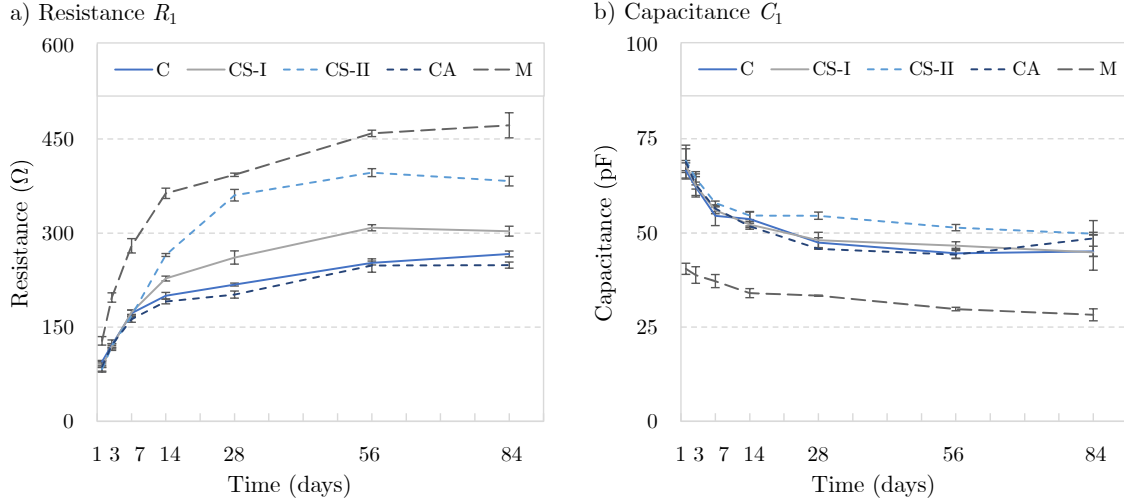
Figure 6.11: a) Resistances $R_1$ and b) Capacitances $C_1$ of different mixtures evaluated from EIS by the SEC model.

of CS-I-84d and CS-II-84d are only about $\approx$ 12 % and 30 %, respectively, higher than C-84d. In contrast, the addition of nano-aluminum reduces the resistivity by $\approx$ 5 % at 56 days of age compared to the reference cement paste at the same hydration time. At 84 days of age, the resistance is the same as that of CA-54d. The mortar has significantly higher resistances than all cement paste samples from the beginning due to the aggregates reducing the number of conductive paths in the matrix.

Table 6.6: Resistances of continuously connected pores (CCP) in materials at different hydration ages evaluated from EIS by the SEC model.

| age | $R$ ($\Omega$) | | | | |
|---|---|---|---|---|---|
| (days) | C | CS-I | CS-II | CA | M |
| 1 | 95.0 $\pm$ 2.0 | 87.6 $\pm$ 2.0 | 83.2 $\pm$ 3.3 | 87.1 $\pm$ 8.7 | 128.3 $\pm$ 6.7 |
| 3 | 121.0 $\pm$ 2.8 | 119.0 $\pm$ 2.0 | 119.6 $\pm$ 4.4 | 121.4 $\pm$ 8.3 | 197.4 $\pm$ 7.4 |
| 7 | 172.3 $\pm$ 4.9 | 173.8 $\pm$ 3.6 | 168.3 $\pm$ 2.2 | 162.8 $\pm$ 4.9 | 279.7 $\pm$ 11.4 |
| 14 | 200.2 $\pm$ 5.2 | 227.6 $\pm$ 3.9 | 265.0 $\pm$ 2.3 | 191.0 $\pm$ 3.8 | 363.4 $\pm$ 8.2 |
| 28 | 218.1 $\pm$ 2.3 | 261.1 $\pm$ 10.5 | 360.4 $\pm$ 9.2 | 202.1 $\pm$ 5.7 | 386.4 $\pm$ 9.4 |
| 56 | 252.4 $\pm$ 3.1 | 308.4 $\pm$ 4.9 | 396.3 $\pm$ 6.3 | 248.3 $\pm$ 10.7 | 458.9 $\pm$ 19.9 |
| 84 | 266.7 $\pm$ 4.6 | 303.0 $\pm$ 7.9 | 382.8 $\pm$ 7.6 | 248.9 $\pm$ 4.9 | 471.7 $\pm$ 9.9 |

### 6.6.3 Influence of relative humidity

The example of measured Nyquist spectra for samples stored 1 month at 11 %, 43 %, 76 %, and 98 % RH is shown in Figure 6.12. The data for samples at 76 % and 98 % RH (in Figure 6.12a, b) have the same shape as fully saturated sample (Figure 6.9), but with larger arc diameter. Data measured for the sample with a relative humidity of 43 % produce a
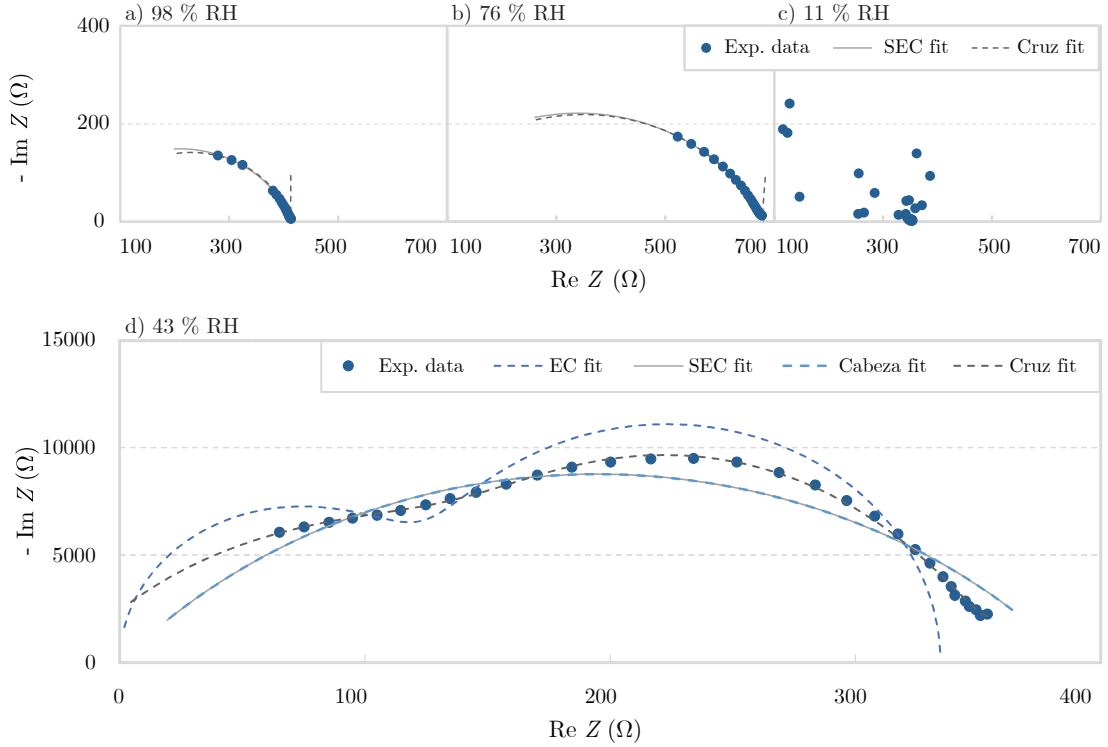
Figure 6.12: Nyquist spectrum of samples stored in different relative humidities showing different models fits: a) 98 % RH, b) 76 % RH, c) 11 % RH, d) 43 % RH.

fuller curve shape (which in this case is no longer a semicircle) and achieve significantly larger values of imaginary impedance (Figure 6.12d). The resistance of the sample stored at 11 % RH was too high, and only disorder data was measured, not applicable for evaluation as shown in Figure 6.12c.

All four models: EC, SEC, Cabeza, and Cruz, were used for the resistance evaluation from data obtained for samples stored in different relative humidities (11 %, 43 %, 76 %, and 98 % RH). Both SEC and Cruz models show negligible differences for 76 % and 98 % RH between each other as shown in Figure 6.12a, b, and both are applicable for evaluation. The evaluation of the samples stored at 43 % RH was only possible with the Cruz model because the fit of this model most accurately corresponds to the experimental data, as shown in Figure 6.12d. The fits of all other models were inappropriate.

The resistances from the reference measurement had to be converted to effective electrical conductivity due to the dimensions and position of embedded electrodes since test samples with different dimensions were used for relative humidity testing. Similar values of the reference samples (before storing in RHs) $\sigma_{eff}$ were obtained as shown in Table 6.7. $\sigma_{eff}$ after storage at different RH for one month decreased by 20 % for the sample stored at 98 % RH), 50 % for the sample at 76 % RH, and 98 % for the sample at 43 % RH compared to reference measurement. After 2 months of storage, the decrease of $\sigma_{eff}$ is attributed to ongoing hydration, not the effect of relative humidity, since the relative humidity should already be stable. Unfortunately, further measurement of samples stored in limewater was not successful. Thus,

Table 6.7: Resistances of mixtures stored in different relative humidities evaluated from EIS by the SEC model.

| RH (%) | $R_1(\Omega)$ | | | $\sigma_{\text{eff}}$ (mS/m) | | |
|---|---|---|---|---|---|---|
| | ref | 1 month | 2 months | ref | 1 month | 2 months |
| 11 | 420 ± 5 | - | - | 75.0 ± 0.7 | - | - |
| 43 | 842 ± 12 | 38730 ± 254 | 59667 ± 665 | 77.0 ± 0.9 | 1.7 ± 0.0 | 1.1 ± 0.0 |
| 76 | 338 ± 1 | 683 ± 2 | 914 ± 10 | 74.6 ± 0.2 | 36.9 ± 0.1 | 27.6 ± 0.2 |
| 98 | 337 ± 2 | 418 ± 3 | 425 ± 1 | 78.6 ± 0.3 | 63.5 ± 0.4 | 62.4 ± 0.1 |
| 100 | 312 ± 2 | - | - | 76.6 ± 0.3 | - | - |

the effect of relative humidity and ongoing hydration was not possible to separate.

Although samples with various dimensions were used (samples stored in 76 % and 98 % RHs had the exact dimensions), the noticeable changes in measured resistances are observable for different relative humidities. The resistivity of samples stored at 76 % and 98 % increases proportionally with decreasing relative humidity, as shown in Table 6.7. The sample stored at 43 % in relative humidity has different electrode dimensions than samples stored at 76 % and 98 %. However, many times larger resistances than the reference, so the position of the electrodes is not as significant as the effect of low relative humidity.

Observation of the influence of relative humidity on the application of EIS was not the main objective of this thesis. Although, given the results above, the influence of RH would deserve a more thorough study with a different experimental plan.

## 6.7 Estimation of porosity from EIS

The relationship between porosity and the electrical properties are defined by Equations (4.11), (4.13), (4.15), and (4.18) in Section 4.2. These relationships contain more than one unknown parameter (porosity $\phi_0$, the conductivity of solid phase $\sigma_s$, percolation threshold $\phi_c$) or a parameter with an unknown time evolution during the hydration period (Archie's index $m$, parameter $k$).

In general, for subsequent evaluation using modified Archie's Law and GEM model, the values of conductivity/resistivity of the pore solution are necessary. The values depend on DoH and are summarized in Table 6.8. The DoH was obtained from Cemhyd3D as shown in Figure 6.13, which reconstructs the hydration process of cement paste in three dimensions. Cemhyd3D uses the typical mineral composition as input according to Taylor's assumption of it [123], the specific surface area of the used clinker, and the ambient temperature. The pore solution's conductivity (respectively resistivity) was obtained from the estimated DoH and the cement composition by the virtual method given in Section 2.2.5. However, this virtual method is derived for DoH in the range of 0.6 - 0.9 [60], so the calculated conductivity of the solid phase at 1 and 3 days may not be accurate. The conductivity $\sigma_s$ was considered to be in the range of 0.0025 Ωm [112] (OPC paste with w/b ratio of 0.4) to 0.01 Ωm [124] (OPC

| hydration age (days) | DoH (%) | $\sigma_0$ (S/m) | $\zeta_0$ ($\Omega$m) |
|---|---|---|---|
| 1 | 42.0 | 11.67 | 0.086 |
| 3 | 56.8 | 12.52 | 0.080 |
| 7 | 65.5 | 13.08 | 0.076 |
| 14 | 71.7 | 13.52 | 0.074 |
| 28 | 76.8 | 13.90 | 0.072 |
| 56 | 80.5 | 14.19 | 0.070 |
| 84 | 82.0 | 14.31 | 0.070 |

Table 6.8: Degree of hydration and conductivity of pore solution at specific hydration time.
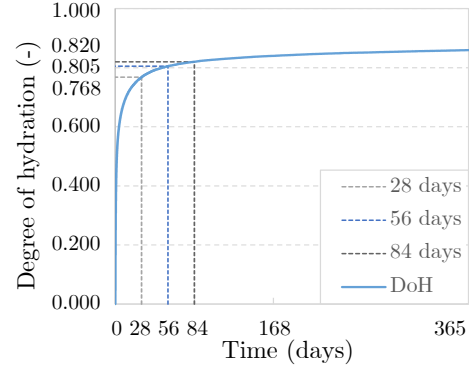


Figure 6.13: Evolution of degree of hydration estimated by Cemhyd3D.

paste with w/b ratio of 0.45). The percolation threshold was considered in the range of 0.15 to 0.2 [113] (OPC with various w/b ratios ranging from 0.3 - 0.5).

Consequently, the porosity, Archie's index $m$, and parameter $k$ (GEM model) are left as only unknowns in presented relationships. Therefore, porosity values measured by helium pycnometry and gravimetric method were used for calibration of parameters $m$ and $k$.

### 6.7.1 Modified Archie's law

Three types of modifications of Archie's law were used in this thesis for porosity evaluation. The classic modification of Archie's law described by Equation (4.11), Archie's law considering the effect of solid phase conductivity described by Equation (4.13), and Archie's law considering the effect of percolation threshold described by Equation (4.15).

Table 6.9: Values of Archie's index of three Archie's law modifications calibrated by porosity from helium pycnometry.

| age | Archie's index, $m_{\mathrm{pyc}}$ (-) | | | | | | | | | | | | | | |
|---|---|---|---|---|---|---|---|---|---|---|---|---|---|---|---|
| (days) | classic modification of Archie's law - Eq. (4.11) | | | | | consideration of solid phase - Eq. (4.13) | | | | | consideration of percolation threshold - Eq. (4.15) | | | | |
| | C | CS-I | CS-II | CA | M | C | CS-I | CS-II | CA | M | C | CS-I | CS-II | CA | M |
| 1 | 3.5 | 3.2 | 3.1 | 3.2 | 2.8 | 3.6 | 3.3 | 3.1 | 3.3 | 2.9 | 2.2 | 1.9 | 1.8 | 1.9 | 1.3 |
| 3 | 3.5 | 3.5 | 3.3 | 3.4 | 3.0 | 3.6 | 3.5 | 3.3 | 3.4 | 3.0 | 2.1 | 2.0 | 1.9 | 2.0 | 1.1 |
| 7 | 3.6 | 3.4 | 3.3 | 3.5 | 3.0 | 3.6 | 3.5 | 3.3 | 3.5 | 3.1 | 2.0 | 1.8 | 1.7 | 1.9 | - |
| 14 | 3.5 | 3.5 | 3.6 | 3.5 | 3.1 | 3.5 | 3.6 | 3.7 | 3.5 | 3.2 | 1.8 | 1.8 | 1.8 | 1.8 | - |
| 28 | 3.4 | 3.6 | 3.7 | 3.4 | 3.1 | 3.5 | 3.6 | 3.8 | 3.4 | 3.1 | 1.7 | 1.8 | 1.7 | 1.6 | - |
| 56 | 3.4 | 3.7 | 3.7 | 3.5 | 3.1 | 3.5 | 3.8 | 3.8 | 3.5 | 3.2 | 1.6 | 1.8 | 1.6 | 1.6 | - |
| 84 | 3.4 | 3.6 | 3.6 | 3.4 | 3.1 | 3.5 | 3.7 | 3.7 | 3.5 | 3.2 | 1.5 | 1.7 | 1.6 | 1.6 | - |

The classic modification of Archie's law uses a total conductivity parameter ($\sigma_{\mathrm{eff}}$) calculated from the measured EIS resistances and the dimensions of the embedded electrodes in

the sample. The constant $C$ depends on the saturation of the sample. Since the samples were fully saturated before measurement and partially immersed in tap water during the measurement, the parameter $C$ was considered equal to 1.0. The conductivity of the pore solution $\sigma_0$ depends on the hydration time and is calculated in Table 6.8.

The modified Archie's law considering the effect of solid phase conductivity also uses $\sigma_{\text{eff}}$ and $\sigma_0$ varying in time. The conductivity of solid phase $\sigma_s$ is assumed to be $0.00775\ \Omega m$ [115]. The modified Archie's law accounting for the effect of the percolation threshold uses a formation factor that depends on the total conductivity $\sigma_{\text{eff}}$ and the conductivity of the pore solution $\sigma_0$. The percolation threshold $\phi_c$ is taken to be 0.2 [113].

In this thesis, for all modifications of Archie's law, the parameter $m$ is not considered a constant as in literature [7, 106] but as a function of the hydration time. The porosity value $\phi_0$ was primarily assumed from measurement by helium pycnometry $\phi_{0,pyc}$. The parameter $m$ is calculated for each observation time and each modification of Archie's law and summarized in Table 6.9. Archie's index with the effect of percolation threshold could not be calculated for M-7d samples and older. Because the measured resistances were higher with time, it is impossible to evaluate the logarithm of a negative number.

The evolution of Archie's index computed from the above modifications is shown in Figure 6.14a. The classic modification and the modification considering the effect of $\sigma_s$ have the same trend. However, the value of the parameter $m_{\text{pyc}}$, including the influence of the solid phase conductivity, is $\approx 0.1$ higher. In contrast, the values of Archie's index with respect to the percolation threshold change significantly in their values (55 % decrease) and time course.
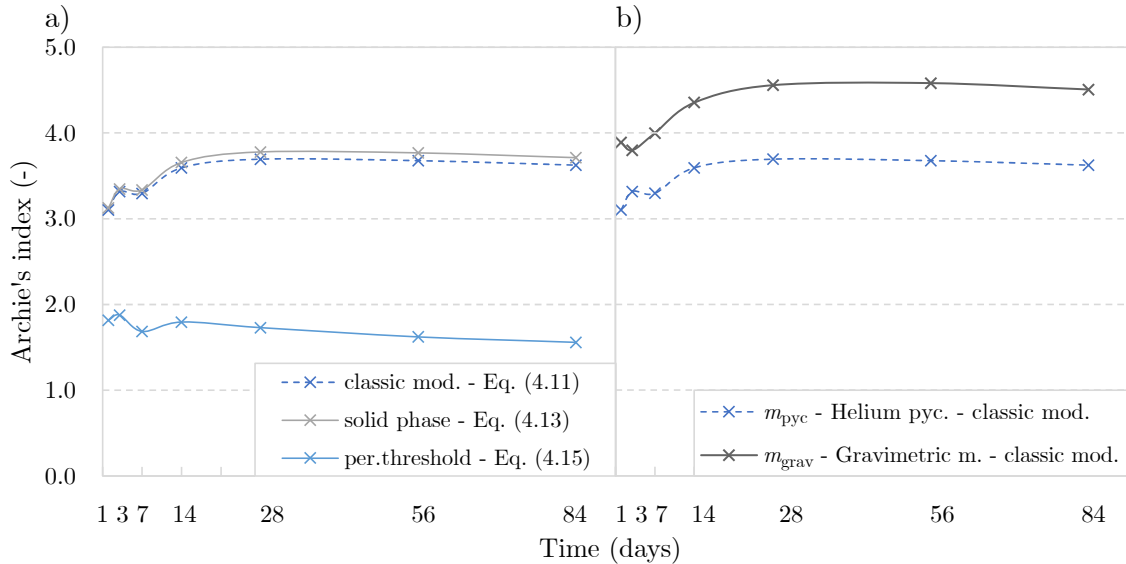


Figure 6.14: Example of Archie index, a) $m_{\text{pyc}}$ evaluated by different Archie's law modifications for CS-II sample calibrated by helium pycnometery, b) Archie index for CS-II sample calibrated by helium pycnometry ($m_{\text{pyc}}$) and gravimetric method ($m_{\text{grav}}$).

The logarithmic function was used to describe the evolution of the Archie index over time, as it gave the most accurate fit calculated data. An example of the fit performed for the classic modification of Archie's law for selected mixtures is shown in Figure 6.15. A different trend can be observed for mixture C, whose values decrease with hydration time. In contrast to the other mixtures, where values increases. The values are likely to stabilize with additional hydration time. In general, it can be concluded that the values of the Archie index for different mixtures at a later period have the following trend: M < C $\doteq$ CA < CS-I $\doteq$ CS-II.
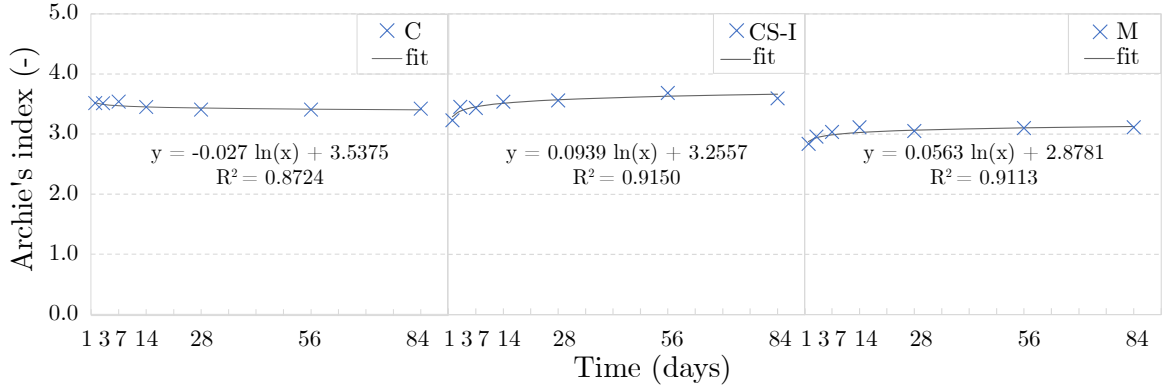


Figure 6.15: Examples of fits of classic modified Archie's law - Equation (4.11) for mixtures C, CS-I, and M.

The porosity evaluated by the gravimetric method was also used to determination of Archie's index $m_{\text{grav}}$. Both $m_{\text{pyc}}$ and $m_{\text{grav}}$ have the same curve shape, as shown in Figure 6.14b. However, the values of $m_{\text{grav}}$ are shifted upwards by $\approx 0.89$. A reason is that the porosity obtained by the gravimetric method takes higher values than the porosity obtained by helium pycnometry. Archie's index is in fact quite closely related to the calibration values used. The trend of Archie's index varies at the initial observation times, which is probably due to an inaccurate estimation of the pore solution conductivity at the first three hydration days.

### 6.7.2 General effective media model

General effective media model can be used to evaluate porosity directly if all the necessary parameters are known, which are percolation threshold $\phi_c$, solid phase conductivity $\sigma_s$, pore solution conductivity $\sigma_0$, total sample conductivity $\sigma_{\text{eff}}$, and parameter $k$. Similar to Archie's law, the parameter $k$ is unknown. Also, the model results are very sensitive to the value of solid phase conductivity. Thus, calibration of these parameters is necessary. In contrast to Archie's law, where experimental measurement at only one time is needed, the GEM model requires several measurements over time to evaluate porosity from experimental data. These experimental data (porosity calibrated by helium pycnometry) were recorded at all seven observation times and plotted as formation factor versus porosity. Then it was used for function fitting according to Equation 4.18 as shown in Figure 6.16.
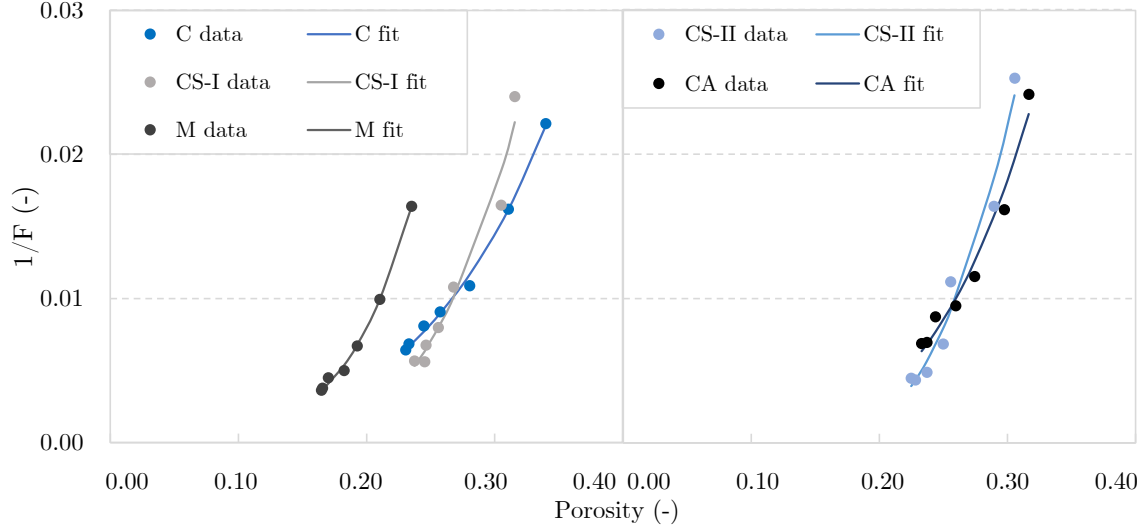
Figure 6.16: Relationship between porosity and formation factor.

The percolation threshold was again assumed to be $\phi_c = 0.2$ since other values significantly affect fit and lower the coefficient of determination values. The result values used to fit the GEM model are summarized in Table 6.10. The conductivity of the solid phase was evaluated to be $\approx 0.0063$ $\Omega$m for the samples (C and M) without nanoparticles addition. This value is within the range of values found in literature 0.0025-0.01 $\Omega$m [112, 124]. Mixtures C and M differ in the parameter $k$, which is twice higher for cement paste than for mortar. The nano-silica probably significantly affects the solid phase conductivity since it takes values even lower than the low limit to ensure the most appropriate fit. The conductivity of the solid phase of CS-I and CS-II mixtures is 0.00100 $\Omega$m and 0.00052 $\Omega$m, respectively. Hence, this value decreases with the increasing amount of nano-silica addition. The conductivity of the solid phase of the CA sample is equal to 0.00266 $\Omega$m and is close to the lower limit reported in literature [112, 124].

Table 6.10: Values of parameter $k$ (GEM model).

| mixture | $k$ (-) | $\sigma_s$ ($\Omega$m) | $\zeta_1$ (S/m) | $R^2$ (-) |
|---|---|---|---|---|
| C | 3.314 | 0.00631 | 158 | 0.999 |
| CS-I | 2.160 | 0.00100 | 1004 | 0.995 |
| CS-II | 1.930 | 0.00052 | 1939 | 0.996 |
| CA | 2.327 | 0.00266 | 375 | 0.996 |
| M | 1.654 | 0.00630 | 159 | 0.999 |

However, the differences in porosity results of the NPs modified cement pastes compared to helium pycnometry are observable. The values more likely correspond to the inverse results of resistances from EIS measurement. The higher the resistance, the lower the porosity obtained. The mixtures CS-I-84d and CS-II-84d have lower porosities of $\approx 15$ % and $\approx 24$ %, respectively than the reference C-84d sample. That confirms the fact that porosity decreases
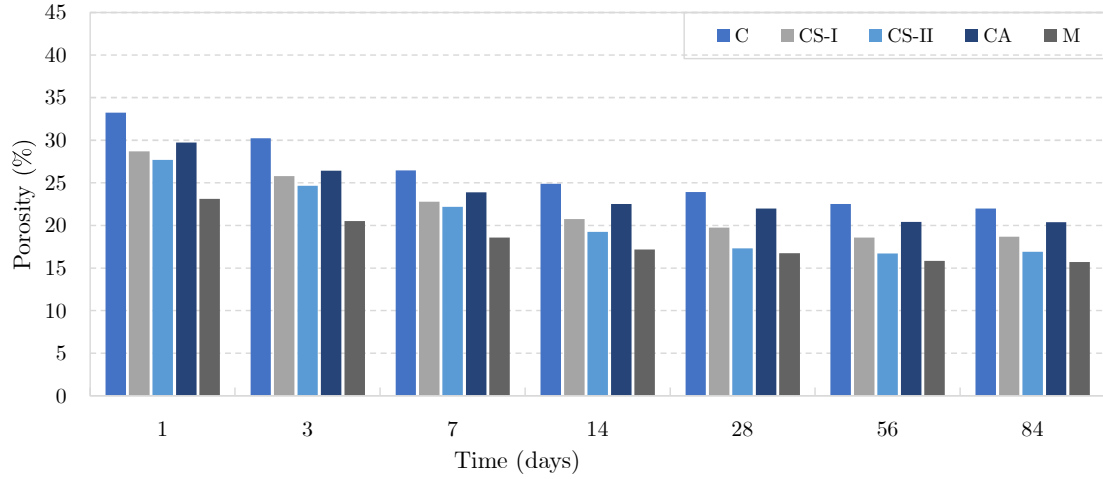
Figure 6.17: Porosity calculated according to GEM model.

with the amount of nano-silica addition. The nano-alumina modified cement paste has a lower porosity of $\approx 10$ % than mixture C at 84 days.

In conclusion, the GEM model, after proper constant calibration, is more suitable for porosity evaluation from EIS measurement than Archie's law since it reflects resistance values from EIS.

Table 6.11: Values of porosity calculated by GEM model.

| age | $\phi_{0,GEM}$ (%) | | | | |
|---|---|---|---|---|---|
| (days) | C | CS-I | CS-II | CA | M |
| 1 | 33.2 | 28.7 | 27.7 | 29.7 | 23.1 |
| 3 | 30.2 | 25.8 | 24.6 | 26.4 | 20.5 |
| 7 | 26.5 | 22.8 | 22.2 | 23.9 | 18.6 |
| 14 | 24.9 | 20.8 | 19.2 | 22.5 | 17.2 |
| 28 | 23.9 | 19.7 | 17.3 | 22.0 | 16.7 |
| 56 | 22.5 | 18.6 | 16.7 | 20.4 | 15.8 |
| 84 | 22.0 | 18.7 | 16.9 | 20.4 | 15.7 |

# 7 Discussion

## 7.1 Comparison of EIS results with the literature

### 7.1.1 EIS resistances

Several researchers have investigated the electrical properties of cement-based materials using EIS.

Vedalakshmi et al. [125] worked with OPC concrete with sample dimensions of (100 × 100 × 100) mm. The electrodes were two stainless steel plates of (40 × 40) mm embedded in the fully saturated sample. An equivalent electric circuit model considered two phases - bulk matrix and pore solution in pores. In the experiment, the obtained resistances were lower than those evaluated in this thesis for the M mixture. At 3 days of age, the effective conductivity obtained by Vedalakshmi was 0.103 S/m, which is $\approx$ 17 % lower than that of the M-3d (0.124 S/m). At 28 days, the value is 0.028 S/m, about $\approx$ 55 % lower than the value M-28d obtained in this thesis. The reason is given that larger aggregates were used for concrete instead of mortar.

Another researcher, Herrera et al. [126], obtained the electrical properties of fully saturated concrete with a $w/c$ ratio of 0.55. However, this experiment cannot be compared with this thesis. The experiment setup was very diverse. The sample was block-shaped (70 × 70 × 150) mm with a single embedded electrode made of steel bar at a depth of about 30 mm. The concrete sample was placed in a PVC container filled with tap water, and stainless steel external electrodes were placed on both sides. Thus, the EIS measurements were performed with a three-electrode arrangement. Measurements were taken for samples aged 7 - 120 days. The resistances and capacitances were evaluated using an equivalent electric circuit for carbonated and non-carbonated material behavior, which has not been included in this thesis.

Mostafa et al. [127] compared the electric properties of different mixtures of ultra-high performance concrete by EIS. Although cylindrical samples with a single rod electrode embedded in the middle of the sample and a different experimental setup were used. It was found that the resistance of the material increased with the addition of nano-silica. The same effect is observed for the mixtures (CS-I, CS-II) used in this thesis.

Many other scientists have studied EIS measurements of CBM. Unfortunately, their research cannot be directly compared with the finding in this thesis. Because the papers do not report the values of the resistances measured [128], the dimensions of the samples [124], the positions of the electrodes [61, 124, 129], or the observation times [106]. In addition, some focus on measurements of values for samples significantly older than in this thesis [130] or samples that have been affected by various influences: isopropanol exchange [128], temperature cycles [130], and forced migration of chloride ions [8] .

### 7.1.2 Porosity calculation from resistances

Porosity can be calculated from the measured resistances according to the modified Archie's law or GEM model. Several researchers have used the same relationships as used in this thesis.

**Modified Archie's law**

Sanish et al. [81] worked with cement pastes with $w/c$ ratio of 0.3 and the concrete with $w/c$ ratio of 0.35. According to the classic modification of Archie's law Equation (4.11), Sanish et al. considered Archie's index equal to 4. The porosity calculated using this value of $m$ shows a large discrepancy (up to 30 %) between the measured and predicted values, especially at early ages. Also, the modified Archie's law, including the effect of solid phase conductivity according to Equation (4.13) was used. The parameter $m$ was still considered to be 4, and $\sigma_s$ is 0.01 S/m. In this thesis, parameter $m$ is 3.5 and 3.6 for classic modification of Archie's law and modified Archie's law, including the effect of solid phase conductivity, respectively. These values are relatively close to $m = 4$ considered by Sanish.

Neithalath et. al [106] worked with the concrete samples with $w/c$ ratio of 0.33. Neithalath considered the Archie index to vary over time, ranging from 1.5 to 2.5 in the classic modification of Archie's law according to Equation (4.11). In this thesis, parameter $m$ is higher ($\approx 3.0$ for M mixture). That is because a different material was used. Also, the modified Archie's law, including the effect of solid phase conductivity according to Equation (4.13), was used to obtain the time evolution of $m$. However, these values are not given in the paper.

He et. al [132] worked with a mortar with $w/c$ ranging from 0.3 to 0.4. The parameter $m$ was considered to vary in time. However, these values are not given in the paper. He used a porosity obtained by MIP to calibrate modified Archie's law.

**GEM model**

Sanish et al. [81] found that the GEM model's predictions are closer to calculated porosity than modified Archie's law. Also, Sanish determined that parameter k lies in the range of 1.93 to 2.10 for different mixtures. In this thesis, parameter k ranges from 1.7 to 2.2 for all mixtures except the C sample (k = 3.3). It can be considered as a good agreement. In addition, Sanish claimed that if the porosity is under the percolation threshold, the GEM model predicts very accurate porosity results. This effect is observable in Figure 7.1 with helium pycnometry porosity calibration.

He et al. [132] used porosity obtained by MIP to calibrate the GEM model. The parameter k was evaluated for samples up to 6 months old and was equal to 1.8127 for the cement paste with $w/c = 0.4$. That value is also within the range obtained in this thesis.

## 7.2 Comparison of porosity measurement techniques with EIS

The porosity values obtained by different methods are shown for the C sample in Figure 7.1 as an example. The same trends are observable for all other mixtures used in this thesis, only with different values. The decrease of the porosity with continuous hydration reaction is observable by all methods used.
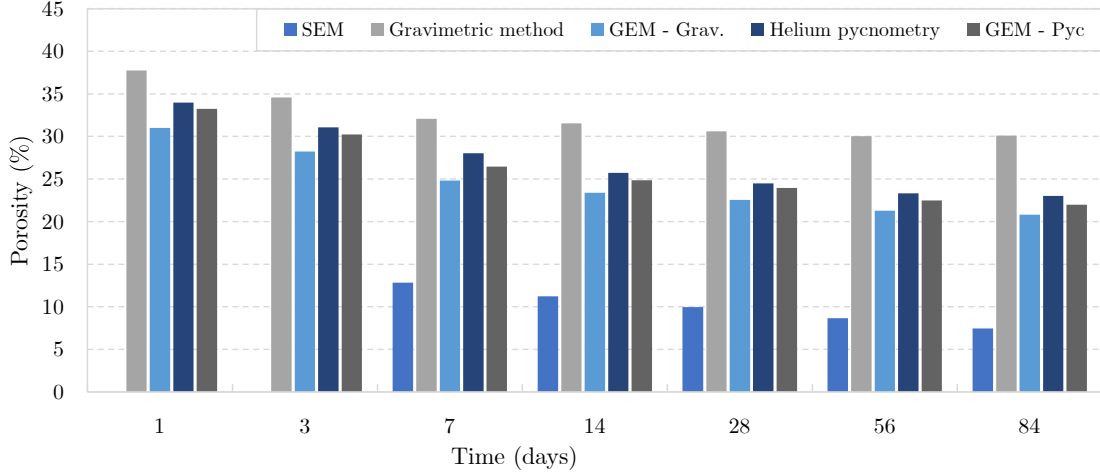


Figure 7.1: Porosity of the C sample obtained by different methods.

The decrease in the porosity over time is well observed by the gravimetric method and helium pycnometry and is associated increase in material resistance measured by EIS. The gravimetric method observed the highest porosity values since it contains large pores and air voids. On the contrary, almost three times lower porosity values were observed by the image analysis of SEM-BSE images. Here, the image analysis serves only as the indicator of pores/cracks phase changes between mixtures and over time. The absolute values do not reflect the actual porosity of the samples.

The porosity obtained by helium pycnometry has lower values than that obtained by the gravimetric method. That is probably due to the different pore size limits of the methods. The helium pycnometry porosity procedure might give another reason since helium pycnometry directly measures matrix density. The bulk density necessary for porosity evaluation is determined by the gravimetric method. Therefore, the value of $\phi_{0,pyc}$ is affected and depends on the gravimetric method.

Moreover, the image analysis can detect the evolution of hydration products over time. The effect of nS addition is observed by the increased amount of main hydrates phase of CS-I and CS-II samples compared to C and CA samples. A similar observation can be noticed by EIS measurement, where the values of resistances have the same trend as the main hydrates phase. During the formation of the new hydration products, the porosity is decreased since the originally free space is filled by these products. It results in an increase of resistance measured by EIS. This observation was not possible made by the gravimetric method or helium pycnometry.

The MIP was the only method able to determine pore size distribution. It can be assumed that the decrease of porosity occurs mainly in pores of size 1 nm - 10 nm with continuous hydration between 7 and 28 days. That means gel pores are the most affected during the observation period. However, a slight reduction in the volume of capillary pores was also observed. Despite this observation, a clear conclusion of which types pores are causing the increase of resistance (reduction of CCP) cannot be made, and it is caused by an overall reduction in porosity.

Porosity calculated by the GEM model and Archie's law modification depends on the methods used for calibration (helium pycnometry, gravimetric method). In the case of Archie's law modification, the porosity value used for calibration is also the value calculated from the model. Thus, the measured resistances from the EIS are not directly reflected in the porosity value but only for the calibration constant Archie index.

On the contrary, the GEM model reflects resistance values during the calculation, despite of technique used for calibration. Nevertheless, the final values are still dependent on the calibration technique used, as shown in Figure 7.1. Although the data from the gravimetric method used for calibration are the highest, the calculated porosity ($\phi_{0,GEM,grav}$) is lower than that of the porosity calculated using the helium pycnometry data ($\phi_{0,GEM,pyc}$). In addition, the coefficient of determination was higher when the porosity from helium pycnometry was used for calibration. Also, the difference between the values of ($\phi_{0,GEM,pyc}$) and ($\phi_{0,pyc}$) is much smaller compared to the gravimetric method.

## 7.3   Chloride penetration test
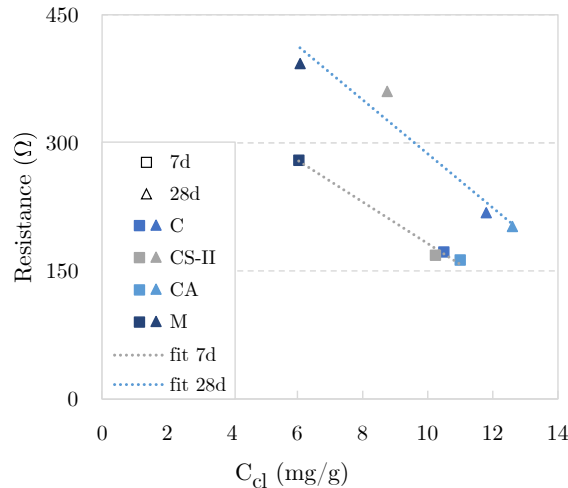


Figure 7.2: The dependence of resistance on chloride concentration.

The relationship between chloride concentration and resistance of the samples is shown in Figure 7.2. Generally, the chloride concentration linearly increases with decreasing resistance. This trend also follows porosity results from another measurement. Also, the chloride concentration measured in the material depends on the age of the sample (degree of hydration)

at which the material is exposed to chloride penetration. Since the exact sample thickness penetrated by chlorides is unknown for 7 and 28 days, as stated in Section 6.5. No conclusion can be drawn between these times.

# 8    Conclusions

In this thesis, the porosity and electric properties of pure cement paste, nanoparticles-modified cement pastes and mortar were investigated. The main method of obtaining the electric properties of the materials was electrochemical impedance spectroscopy with different equivalent electric circuit models used for evaluation. Analytical models were used to evaluate porosity from EIS. Moreover, porosity was also obtained by gravimetric method, helium pycnometry, MIP, and SEM. In addition, a chloride penetration test was performed. Based on the EIS measurements and their comparison with other accompanying tests, the following conclusions can be deduced:

- The sample dimensions and electrode positions have a significant effect on the measured electric properties of the material. Since there are no standardized dimensions for CBMs samples in EIS measurements, a block-shaped sample with dimensions of (54 × 30 × 11.7) mm was designed and found to be optimal in this thesis. The cement paste sample of these dimensions is not affected by hydration heat (cracks formation). For adequate EIS measurement, it is necessary to ensure a sufficient ratio of the area of the electrodes embedded in the material and their distance in the direction of the electric current. In the case of fully saturated samples, measurements should be performed with partial immersion in the solution. Tap water or destilled water is appropriate to use. The lime water used to store the samples is unsuitable because of its high conductivity. Also, samples measured in water must have a sufficiently large covering layer of electrodes to avoid changes in the expected path of the electric current.

- The SEC model is the most appropriate model for saturated cement pastes and mortar for used experiment setting. The Cruz model can be suitably fitted to experimental data, but contains multiple resistors and capacitors that may affect each other. The EC model is inappropriate because it does not overlay measured data at later observation times. The Cabeza model is also inappropriate because it does not fit the measured data sufficiently.

- The measured resistances increase with increasing hydration time for all mixtures used. The resistances of C, CS-I, CS-II, and CA mixtures do not differ in the first 7 days of hydration. Thereafter, the resistance of the CS-I and CS-II increases with the amount of added admixture, by a maximum of $\approx$ 18 % and $\approx$ 46 %, respectively, compared to the C mixture over the observation period. In contrast, the resistance of the CA mixture has slightly lower values $\approx$ 5% than the C mixture. The resistance of the mortar was higher than for all cement paste mixtures during the entire observation period since the amount of continuously connected pores is significantly reduced by the presence of aggregates. This trend in the differences in resistivity across mixtures corresponds to changes in porosity obtained by several other methods.

- Samples stored at high RHs (76 %, 98 %) are measurable and evaluable as fully saturated samples. The resistance of these samples increases as the relative humidity

decreases. The Cruz model is the only model that can evaluate samples stored in intermediate RH (43 %). The resistance of these samples is approximately $100 \times$ higher than for fully saturated samples. The resistances of samples stored in very low relative humidity (11 %) are too high, measuring only scattered points on the Nyquist spectrum. Therefore, no model can evaluate their resistance values.

- The evaluation of porosity from measured resistances can be performed by several modifications of Archie's law or the GEM model. However, a direct evaluation is not possible without knowledge of parameters in these models such as $m$ (Archie's index), $k$ (GEM model). Therefore, porosity obtained by helium pycnometry and gravimetric method was used to calibrate and determine the unknown parameters. Both methods are only as accurate as the porosity used for calibration. However, since the porosity determined by the GEM model depends primarily on the measured resistances, the effect of inaccurate porosity is not as significant as in the case of Archie's law.

- Archie's index can be calculated for each observation time separately. Archie's index is highly influenced and dependent on the porosity obtained by another method. But the influence of resistances determined by EIS is not apparent. Generally, the values of Archie's index evolve with hydration time and are different for every mixture used. Archie's index should not be treated as a constant as in literature. A natural logarithmic function can be used to describe Archie's index evolution over time.

- Several measurements over time are necessary for the calibration of the GEM model. The parameter $k$ and the solid phase conductivity can be obtained by the porosity calibration (e.g. from helium pycnometry or gravimetric method). The porosity can then be calculated with the knowledge of these calibrated parameters. The porosity calculated from these determined parameters depends mainly on the resistances evaluated by EIS.

- The microstructure evolution was observed on both SEM-BSE images and EIS resistance. As the volume fraction of the main hydrates increases, the amount of continuous conductive paths decreases. That corresponds to an increase in resistance. The percentage volume of the main hydrates increases with the amount of nano-silica added together with resistance as additional C-S-H gel is formed, and porosity decreases. Nano-alumina addition did not have a dominant effect on porosity, but a slight decrease in resistance compared to the C sample was found.

- The porosity obtained by the gravimetric method has the highest values because it contains large pores and air voids. The porosity values obtained by helium pycnometry were lower compared to the gravimetric method, probably due to the different pore size limits of the methods. The decreasing porosity of both methods corresponds to the increasing resistance measured by EIS. A slight reduction in gel pores and capillary pores is observed in the pore size distribution obtained by MIP, which also caused an increase in resistances.

- The chloride concentration depends on the sample resistance. With higher resistance, the chloride concentration decreases. The effective diffusion coefficient varies at each observation time, so a more accurate parameter determination should be done at each observation time.

- Generally, EIS can be used to observe the electric properties all designed cementitious mixtures (C, CS-I, CS-II, CA, and M). For resistances and capacitances evaluation, the SEC model is the most accurate and simplest. The GEM model should be used for porosity evaluation because it is complex and time-dependent. For calibration of the GEM model, the porosity obtained by helium pycnometry is the most suitable as it has similar values to the GEM model.

**Future outlook**

Based on the observations retrieved and uncertainties arising from this thesis, the following additional research could be performed, as summarized below:

- Measurements should also be performed at further observation times. That is because the microstructure of CBMs is still evolving with ongoing hydration, especially during the first year (the predict degree of hydration is 0.86). However, EIS measurements were made on samples up to 3 months old when the degree of hydration was predicted to be 0.82. Thus, the measured resistances are not steady.

- To investigate the effect of different RHs on the setup and electrical properties from EIS measurements. The EIS measurements should be performed with samples of the same dimensions and electrode positions, with a more extensive RH spectrum, and with sufficient measurement statistics. The experimental setup should allow the separation of the RH and DoH effects. Also, samples should be measured at the same RH in which they were stored. It should eliminate the negative effect caused by the RH gradient during the measurement.

# Bibliography

[1] D. Breysse. Deterioration processes in reinforced concrete: An overview. In Ch. Maier-hofer, H.W. Reinhardt, and G. Dobmann, editors, *Non-Destructive Evaluation of Reinforced Concrete Structures*, volume 1 of *Woodhead Publishing Series in Civil and Structural Engineering*, pages 28–56. Woodhead Publishing, 2010.

[2] J. Němeček. Micro-scale fracture properties of cementitious composites. 2021.

[3] Y. Reches. Nanoparticles as concrete additives: Review and perspectives. *Construction and Building Materials*, 175:483–495, 2018.

[4] S.C. Paul, A.S. Van Rooyen, G.P.A.G. van Zijl, and L.F. Petrik. Properties of cement-based composites using nanoparticles: A comprehensive review. *Construction and Building Materials*, 189:1019–1034, 2018.

[5] H.H. Hernández, A.M.R. Reynoso, J.C.T. González, C.O.G. Morán, J.G.M. Hernández, A.M. Ruiz, J.M. Hernández, and R.O. Cruz. Electrochemical impedance spectroscopy (EIS): A review study of basic aspects of the corrosion mechanism applied to steels. *Electrochemical Impedance Spectroscopy*, pages 137–144, 2020.

[6] D.V. Ribeiro and J.C.C. Abrantes. Application of electrochemical impedance spectroscopy (EIS) to monitor the corrosion of reinforced concrete: A new approach. *Construction and Building Materials*, 111:98–104, 2016.

[7] R. He, H. Ye, H. Ma, C. Fu, X. Jin, and Z. Li. Correlating the chloride diffusion coefficient and pore structure of cement-based materials using modified noncontact electrical resistivity measurement. *Journal of Materials in Civil Engineering*, 31(3): 04019006, 2019.

[8] I. Sánchez, X.R. Nóvoa, G. De Vera, and M.A. Climent. Microstructural modifications in Portland cement concrete due to forced ionic migration tests. study by impedance spectroscopy. *Cement and concrete research*, 38(7):1015–1025, 2008.

[9] Y. Zhu, H. Zhang, Z. Zhang, and Y. Yao. Electrochemical impedance spectroscopy (EIS) of hydration process and drying shrinkage for cement paste with $w/c$ of 0.25 affected by high range water reducer. *Construction and Building Materials*, 131:536–541, 2017.

[10] J.M. Cruz, I.C. Fita, L. Soriano, J. Payá, and M.V. Borrachero. The use of electrical impedance spectroscopy for monitoring the hydration products of Portland cement mortars with high percentage of pozzolans. *Cement and Concrete Research*, 50:51–61, 2013.

[11] P.A. Danoglidis, M.S. Konsta-Gdoutos, and S.P. Shah. Relationship between the carbon nanotube dispersion state, electrochemical impedance and capacitance and mechanical properties of percolative nanoreinforced OPC mortars. *Carbon*, 145:218–228, 2019.

[12] G. Song. Equivalent circuit model for AC electrochemical impedance spectroscopy of concrete. *Cement and concrete research*, 30(11):1723–1730, 2000.

[13] C. Andrade, V.M. Blanco, A. Collazo, M. Keddam, X.R. Novoa, and H. Takenouti.

Cement paste hardening process studied by impedance spectroscopy. *Electrochimica acta*, 44(24):4313–4318, 1999.

[14] P. Xie, P. Gu, Z. Xu, and J.J. Beaudoin. A rationalized AC impedence model for microstructural characterization of hydrating cement systems. *Cement and Concrete Research*, 23(2):359–367, 1993.

[15] D.E. MacPhee, D.C. Sinclair, and S.L. Stubbs. Electrical characterization of pore reduced cement by impedance spectroscopy. *Journal of materials science letters*, 15 (18):1566–1568, 1996.

[16] G.E. Archie. The electrical resistivity log as an aid in determining some reservoir characteristics. *Transactions of the AIME*, 146(01):54–62, 1942.

[17] Y. Sang, Y. Yang, and Q. Zhao. Electrical resistivity of plain cement-based materials based on ionic conductivity: A review of applications and conductive models. *Journal of Building Engineering*, 46:103642, 2022.

[18] P.W.J. Glover. A generalized Archie's law for n phases. *Geophysics*, 75(6):E247–E265, 2010.

[19] D.S. McLachlan, M. Blaszkiewicz, and R.E. Newnham. Electrical resistivity of composites. *Journal of the American Ceramic Society*, 73(8):2187–2203, 1990.

[20] B.Y. Chang and S.M. Park. Electrochemical impedance spectroscopy. *Annual Review of Analytical Chemistry*, 3(1):207, 2010.

[21] M. Memarpour, F. Shafiei, A. Rafiee, M. Soltani, and M.H. Dashti. Effect of hydroxyapatite nanoparticles on enamel remineralization and estimation of fissure sealant bond strength to remineralized tooth surfaces: An in vitro study. *BMC Oral Health*, 19(1): 1–14, 2019.

[22] Inc US Research Nanomaterials. Aluminum oxide $Al_2O_3$ nanopowder / nanoparticles ($Al_2O_3$, 100% alpha, 99+%, 80nm). Online: https://www.us-nano.com/inc/sdetail/208.

[23] C.R. Gagg. Cement and concrete as an engineering material: An historic appraisal and case study analysis. *Engineering Failure Analysis*, 40:114–140, 2014.

[24] H.F.W. Taylor. *Cement chemistry*. Thomas Telford, 1997.

[25] H.M. Jennings. Refinements to colloid model of C-S-H in cement: CM-II. *Cement and Concrete Research*, 38(3):275 – 289, 2008.

[26] D.P. Bentz, E.J. Garboczi, C.J. Haecker, and O.M. Jensen. Effects of cement particle size distribution on performance properties of Portland cement-based materials. *Cement and Concrete Research*, 29(10):1663–1671, 1999.

[27] V. Ajay, C. Rajeev, and R.K. Yadav. Effect of micro silica on the strength of concrete with ordinary Portland cement. *Research Journal of Engineering Sciences*, 2278:9472, 2012.

[28] M. Bolhassani and M. Samani. Effect of type, size, and dosage of nanosilica and microsilica on properties of cement paste and mortar. *ACI Materials Journal*, 112(2): 1–7, 2015.

[29] P.S. Behera, R. Sarkar, and S. Bhattacharyya. Nano alumina: A review of the powder synthesis method. *Interceram-International Ceramic Review*, 65(1):10–16, 2016.

[30] A. Lazaro, G. Quercia, H.J.H. Brouwers, and J.W. Geus. Synthesis of a green nano-silica material using beneficiated waste dunites and its application in concrete. *World journal of nano science and engineering*, 2013, 2013.

[31] V. Potapov, R. Fediuk, and D. Gorev. Hydrothermal $SiO_2$ nanopowders: Obtaining them and their characteristics. *Nanomaterials*, 10(4), 2020.

[32] M.I. Khan. Nanosilica/silica fume. In R. Siddique and P. Cachim, editors, *Waste and Supplementary Cementitious Materials in Concrete*, Woodhead Publishing Series in Civil and Structural Engineering, pages 461–491. Woodhead Publishing, 2018.

[33] S.M.T. Al-Abboodi, E.J.A. Al-Shaibani, and E.A. Alrubai. Preparation and characterization of nano silica prepared by different precipitation methods. *IOP Conference Series: Materials Science and Engineering*, 978(1):012031, nov 2020.

[34] A. Lazaro, H.J.H. Brouwers, G. Quercia, and J.W. Geus. The properties of amorphous nano-silica synthesized by the dissolution of olivine. *Chemical Engineering Journal*, 211-212:112–121, 2012.

[35] A. Lazaro, Q.L. Yu, and H.J.H. Brouwers. Nanotechnologies for sustainable construction. In J.M. Khatib, editor, *Sustainability of Construction Materials (Second Edition)*, Woodhead Publishing Series in Civil and Structural Engineering, pages 55–78. Woodhead Publishing, second edition edition, 2016.

[36] M. Shojaie-Bahaabad and E. Taheri-Nassaj. Economical synthesis of nano alumina powder using an aqueous sol–gel method. *Materials Letters*, 62(19):3364–3366, 2008.

[37] Jiang Li, Yubai Pan, Changshu Xiang, Qiming Ge, and Jingkun Guo. Low temperature synthesis of ultrafine $Al_2O_3$ powder by a simple aqueous sol–gel process. *Ceramics International*, 32(5):587–591, 2006.

[38] J.C. Toniolo, M.D. Lima, A.S. Takimi, and C.P. Bergmann. Synthesis of alumina powders by the glycine-nitrate combustion process. *Materials research bulletin*, 40(3):561–571, 2005.

[39] Z. Wu, Y. Shen, Y. Dong, and J. Jiang. Study on the morphology of $\alpha$-$Al_2O_3$ precursor prepared by precipitation method. *Journal of Alloys and Compounds*, 467(1-2):600–604, 2009.

[40] S.A. Hosseini, A. Niaei, and D. Salari. Production of $\gamma$-$Al_2O_3$ from kaolin. *Open Journal of Physical Chemistry*, 1(2):23–27, 2011.

[41] A.W.A. Al-Ajeel and S.I. Al-Sindy. Alumina recovery from Iraqi kaolinitic clay by hydrochloric acid route. *Iraqi bulletin of Geology and Mining*, 2(1):67–76, 2006.

[42] M. Thomas. *Optimizing the use of fly ash in concrete*, volume 5420. Portland Cement Association Skokie, IL, 2007.

[43] J.J. Thomas and H.M. Jennings. Materials of cement science primer: The science of concrete. Technical report, 2009.

[44] H. Zhang, Y. Xu, Y. Gan, Z. Chang, E. Schlangen, and B. Šavija. Microstructure

informed micromechanical modelling of hydrated cement paste: Techniques and challenges. *Construction and Building Materials*, 251:118983, 2020.

[45] I. Pane and W. Hansen. Investigation of blended cement hydration by isothermal calorimetry and thermal analysis. *Cement and Concrete Research*, 35(6):1155–1164, 2005.

[46] K. Van Breugel. Simulation of hydration and formation of structure in hardening cement-based materials. 1993.

[47] S. Bishnoi and K.L. Scrivener. A new platform for modelling the hydration of cements. *Cement and Concrete Research*, 39(4):266 – 274, 2009.

[48] H.M. Jennings and S.K. Johnson. Simulation of microstructure development during the hydration of a cement compound. *Journal of the American Ceramic Society*, 69 (11):790–795, 1986.

[49] P. Navi and C. Pignat. Simulation of cement hydration and the connectivity of the capillary pore space. *Advanced Cement Based Materials*, 4(2):58–67, 1996.

[50] Ø. Bjøntegaard, H. Budelmann, M. Krauss, and T.A. Martius-Hammer. Rilem technical committee 195-dtd recommendation for test methods for AD and TD of early age concrete. *Dordrecht: Springer Netherlands (RILEM State-of-the-Art Reports). doi*, 10: 978–94, 2015.

[51] X.Y. Wang, H.S. Lee, and K.B. Park. Simulation of low-calcium fly ash blended cement hydration. *ACI Materials Journal*, 106(2):167, 2009.

[52] R. Chaube, T. Kishi, and K. Maekawa. *Modelling of concrete performance: Hydration, microstructure and mass transport.* CRC Press, 1999.

[53] D.P. Bentz. Three-dimensional computer simulation of Portland cement hydration and microstructure development. *J. Am. Ceram. Soc.*, 80(1):3–21, 1997.

[54] J.W. Bullard. A three-dimensional microstructural model of reactions and transport in aqueous mineral systems. *Modelling and Simulation in Materials Science and Engineering*, 15(7):711, 2007.

[55] V. Šmilauer and Z. Bittnar. Microstructure-based micromechanical prediction of elastic properties in hydrating cement paste. *Cement and Concrete Research*, 36(9):1708 – 1718, 2006.

[56] Y.Y. Kim, K.M. Lee, J.W. Bang, and S.J. Kwon. Effect of $w/c$ ratio on durability and porosity in cement mortar with constant cement amount. *Advances in Materials Science and Engineering*, 2014, 2014.

[57] A. Aili and I. Maruyama. Review of several experimental methods for characterization of micro-and nano-scale pores in cement-based material. *International Journal of Concrete Structures and Materials*, 14(1):1–18, 2020.

[58] A. Vollpracht, B. Lothenbach, R. Snellings, and J. Haufe. The pore solution of blended cements: A review. *Materials and Structures*, 49(8):3341–3367, 2016.

[59] K.A Snyder, X. Feng, B.D. Keen, and T.O. Mason. Estimating the electrical conductivity of cement paste pore solutions from OH, K and Na concentrations. *Cement and Concrete Research*, 33(6):793–798, 2003.

[60] D.P. Bentz. A Virtual Rapid Chloride Permeability Test. *Cement and Concrete Composites*, 29(10):723–731, 2007.

[61] B.J. Christensen, T. Coverdale, R.A. Olson, S.J. Ford, E.J. Garboczi, H.M. Jennings, and T.O. Mason. Impedance spectroscopy of hydrating cement-based materials: measurement, interpretation, and application. *Journal of the American Ceramic Society*, 77(11):2789–2804, 1994.

[62] National Institute of Standards and technology. Estimation of pore solution conductivity. Online: https://www.nist.gov/el/materials-and-structural-systems-division-73100/inorganic-materials-group-73103/estimation-pore, 2017.

[63] S.W.M. Supit and F.U.A. Shaikh. Durability properties of high volume fly ash concrete containing nano-silica. *Materials and structures*, 48(8):2431–2445, 2015.

[64] A.N. Givi, S.A. Rashid, F.N.A. Aziz, and M.M.Salleh. Experimental investigation of the size effects of $SiO_2$ nano-particles on the mechanical properties of binary blended concrete. *Composites Part B: Engineering*, 41(8):673–677, 2010.

[65] S. Maheswaran, B. Bhuvaneshwari, G.S. Palani, R. Nagesh, and S. Kalaiselvam. An overview on the influence of nano silica in concrete and a research initiative. *Research Journal of Recent Sciences, ISSN*, 2277:2502, 2013.

[66] G.H. Barbhuiya, M.A. Moiz, S.D. Hasan, and M.M. Zaheer. Effects of the nanosilica addition on cement concrete: A review. *Materials Today: Proceedings*, 32:560–566, 2020.

[67] P. Hou, J.i Qian, X. Cheng, and S.P. Shah. Effects of the pozzolanic reactivity of $nanoSiO_2$ on cement-based materials. *Cement and Concrete Composites*, 55:250–258, 2015.

[68] S. Bai, X. Guan, H. Li, and J. Ou. Effect of the specific surface area of nano-silica particle on the properties of cement paste. *Powder Technology*, 392:680–689, 2021.

[69] S. Barbhuiya, S. Mukherjee, and H. Nikraz. Effects of nano-$Al_2O_3$ on early-age microstructural properties of cement paste. *Construction and Building Materials*, 52: 189–193, 2014.

[70] Z. Yang, Y. Gao, S. Mu, H. Chang, W. Sun, and J. Jiang. Improving the chloride binding capacity of cement paste by adding nano-$Al_2O_3$. *Construction and Building Materials*, 195:415–422, 2019.

[71] A. Nazari, S. Riahi, S. Riahi, S. Fatemeh Shamekhi, and A. Khademno. Influence of $Al_2O_3$ nanoparticles on the compressive strength and workability of blended concrete. *Journal of American Science*, 6(5):6–9, 2010.

[72] N. León, J. Massana, F. Alonso, A. Moragues, and E. Sánchez-Espinosa. Effect of nano-$Si_2O$ and nano-$Al_2O_3$ on cement mortars for use in agriculture and livestock production. *Biosystems Engineering*, 123:1–11, 2014.

[73] G.K. Glass and N.R. Buenfeld. The presentation of the chloride threshold level for corrosion of steel in concrete. *Corrosion science*, 39(5):1001–1013, 1997.

[74] T. Maruya, S. Tangtermsirikul, and Y. Matsuoka. Modeling of movement of chloride

ions in concrete surface layer. *Jornal of Materials, Concrete Structures and Pavement*, 38(585):79–95, 1998.

[75] M.V.A. Florea and H.J.H. Brouwers. Chloride binding related to hydration products: Part I: Ordinary Portland Cement. *Cement and Concrete Research*, 42(2):282–290, 2012.

[76] C. Yi, H. Ma, H. Zhu, W. Li, M. Xin, Y. Liu, and Y. Guo. Study on chloride binding capability of coal gangue based cementitious materials. *Construction and Building Materials*, 167:649–656, 2018.

[77] T. Ishida, S. Miyahara, and T. Maruya. Chloride binding capacity of mortars made with various Portland cements and mineral admixtures. *Journal of Advanced Concrete Technology*, 6(2):287–301, 2008.

[78] B. Benmokrane, M. Robert, and T. Youseff. Reinforcement of concrete using fibre-reinforced polymer composites. In Vistasp M. Karbhari, editor, *Durability of Composites for Civil Structural Applications*, Woodhead Publishing Series in Civil and Structural Engineering, pages 225–246. Woodhead Publishing, 2007.

[79] D.W.S. Ho and R.K. Lewis. Carbonation of concrete and its prediction. *Cement and Concrete Research*, 17(3):489–504, 1987.

[80] T. Ishida, P.O.N. Iqbal, and H.T.L. Anh. Modeling of chloride diffusivity coupled with non-linear binding capacity in sound and cracked concrete. *Cement and Concrete Research*, 39(10):913–923, 2009.

[81] K.B. Sanish, N. Neithalath, and M. Santhanam. Monitoring the evolution of material structure in cement pastes and concretes using electrical property measurements. *Construction and Building Materials*, 49:288–297, 2013.

[82] F. Bayer. Degradace mikrostruktury betonu použitím elektrochemických ochran výztuže. 2022.

[83] M. Krus, K.K. Hansen, and H.M. Künzel. Porosity and liquid absorption of cement paste. *Materials and Structures*, 30(7):394–398, 1997.

[84] K.L. Scrivener. Backscattered electron imaging of cementitious microstructures: understanding and quantification. *Cement and Concrete Composites*, 26(8):935 – 945, 2004. Scanning electron microscopy of cements and concretes.

[85] K.L. Scrivener, H.H. Patel, P.L. Pratt, and L.J. Parrott. Analysis of phases in cement paste using backscattered electron images, methanol adsorption and thermogravimetric analysis. *MRS Online Proceedings Library (OPL)*, 85, 1986.

[86] C. Mignot. Color (and 3D) for scanning electron microscopy. *Microscopy Today*, 26(3): 12–17, 2018.

[87] J. Němeček, J. Lukeš, and J. Němeček. High-speed mechanical mapping of blended cement pastes and its comparison with standard modes of nanoindentation. *Materials Today Communications*, 23:100806, 2020.

[88] K.L. Scrivener. The use of backscattered electron microscopy and image analysis to study the porosity of cement paste. *MRS Online Proceedings Library (OPL)*, 137, 1988.

[89] A. Accary. *Experimental characterization of the interstitial pore pressure of wet concrete under high confining pressure.* PhD thesis, Université Grenoble Alpes, 2018.

[90] A.M. Geddis, A.G. Guzman, and R.L. Bassett. *Rapid estimate of solid volume in large tuff cores using a gas pycnometer.* Citeseer, 1996.

[91] B.O. Marinder. A simple apparatus for determining the density of solids. *Measurement Science and Technology*, 7(11):1569–1573, nov 1996.

[92] C.L. Bielders, L.W. De Backer, and B. Delvaux. Particle density of volcanic soils as measured with a gas pycnometer. *Soil Science Society of America Journal*, 54(3):822–826, 1990.

[93] S. Van Vlierberghe, G.J. Graulus, S. K. Samal, I. Van Nieuwenhove, and P. Dubruel. Porous hydrogel biomedical foam scaffolds for tissue repair. In *Biomedical foams for tissue engineering applications*, pages 335–390. Elsevier, 2014.

[94] R.E. Danielson and P.L. Sutherland. Porosity. *Methods of soil analysis: Part 1 physical and mineralogical methods*, 5:443–461, 1986.

[95] S. Tamari. Optimum design of the constant-volume gas pycnometer for determining the volume of solid particles. *Measurement Science and Technology*, 15(3):549–558, feb 2004.

[96] Y. Jiang, M. Lawrence, M.P. Ansell, and A. Hussain. Cell wall microstructure, pore size distribution and absolute density of hemp shiv. *Royal Society Open Science*, 5(4): 171945, 2018.

[97] D. Shi and D.N. Winslow. Contact angle and damage during mercury intrusion into cement paste. *Cement and Concrete Research*, 15(4):645–654, 1985.

[98] S.P. Rigby, D. Barwick, R.S. Fletcher, and S.N. Riley. Interpreting mercury porosimetry data for catalyst supports using semi-empirical alternatives to the Washburn equation. *Applied Catalysis A: General*, 238(2):303–318, 2003.

[99] K. Scrivener, R. Snellings, B. Lothenbach, et al. *A practical guide to microstructural analysis of cementitious materials*, volume 540. Crc Press Boca Raton, FL, USA:, 2016.

[100] H.J. Haugen and S. Bertoldi. Characterization of morphology—3D and porous structure. In Maria Cristina Tanzi and Silvia Farè, editors, *Characterization of Polymeric Biomaterials*, pages 21–53. Woodhead Publishing, 2017.

[101] J.E. Garland, C.M. Pettit, and D. Roy. Analysis of experimental constraints and variables for time resolved detection of Fourier transform electrochemical impedance spectra. *Electrochimica Acta*, 49(16):2623–2635, 2004.

[102] R. Cottis and S. Turgoose. *Electrochemical impedance and noise*, volume 7. National Assn of Corrosion Engineers, 1999.

[103] H.W. Whittington, J. McCarter, and M.C. Forde. The conduction of electricity through concrete. *Magazine of concrete research*, 33(114):48–60, 1981.

[104] B.J. Christensen, T.O. Mason, and H.M. Jennings. Influence of silica fume on the early hydration of Portland cements using impedance spectroscopy. *Journal of the American Ceramic Society*, 75(4):939–945, 1992.

[105] D.E. Macphee, D.C. Sinclair, and S.L. Cormack. Development of an equivalent circuit

model for cement pastes from microstructural considerations. *Journal of the American Ceramic Society*, 80(11):2876–2884, 1997.

[106] N. Neithalath, J. Weiss, and J. Olek. Characterizing enhanced porosity concrete using electrical impedance to predict acoustic and hydraulic performance. *Cement and Concrete Research*, 36(11):2074–2085, 2006.

[107] X. Hu, C. Shi, X. Liu, J. Zhang, and G. De Schutter. A review on microstructural characterization of cement-based materials by AC impedance spectroscopy. *Cement and Concrete Composites*, 100:1–14, 2019.

[108] A.E.A. Hamami, J.M. Loche, and A. Aït-Mokhtar. Cement fraction effect on EIS response of chloride migration tests. *Advances in Cement Research*, 23(5):233–240, 2011.

[109] M. Cabeza, M. Keddam, X.R. Nóvoa, I. Sánchez, and H. Takenouti. Impedance spectroscopy to characterize the pore structure during the hardening process of Portland cement paste. *Electrochimica Acta*, 51(8-9):1831–1841, 2006.

[110] A. Covelo, B. Diaz, L. Freire, X.R. Nóvoa, and M.C. Perez. Microstructural changes in a cementitious membrane due to the application of a DC electric field. *Journal of Environmental Science and Health Part A*, 43(8):985–993, 2008.

[111] B.A. Boukamp. A linear Kronig-Kramers transform test for immittance data validation. *Journal of the electrochemical society*, 142(6):1885, 1995.

[112] E.J. Garboczi and D.P. Bentz. Computer simulation of the diffusivity of cement-based materials. *Journal of materials science*, 27(8):2083–2092, 1992.

[113] S. Bejaoui and B. Bary. Modeling of the link between microstructure and effective diffusivity of cement pastes using a simplified composite model. *Cement and Concrete Research*, 37(3):469–480, 2007. Cementitious Materials as model porous media: Nanostructure and Transport processes.

[114] B.H. Oh and S.Y. Jang. Prediction of diffusivity of concrete based on simple analytic equations. *Cement and Concrete Research*, 34(3):463–480, 2004.

[115] H. Ma, D. Hou, J. Liu, and Z. Li. Estimate the relative electrical conductivity of C–S–H gel from experimental results. *Construction and Building Materials*, 71:392–396, 2014.

[116] S. Fallah and M. Nematzadeh. Mechanical properties and durability of high-strength concrete containing macro-polymeric and polypropylene fibers with nano-silica and silica fume. *Construction and Building Materials*, 132:170–187, 2017.

[117] A. Nazari, S. Riahi, S. Riahi, S.F. Shamekhi, and A. Khademno. Mechanical properties of cement mortar with $Al_2O_3$ nanoparticles. *Journal of American Science*, 6(4):94–97, 2010.

[118] Y. Li, B. Feng, J. Liu, M. He, and F. Shi. Coal desulfurization and deashing by high voltage pulse treatment in tap water. *Fuel*, 324:124621, 2022.

[119] M. Takahashi. $\zeta$ potential of microbubbles in aqueous solutions: electrical properties of the gas- water interface. *The Journal of Physical Chemistry B*, 109(46):21858–21864, 2005.

[120] S. Caré. Effect of temperature on porosity and on chloride diffusion in cement pastes. *Construction and Building Materials*, 22(7):1560–1573, 2008.

[121] H.S. Wong, M.K. Head, and N.R. Buenfeld. Pore segmentation of cement-based materials from backscattered electron images. *Cement and concrete research*, 36(6):1083–1090, 2006.

[122] R. Nováková, M. Kouřil, J. Soulil, K. Splítek, V. Špinar, D. Dobiáš, and P. Pokorný. Relation of corrosion simulators transport and modern concrete pore microstructure. In *Conference METAL*, page 6, 2015.

[123] H.F.W. Taylor. Modification of the Bogue calculation. *Advances in Cement Research*, 2(6):73–77, 1989.

[124] R.T. Coverdale, B.J. Christensen, H.M. Jennings, T.O. Mason, D.P. Bentz, and E.J. Garboczi. Interpretation of impedance spectroscopy of cement paste via computer modelling. *Journal of Materials Science*, 30(3):712–719, 1995.

[125] R. Vedalakshmi, R.R. Devi, B. Emmanuel, and N. Palaniswamy. Determination of diffusion coefficient of chloride in concrete: an electrochemical impedance spectroscopic approach. *Materials and Structures*, 41(7):1315–1326, 2008.

[126] H.H. Hernández, F.G. Díaz, G.D.J.F.S. Miguel, J.C.R.V. Altamirano, C.O.G. Morán, and J.M. Hernández. Electrochemical impedance spectroscopy as a practical tool for monitoring the carbonation process on reinforced concrete structures. *Arabian Journal for Science and Engineering*, 44(12):10087–10103, 2019.

[127] Sahar A Mostafa, Mohamed M El-Deeb, Ahmed A Farghali, and A Serag Faried. Evaluation of the nano silica and nano waste materials on the corrosion protection of high strength steel embedded in ultra-high performance concrete. *Scientific Reports*, 11(1): 1–16, 2021.

[128] G.M. Moss, B.J. Christensen, T.O. Mason, and H.M. Jennings. Microstructural analysis of young cement pastes using impedance spectroscopy during pore solution exchange. *Advanced Cement Based Materials*, 4(2):68–75, 1996.

[129] S.J. Ford, T.O. Mason, B.J. Christensen, R.T. Coverdale, H.M. Jennings, and E.J. Garboczi. Electrode configurations and impedance spectra of cement pastes. *Journal of Materials Science*, 30(5):1217–1224, 1995.

[130] W.J. McCarter, G. Starrs, and T.M. Chrisp. Electrical conductivity, diffusion, and permeability of Portland cement-based mortars. *Cement and Concrete Research*, 30 (9):1395–1400, 2000.

[131] S. Tully-Dartez, H.E. Cardenas, and P.F.S. Sit. Pore characteristics of chitosan scaffolds studied by electrochemical impedance spectroscopy. *Tissue Engineering Part C: Methods*, 16(3):339–345, 2010.

[132] R. He, H. Ma, R.B. Hafiz, C. Fu, X. Jin, and J. He. Determining porosity and pore network connectivity of cement-based materials by a modified non-contact electrical resistivity measurement: Experiment and theory. *Materials & Design*, 156:82–92, 2018.